

Thermal and Nonthermal Emission from the Nearby Galaxy M33

A Multi-Scale Study of Infrared and Radio Emission

Dissertation

zur

Erlangung des Doktorgrades (Dr. rer. nat.)

der

Mathematisch-Naturwissenschaftlichen Fakultäten

der

Rheinischen Friedrich-Wilhelms-Universität Bonn

vorgelegt von

Fatemeh Tabatabaei

aus

Tehran, Iran

Bonn, 2008

Angefertigt mit Genehmigung der Mathematisch-Naturwissenschaftlichen
Fakultät der Rheinischen Friedrich-Wilhelms-Universität Bonn

Referent: Prof. Dr. U. Klein
Korreferent: Prof. Dr. P. L. Biermann
Tag der mündlichen Prüfung: 22/01/2008

Diese Dissertation ist auf dem Hochschulschriftenserver der ULB Bonn
<http://hss.ulb.uni-bonn.de/diss-online>
elektronisch publiziert. Das Erscheinungsjahr ist 2008.

Abstract

A multi-wavelength study of radio and IR emission from the nearby galaxy M33 is presented. We focus on three main topics: 1) energy sources of IR emission and its correlation with radio continuum emission at different spatial scales, 2) separation of thermal and nonthermal components of the radio continuum emission without assuming a constant nonthermal spectral index, and 3) distribution of the linearly polarized emission and magnetic fields in M33.

Highly resolved and sensitive Spitzer MIPS images of M33 at 24, 70, and 160 μm enabled us to study the morphology of different dust components and their role in attenuation of the $\text{H}\alpha$ emission from this galaxy. Radio continuum observations with the VLA and the 100-m Effelsberg telescope led to high sensitive maps of total and linearly polarized radio continuum emission at low (1.42 GHz) and high frequencies (8.35 GHz). A 2D-wavelet transformation was used to find dominant scales of emitting structures, separate the diffuse emission components from compact sources, and compare IR emitting structures to those at radio and $\text{H}\alpha$ wavelengths.

We found that the IR emission is powered predominantly by young O/B stars, specifically at 24 and 70 μm . At least up to scales of 0.8 kpc, the cold dust (emitting at 160 μm) is also effectively heated by UV photons from massive ionizing stars, however, the average radiation field also contributes to heating the cold dust at larger scales. At scales smaller than 4 kpc, emission from both the warm and the cold dust show better correlation with the thermal radio than with the nonthermal radio emission, indicating a more important role of UV photons from O/B stars than of cosmic ray electrons in heating the dust at these scales. Interestingly, there is a characteristic scale range where the nonthermal radio–IR correlation is maximum: scales of giant star-forming regions, spiral arms and the central extended region of M33, 0.8–2 kpc, indicating regions with high-density cosmic rays and/or stronger (turbulent) magnetic field.

We developed a new thermal/nonthermal separation method based on a de-reddened $\text{H}\alpha$ map as a template for the thermal radio emission. For the first time, we derived a map of the nonthermal spectral index in a galaxy by means of this method, directly indicating energy loss of cosmic ray electrons when diffusing away from their origins in star-forming regions towards interarm regions and the outer parts of the galaxy. Furthermore, this energy loss is more significant at 8.35 GHz than at 1.42 GHz. Assuming equipartition between the magnetic field and cosmic ray electrons, we obtained the scale length of the cosmic ray electrons and of the magnetic field $\simeq 12$ kpc and 24 kpc, respectively.

The large-scale magnetic field exhibits a well ordered spiral structure with almost the same orientation as that of the optical spiral arms. There is a north-south asymmetry in the received polarized emission that is frequency-dependent and most probably caused by Faraday depolarization effects. About 10% of the nonthermal emission from M33 at 8.35 GHz is polarized, mostly due to the strong polarized emission from a magnetic arm in the north-west of the galaxy. The average total and regular magnetic field strengths in M33 are estimated as $\simeq 6.4$ and 2.5 μG , respectively.

Acknowledgment

I would like to express my deep and sincere gratitude to my supervisors, Dr. Marita Krause and Dr. Rainer Beck. Their wide knowledge and logical way of thinking, understanding, stimulating suggestions and advice made this work successful.

My sincere thanks to Dr. Endrik Krügler who guided the work concerning the interstellar dust. He was always welcoming my stupid questions.

I am grateful to Dr. Elly M. Berkhuijsen for her helpful comments, discussions and contribution.

I wish to express my warm thanks to Prof. Peter. L. Biermann for science discussions. Many thanks to Prof. Uli Klein for valuable advice and effort in reviewing this thesis. I thank Prof. Karl Menten and Prof. Richard Wielebinski for their kind advice and comments.

I acknowledge the staff of the 100-m Effelsberg telescope and the VLA for their assistance with radio observations. Thanks to Dr. Christian Henkel for helping me in radio recombination line observations. I thank members of the radio continuum group, Dr. Patricia Reich, Dr. Laura La Porta, Dr. Wolfgang Reich, and Dr. Tigran Arshakian for their support and comradeship.

I owe my sincere gratitude to Prof. Anton Zensus, the director of the Max Planck Institute für Radioastronomie, who gave me the opportunity to work and let me use all the facilities, and to Dr. Eduardo Ros, the coordinator of the International Max Planck Research School for his kind efforts and assistance. Thanks to Gabi Breuer for her sympathetic help not only in secretarial work but also in other affairs I needed a hand.

Especially, I would like to give my loving thanks to my husband, Reza Rezaei. His constant encouragement, support and strength accompanied with sweetness and love enabled me to do my best. I dedicate this thesis to him.

The financial support from the International Max Planck Research school (IMPRS) for Radio and Infrared Astronomy at the Universities of Bonn and Cologne is gratefully acknowledged.

Fatemeh Tabatabaei
Bonn, January 2008

In the context of this thesis, the following articles have been published:

Papers in Refereed Journals

1. Tabatabaei, F. S., Beck, R., Krause, M., Berkhuijsen, E. M., Gehrz, R., Gordon, K. D., Hinz, J. L., Humphreys, R., McQuinn, K., Polomski, E., Rieke, G. H., and Woodward, C. E.
A multi-scale study of infrared and radio emission from Scd galaxy M 33, *Astronomy & Astrophysics*, 2007, V. 466, p. 509
2. Tabatabaei, F. S., Krause, M., and Beck, R.
High-resolution radio continuum survey of M 33. I. The radio maps, *Astronomy & Astrophysics*, 2007, V. 472, p. 785
3. Tabatabaei, F. S. and Beck, R., Krügel, E., Krause, M., Berkhuijsen, E. M., Gordon, K. D., and Menten, K. M.
High resolution radio continuum survey of M33: II. Thermal and nonthermal emission, *Astronomy & Astrophysics*, 2007, V. 475, p. 133

Conference Proceedings

1. Tabatabaei, F., Krause, M. and Beck, R.
Spitzer images of M 33: a probe to radio-FIR correlation, *Astronomische Nachrichten*, 2005, V. 326, p. 532
2. Tabatabaei, F. S., Krause, M., Beck, R., and Berkhuijsen, E. M.
The radio-F(IR) correlation in M33 in *Turbulence in the magnetized interstellar medium*, German-Russian Open Workshop, Perm, Russia, September 2006.
3. Tabatabaei, F. S., Beck, R., Krause, M., Krügel, E., and Berkhuijsen, E. M.
Variation of the radio synchrotron spectral index in the interstellar medium of M33, *Astronomische Nachrichten*, 2007, V. 328, p. 636
4. Tabatabaei, F. S., Beck, R., Krause, M., and Berkhuijsen, E. M.
A Multi-Scale Study of IR and Radio Emission from M33, in *Formation and Evolution of Galaxy Disks*, Vatican, October 2007
5. Tabatabaei, F. S., Beck, R., Krügel, E., Krause, M., and Berkhuijsen, E. M.
Variations of the Radio Synchrotron Spectral Index in M33, in *Formation and Evolution of Galaxy Disks*, Vatican, October 2007

Contents

Abstract	i
Acknowledgement	ii
Publications	iii
Contents	v
List of Tables	ix
List of Figures	xi
1 Introduction	1
1.1 Thermal free-free emission	1
1.2 Nonthermal synchrotron emission	5
1.3 Thermal/nonthermal separation methods	7
1.3.1 Standard method	7
1.3.2 Methods based on thermal emission templates	8
1.4 Dust emission and absorption	9
1.5 M33, an ideal laboratory	9
1.6 Overview of the thesis	12
2 High-resolution radio continuum survey	15
2.1 Introduction	15
2.2 Observations and data reduction	16
2.2.1 Effelsberg single-dish observations	16
2.2.2 VLA observations	19
2.3 Results	26
2.3.1 Total intensity	26
2.3.2 Distribution of polarized emission	27
2.3.3 Integrated flux densities	28
2.3.4 Distribution of total spectral index	28
2.3.5 Integrated radio continuum spectrum	31
2.3.6 Exponential scale lengths	31
2.3.7 North–south asymmetry	33
2.4 Discussion and conclusions	34

3	Multi-scale study of radio and IR emission from M33	35
3.1	Introduction	35
3.2	Observations and data reduction	37
3.3	Wavelet analysis of IR emission	40
3.4	Spectral characteristics of IR and radio maps	43
3.5	Wavelet cross-correlations	45
3.6	Comparison with $H\alpha$	49
3.7	Discussion	50
3.7.1	IR emission	50
3.7.2	Radio emission and radio-IR correlation	51
3.7.3	Comparison with NGC 6946	52
3.8	Conclusions	53
4	Thermal and nonthermal radio emission from M33	55
4.1	Introduction	55
4.2	Data	57
4.3	Temperature distribution of dust	57
4.4	Optical depth at $160\mu\text{m}$	58
4.5	Distribution of extinction	59
4.6	Distribution of free-free emission	61
4.7	Distribution of nonthermal emission	64
4.8	Nonthermal spectral index	66
4.9	Discussion	69
4.9.1	Comparison with the standard method	69
4.9.2	Radial scale lengths	71
4.9.3	North-south asymmetry	73
4.9.4	Uncertainties	74
4.9.5	Thermal/nonthermal radio-IR correlation	75
4.9.6	Spinning dust emission	77
4.9.7	Comparison with the 49 cm data	77
4.10	Summary and conclusions	77
5	Magnetic fields in M33	81
5.1	Introduction	81
5.2	Rotation measures	81
5.3	Nonthermal degree of polarization	85
5.4	Magnetic field	86
5.5	Depolarization	89
5.6	Conclusions	93
6	Conclusions	95
A	Ionization and recombination Processes	101
B	Wavelets as a tool for scaling analysis	103
C	Effective optical depth	109

Bibliography	111
Curriculum vitae	118

List of Tables

1.1	The a factors for different frequencies and temperatures	4
1.2	Positional data on M33.	10
2.1	Characteristics and performances of the receivers of the 100-m Effelsberg telescope.	16
2.2	Central positions of the 12 fields observed with VLA at 20 cm.	23
2.3	The 11 brightest HII regions at 3.6 cm.	26
2.4	Integrated flux densities for $R < 8.5$ kpc.	28
2.5	Integrated total flux densities from Effelsberg surveys ($R < 50'$).	31
2.6	Exponential scale lengths.	32
2.7	Northern and southern integrated flux densities in total and polarized intensity	32
3.1	M33 data used in radio-IR correlation study.	37
3.2	Source subtraction thresholds	41
3.3	Fractions of the wavelet energy provided by the 11 brightest HII regions	45
4.1	Thermal flux density and thermal fraction at 3.6 cm	63
4.2	Thermal flux density and thermal fraction at 20 cm	64
4.3	Thermal fractions at 3.6 cm obtained from the new and standard methods	72
4.4	Exponential scale lengths of the thermal and nonthermal emissions	73
4.5	North-South ratios of the integrated flux densities of the thermal, nonthermal, and total radio emission	73
4.6	Average thermal fraction of M33 at 3.6 cm for different assumptions	75
5.1	Integrated nonthermal flux densities and average nonthermal degree of polarization at $180''$	85

List of Figures

1.1	Total extinction coefficient (MRN+vsg+PAH)	10
1.2	Integrated flux densities of M33 from archived data.	11
1.3	Integrated flux densities of M33 from new observations	11
1.4	M33's rotation curve	13
2.1	Total intensity and apparent B-vectors at 3.6 cm	17
2.2	Linearly polarized emission and degree of polarization at 3.6 cm	18
2.3	A sketch of the optical arms overlaid on the total and linearly polarized intensities	19
2.4	Apparent B-vectors superimposed on an optical image	20
2.5	Total intensity emission with apparent B-vectors at 6.2 cm	21
2.6	Linearly polarized emission and degree of polarization at 6.2 cm	22
2.7	Total intensity emission with apparent B-vectors at 20 cm	24
2.8	Linearly polarized emission and degree of polarization at 20 cm	25
2.9	Total spectral index map of M33	29
2.10	Total spectral index averaged in rings of 0.5 kpc	30
2.11	Radio spectrum of the integrated emission from M33	31
2.12	Radial profiles of total intensity in radio and IR	32
3.1	The radio maps of M33	37
3.2	The Spitzer IR maps of M33	38
3.3	The wavelet decomposition of IR maps	39
3.4	The wavelet spectra of the 24 and 70 μm maps	42
3.5	The wavelet spectra at 51'' resolution	42
3.6	The wavelet spectra at 84'' resolution	43
3.7	The cross-correlations in IR	46
3.8	The cross-correlation between 3.6 cm radio and IR	47
3.9	The correlation of the 20 cm radio with IR	48
3.10	The correlation of $\text{H}\alpha$ with IR	50
4.1	Dust temperature map of M33	58
4.2	Distribution of the dust optical depth	59
4.3	Radial distribution of the mean effective optical depth at $\text{H}\alpha$	60
4.4	Thermal and nonthermal maps at 3.6 cm	61
4.5	Thermal and nonthermal maps at 20 cm	62
4.6	The wavelet spectra of the 3.6 and 20 cm thermal and nonthermal emission	65
4.7	The 20 cm nonthermal map with supernova remnants	65

4.8	The nonthermal spectral index map of M33	67
4.9	Histogram of the nonthermal spectral index map	68
4.10	Mean nonthermal spectral index in rings of 0.5 kpc width	68
4.11	Thermal and nonthermal 20 cm maps obtained from the standard method	70
4.12	Radial profiles of the thermal and nonthermal intensities from the <i>new</i> separation method	71
4.13	Radial profiles of the thermal and nonthermal intensities from the <i>old</i> separation method	71
4.14	Distribution (histogram) of the thermal fraction at 3.6 cm in M33	74
4.15	The IR–thermal/nonthermal radio correlation	76
4.16	The WSRT 49 cm image of M33 at 90'' resolution.	78
5.1	Observed rotation measure maps of M33	83
5.2	Intrinsic rotation measure map of M33	84
5.3	Azimuthal behavior of RM in different rings of 1 kpc width	84
5.4	Nonthermal degree of polarization at 3.6 cm	85
5.5	Optical image of M33 with vectors of the linearly polarized emission corrected for the Faraday rotation	87
5.6	Variation of the estimated mean total and ordered magnetic field strengths in rings of 0.5 kpc	88
5.7	Distribution of the turbulent magnetic field strength, B_r (μG), in M33.	89
5.8	Thermal electron density distribution across M33	91
5.9	Depolarization in M33	92
B.1	Haar wavelet.	103
B.2	The sinusoids have infinity support but the wavelets have compact support	104
B.3	An input signal decomposed by the fourier transform.	104
B.4	An input signal decomposed by a wavelet transform.	104
B.5	Two isotropic wavelet functions	106

1 Introduction

The nonthermal synchrotron emission and the thermal free-free emission are the two main components of the radio continuum emission. Studies of the magnetic field strength and orientation are possible using the nonthermal and polarized radio continuum emission. The distribution of the cosmic ray electrons and their sources in spiral galaxies can also be inferred if the magnetic field strengths and the propagation characteristic of the electrons are known (Beck & Gr ave 1982). However, there has been a technical problem to distinguish the nonthermal and thermal components. Different methods of separation have been proposed so far, giving different results. The standard method requires accurate absolute measurements of the brightness temperature of the continuum emission at high and low frequencies and a priori knowledge of the spectral index of the nonthermal component. This method does not give a precise image of the thermal/nonthermal emission across a galaxy, as it assumes that the nonthermal spectral index is constant everywhere.

In this chapter, we review the physics of the nonthermal and thermal emission along with the existing separation techniques. We also introduce essentials of a possible separation method based on templates of the thermal emission. Finally, an overview of the thesis is presented.

1.1 Thermal free-free emission

Electrons and ions interact with each other through their electrostatic charge in an ionized gas. The most common and least interfering interaction (with the atomic structure) is when a free electron is scattered in the Coulomb field of an ion. Essentially a free electron is elastically scattered off an ion and escapes as a free electron, which is called a *free-free* transition. A photon is emitted with an energy corresponding to the difference of the outgoing to the incoming kinetic energy of the electron (i.e., $h\nu = E' - E$), according to the principle of energy conservation. We provide a brief derivation of the free-free spectrum in the following, while a more detailed treatment can be found in Jackson (1962, Sects. 13 and 15) and Lang (1999).

When a nonrelativistic electron with mass m , charge e , and velocity v passes the Coulomb field of an atom, molecule, or ion with charge $+Ze$, considered stationary, the angular deflection θ of the particle is given by (Rutherford, 1911),

$$\tan\frac{\theta}{2} = \frac{Ze^2}{mv^2b} \quad (1.1)$$

where the impact parameter b designates the perpendicular distance from the charge Ze to the original trajectory of the incoming electron. The angular deflection of the elec-

tron on its hyperbolic trajectory corresponds to an acceleration in a direction perpendicular to its original path by an amount of Δv . The total power of the electromagnetic radiation (emitted per unit time in all directions) of an accelerated point charge is

$$P = \frac{2}{3} \frac{q^2}{c^3} \left(\frac{dv}{dt} \right)^2 \quad (1.2)$$

(see Larmor 1897; for derivation, see Jackson 1962, Sect. 14).

Thus, the total power radiated by such a deflected electron is, by combining above equations, using the approximation $\Delta v \approx v \times \tan(\theta) \approx v \times 2 \tan(\theta/2)$ that results from the momentum transfer equation for elastic scattering,

$$W(\nu)d\nu \approx \frac{2e^2}{3\pi c^3} |\Delta v|^2 d\nu \approx \frac{8}{3\pi} \left(\frac{e^2}{mc^2} \right)^2 \frac{Z^2 e^2}{c} \left(\frac{c}{vb} \right)^2 d\nu, \quad \text{for } \nu < \frac{v}{b} \quad (1.3)$$

where Δv is the change in electron velocity caused by the collision.

The total rate of encounters between an electron and a volume density n_i of ions in the parameter range of $b \dots b + db$ (which is a cylindrical tube with radius b around each ion) is

$$n_i v 2\pi b db = n_i v 2\pi \frac{d\sigma_s}{d\Omega} \sin(\theta) d\theta \quad (1.4)$$

where the *differential scattering cross section* $d\sigma_s/d\Omega$ can be calculated from Eq. (1.4) and Rutherford's expression Eq. (1.1),

$$\frac{d\sigma_s}{d\Omega} = \frac{b}{\sin\theta} \left| \frac{db}{d\theta} \right| = \frac{Z^2}{4} \left(\frac{e^2}{mv^2} \right)^2 \frac{1}{\sin^4(\theta/2)}. \quad (1.5)$$

The total free-free power $P_i(v, \nu)d\nu$ radiated by a single electron in the frequency interval $\nu, \dots, \nu + d\nu$ in collisions with n_i ions is

$$P_i(v, \nu)d\nu = n_i v Q_r(v, \nu)d\nu, \quad (1.6)$$

where the *radiation cross section* $Q_r(v, \nu)$ is given by

$$Q_r(v, \nu) = \frac{16}{3} \frac{Z^2 e^6}{m^2 c^3 v^2} \int_{b_{min}}^{b_{max}} \frac{db}{b} \quad (\text{cm}^2 \text{ erg Hz}^{-1}) \quad (1.7)$$

The integral in the radiation cross section is also called *Coulomb integral* $\ln \Lambda$, or *Gaunt factor* $g(\nu, T_e)$ if multiplied with the constant $\sqrt{3}/\pi$,

$$g(\nu, T_e) = \frac{\sqrt{3}}{\pi} \ln \Lambda = \frac{\sqrt{3}}{\pi} \int_{b_{min}}^{b_{max}} \frac{db}{b} = \frac{\sqrt{3}}{\pi} \ln \left(\frac{b_{max}}{b_{min}} \right). \quad (1.8)$$

The upper limit of the impact parameter b_{max} is the mean distance between the ions or the Debye length in the plasma, while quantum mechanics determines the lower limit b_{min} . Oster (1961) arrives at

$$\frac{b_{max}}{b_{min}} = \left(\frac{2kT_e}{\gamma m} \right)^{1.5} \frac{m}{\pi \gamma Z e^2 \nu}, \quad (1.9)$$

where, $\gamma = e^C = 1.781$ and $C = 0.577$, Euler's constant, which is valid as long as $T_e > 20$ K and $\nu_{max} > 30$ GHz.

The total free-free power radiated from a thermal plasma per unit volume, unit frequency, and unit solid angle is called the *volume emissivity* ϵ_ν and is obtained by integrating the total free-free power of a single electron (Eq. 1.6) over the thermal distribution $f(v)$,

$$\epsilon_\nu = \frac{n_e}{4\pi} \int P_i(v, \nu) f(v) dv. \quad (1.10)$$

We insert the Maxwell-Boltzmann distribution of a plasma with temperature T ,

$$f(v)dv = \left(\frac{2}{\pi}\right)^{1/2} \left(\frac{m}{k_B T}\right)^{3/2} v^2 \exp\left(-\frac{mv^2}{2k_B T}\right) dv. \quad (1.11)$$

Inserting the total free-free power $P_i(v, \nu)$ Eq. (1.6) of a single electron into Eq. (1.10) and integrating over the Maxwell-Boltzmann distribution $f(v)$ in the classical free-free treatment ($h\nu = \frac{1}{2}mv^2$) yields then

$$\epsilon_\nu d\nu = \frac{8}{3} \left(\frac{2\pi}{3}\right)^{1/2} \frac{Z^2 e^6}{m^2 c^3} \left(\frac{m}{k_B T}\right)^{1/2} n_i n_e g(\nu, T) \exp\left(-\frac{h\nu}{k_B T}\right) d\nu \quad (1.12)$$

$$\approx 5.4 \times 10^{-39} Z^2 \frac{n_i n_e}{T^{1/2}} g(\nu, T) \exp\left(-\frac{h\nu}{k_B T}\right) d\nu \quad (\text{erg s}^{-1} \text{ cm}^{-3} \text{ Hz}^{-1} \text{ str}^{-1}). \quad (1.13)$$

The observable energy flux F at Earth can be derived from the emissivity $\epsilon_\nu = d\epsilon/(dt dV d\nu d\Omega)$ according to Eq. (1.12) by the following dimensional relation

$$dF = \frac{d\epsilon}{dt dA d(h\nu)} = \frac{d\epsilon}{dt (R^2 d\Omega) h d\nu} = \frac{1}{R^2 h} \frac{d\epsilon}{dt d\Omega d\nu} = \frac{dV}{R^2 h} \epsilon_\nu \quad (1.14)$$

where $h = 6.63 \times 10^{-27}$ erg s and R is the distance to the source in cgs units. Thus the observed free-free flux at Earth can be expressed as a volume integral over the source,

$$F d\nu = \int dV \frac{1}{R^2 h} \epsilon_\nu d\nu \quad (1.15)$$

$$\approx 8.1 \times 10^{-39} Z^2 \int_V \frac{n_i n_e}{T^{1/2}} g(\nu, T) \exp\left(-\frac{h\nu}{k_B T}\right) dV d\nu \quad (\text{erg s}^{-1} \text{ cm}^{-2}). \quad (1.16)$$

The absorption coefficient κ_ν can be computed according to the Kirchhoff law:

$$\kappa_\nu = \frac{\epsilon_\nu}{B_\nu(T)} = \epsilon_\nu \frac{c^2}{2h\nu^3} \left[\exp\left(\frac{h\nu}{k_B T}\right) - 1 \right], \quad (1.17)$$

Table 1.1: The a factor for different frequencies and temperatures using Eq. (1.23).

ν (GHz)	T_e (K)				
	4000	6000	7000	8000	10000
0.4	0.9972	0.9934	0.9912	0.9889	0.9844
1.4	0.9936	0.9974	0.9978	0.9977	0.9967
2.3	0.9872	0.9946	0.9962	0.9972	0.9978
10	0.9484	0.9684	0.9745	0.9792	0.9857
30	0.8957	0.9276	0.9379	0.9461	0.9582
44	0.8717	0.9084	0.9203	0.9299	0.9442
70	0.8382	0.8810	0.8952	0.9066	0.9238
100	0.8090	0.8569	0.8729	0.8858	0.9054

where $B_\nu(T)$ is the Planck function. Using the Rayleigh-Jeans approximation ($B_\nu(T) = \frac{2\nu^2}{c^2} k_B T$), we obtain the

$$\kappa_\nu = \epsilon_\nu \frac{c^2}{2\nu^2 k_B T}. \quad (1.18)$$

The optical depth is defined as

$$\tau_\nu = - \int_0^l \kappa_\nu dl, \quad (1.19)$$

where l is the line of sight path length through the emitting medium. On the other hand, the *emission measure* EM is given by

$$\frac{\text{EM}}{\text{cm}^{-6}\text{pc}} = \int_0^{l/\text{pc}} \left(\frac{N_e}{\text{cm}^{-3}} \right)^2 d \left(\frac{l}{\text{pc}} \right), \quad (1.20)$$

If we assume that the plasma is macroscopically neutral and that the chemical composition is given approximately by $N_{\text{H}} : N_{\text{He}} : N_{\text{other}} \sim 10 : 1 : 10^{-3}$, then to high accuracy $N_i = N_e$. In this case the temperature of the plasma is described as the electron temperature T_e . Then using Eqs. (1.13), (1.18), (1.19), and (1.20), the optical depth of the free-free emission at radio frequencies is

$$\tau_\nu = 3.014 \times 10^{-2} \left(\frac{T_e}{\text{K}} \right)^{-1.5} \left(\frac{\nu}{\text{GHz}} \right)^{-2} \left(\frac{\text{EM}}{\text{cm}^{-6}\text{pc}} \right) g(\nu, T_e), \quad (1.21)$$

or equivalently,

$$\tau_\nu = 8.235 \times 10^{-2} \left(\frac{T_e}{\text{K}} \right)^{-1.35} \left(\frac{\nu}{\text{GHz}} \right)^{-2.1} \left(\frac{\text{EM}}{\text{cm}^{-6}\text{pc}} \right) a(\nu, T_e), \quad (1.22)$$

with

$$a = 0.366 \nu_{\text{GHz}}^{0.1} T_e^{-0.15} [\ln(4.995 \times 10^{-2} \nu_{\text{GHz}}^{-1}) + 1.5 \ln(T_e)] \simeq 1, \quad (1.23)$$

(Altenhoff et al. 1960; Mezger & Henderson 1967). Exact values of the a factor are given in Table 1.1 for a number of frequencies between 0.4 GHz and 100 GHz and electron temperatures between 4000 K and 10,000 K.

1.2 Nonthermal synchrotron emission

Relativistic electrons gyrating in a magnetic field emit synchrotron radiation in the radio regime. Supernova remnants are considered as famous sources of this kind of emission. Generally, when an electron with the charge e and mass m moves at a relativistic velocity \mathbf{v} across a magnetic field \mathbf{B} , it spirals along the direction of \mathbf{B} . If the electron has a velocity component parallel to the magnetic field, it will move in a helix with a pitch angle ψ given by

$$\tan\psi = \frac{v_{\perp}}{v_{\parallel}}, \quad (1.24)$$

where v_{\perp} and v_{\parallel} are the magnitude of the velocity components perpendicular and parallel to \mathbf{B} .

The direction of the acceleration vector continually changes in the plane perpendicular to the field lines with a magnitude of

$$a_{\perp} = \frac{eB}{\gamma m} v_{\perp}, \quad (1.25)$$

with $\gamma = (1 - \frac{v^2}{c^2})^{-1/2}$ the Lorentz factor. The total amount of power radiated by the accelerated charged particle in the laboratory frame is given by

$$P = \frac{2e^2}{3c^3} \gamma^4 a_{\perp}^2, \quad (1.26)$$

Considering the total energy of $E = \gamma m c^2$, the power emitted by a relativistic particle is

$$P = \frac{2e^4 v_{\perp}^2 B^2}{3m^2 c^3} \left(\frac{E}{mc^2} \right)^2 = \sigma_{\text{T}} \gamma^2 c u_B, \quad (1.27)$$

where $u_B = B^2/4\pi$ is the energy density deposited in the magnetic field and $\sigma_{\text{T}} = 6.65 \times 10^{-25} \text{ cm}^2$ the Thomson cross section.

In the electron's rest frame, because the acceleration is directed perpendicular to the direction of motion, the power pattern of the emission will be that of a dipole field with the dipole oriented along the direction of the acceleration. This power P' has an angular distribution given by

$$\frac{dP'(\vartheta, \varphi)}{d\Omega} = \frac{1}{4\pi} \frac{e^2}{c^3} (a'_{\perp})^2 (1 - \sin^2 \vartheta \cos^2 \varphi).$$

In the laboratory frame, this becomes

$$\frac{dP(\vartheta, \varphi)}{d\Omega} = \frac{1}{4\pi} \frac{e^2}{c^3} (a'_{\perp})^2 \frac{1}{(1 - \beta \cos \vartheta)^3} \left[1 - \frac{\sin^2 \vartheta \cos^2 \varphi}{\gamma^2 (1 - \beta \cos \vartheta)^2} \right].$$

In the ultrarelativistic case, when $\beta \simeq 1$, no radiation is emitted towards $\vartheta = 0, \pi$. For these directions, we have $u'_{\perp} = \pm c$ and $u'_{\parallel} = 0$, and in the laboratory frame they subtend the angle

$$\tan \theta = \frac{u_{\perp}}{u_{\parallel}} = \frac{c}{\gamma v} = \frac{1}{\gamma}.$$

Hence, the power P is confined to a cone with the angle θ , providing a strong beaming effect.

The total emissivity of an electron of Energy E with $\gamma \gg 1$ (given by Westfold 1959; Pacholczyk 1970) is

$$P(\nu, E) = \sqrt{3} \frac{e^3 B \sin \psi}{mc^2} \frac{\nu}{\nu_c} \int_{\nu/\nu_c}^{\infty} K_{5/3}(\eta) d\eta. \quad (1.28)$$

$K_{5/3}$ is the modified Bessel function of 5/3 order and the critical frequency

$$\nu_c = \frac{3}{4\pi} \gamma^2 \frac{eB}{m} \sin \psi$$

. Then the *volume emissivity* (power per unit frequency interval, per unit volume, and per unit solid angle) of N relativistic electrons would be

$$\epsilon(\nu) = \int_E P(\nu, E) N(E) dE, \quad (1.29)$$

where $N(E) dE$ is the number of electrons per unit volume and per unit solid angle moving in the direction of the observer and whose energies lie in the range E and $E + dE$.

According to the cosmic ray data, $N(E)$ is well described by a power law spectrum,

$$N(E) dE = A E^{-\delta} dE, \quad (1.30)$$

for $E_1 < E < E_2$ and A is a constant. Substituting (1.28) and (1.30) in (1.29),

$$\epsilon(\nu) \sim \nu^{(1-\delta)/2} = \nu^{-\alpha_n}, \quad (1.31)$$

with $\alpha_n \equiv \frac{1}{2}(\delta - 1)$. This means that the nonthermal emission can be described as a power law with an index α_n . If we assume that the synchrotron emission arises from a region in which the magnetic field is uniform in strength and orientation (regular) and which extends for the depth L_u along the line of sight, the total intensity (provided a small optical depth, Lang 1999) is

$$I(\nu) = a(\alpha_n) A L_u \frac{\sqrt{3}}{8\pi} \frac{e^3}{mc^2} \left[\frac{3e}{4\pi m^3 c^5} \right]^{\alpha_n} B_{u,\perp}^{\alpha_n+1} \nu^{-\alpha_n}, \quad (1.32)$$

where $B_{u,\perp} = B_u \sin \psi$, and

$$a(\alpha_n) = 2^{\alpha_n-1} \frac{\alpha_n + 5/3}{\alpha_n + 1} \Gamma\left(\frac{3\alpha_n + 1}{6}\right) \Gamma\left(\frac{3\alpha_n + 5}{6}\right). \quad (1.33)$$

If the magnetic field is random which extends for the depth L_r along the line of sight, then

$$I(\nu) = b(\alpha_n) A L_r \frac{\sqrt{3}}{8\pi} \frac{e^3}{mc^2} \left[\frac{3e}{4\pi m^3 c^5} \right]^{\alpha_n} B_r^{\alpha_n+1} \nu^{-\alpha_n}, \quad (1.34)$$

with

$$b(\alpha_n) = 2^{\alpha_n-4} \sqrt{\frac{3}{\pi}} \frac{\Gamma\left(\frac{3\alpha_n+1}{6}\right) \Gamma\left(\frac{3\alpha_n+11}{6}\right) \Gamma\left(\frac{\alpha_n+3}{2}\right)}{(\alpha_n + 1) \Gamma\left(\frac{\alpha_n+4}{2}\right)}. \quad (1.35)$$

In realistic situations, the magnetic field is a combination of both uniform and random fields. Hence using (1.32) and (1.34), the total observed nonthermal intensity in Jy str^{-1} units is given by

$$I(\nu) = A \left(\frac{\nu}{\text{GHz}} \right)^{-\alpha_n} \left(0.933 a(\alpha_n) L_u B_{u,\perp}^{\alpha_n+1} + 13.5 b(\alpha_n) L_r B_r^{\alpha_n+1} \right) (6.26 \times 10^9)^{\alpha_n}. \quad (1.36)$$

Since the acceleration of the gyrating electron has no component parallel to the magnetic field, the instantaneous emission is elliptically polarized, but as the position angle of the polarization ellipse is rotating with the electron, the time-averaged polarization is linear. The average radiation of monoenergetic relativistic electrons is also linearly polarized provided the magnetic field is homogeneous. The details are given by Westfold (1959), Ginzburg et al. (1965), and Pacholczyk (1970). For an ensemble of relativistic electrons with a power law distribution of energies in a uniform magnetic field, the degree of linearly polarization is given by

$$p = \frac{3\alpha_n + 3}{3\alpha_n + 5}. \quad (1.37)$$

However, due to depolarization effects, the observed degree of polarization is always lower than the theoretical degree of polarization. Followings, we review the thermal/nonthermal separation methods mostly used so far. Then we propose a possible separation technique for the radio continuum emission from external galaxies.

1.3 Thermal/nonthermal separation methods

1.3.1 Standard method

The standard method is based on the continuum data at radio wavelengths. The spectral index of the nonthermal emission (α_n) serves as a free parameter and it is assumed to be constant with location of the radio continuum emission across the object. The nonthermal spectral index (together with the thermal fraction f_{th}) is found either by fitting the following model to the mean integrated radio spectra (eg. Niklas et al. 1997),

$$\frac{S_{\nu_2}}{S_{\nu_1}} = f_{th}^{\nu_1} \left(\frac{\nu_2}{\nu_1} \right)^{-0.1} + (1 - f_{th}^{\nu_1}) \left(\frac{\nu_2}{\nu_1} \right)^{-\alpha_n}, \quad (1.38)$$

or by taking the spectral index of the total radio continuum emission from regions where the nonthermal emission is dominant (like outer parts and interarm regions of a galaxy) as α_n (e.g. Klein et al. 1982; Berkhuijsen et al. 2003). This method has been used for both global and local studies. Separation of thermal and nonthermal components in global studies is done to obtain integrated thermal/nonthermal flux densities for an object (e.g. Klein et al. 1984; Niklas et al. 1997; Dumke et al. 2000). In the local studies the aim of separation is usually to find the distribution of thermal/nonthermal emission across an object (eg. Beck & Gräve 1982; Tilanus et al. 1988; Buczylowski 1988). More details about the standard method can be found in Chapter 4.

1.3.2 Methods based on thermal emission templates

IR emission

Although Infra-Red (IR) fluxes from normal galaxies are commonly taken to indicate the rate of recent star formation, one may use it as a tracer for the thermal emission, too, especially at wavelengths that the IR is powered predominantly by HII regions. Recently, the Spitzer 24 and 70 μm observations of M33 have shown that these bands follow closely the structure of the ionized gas. Their distributions are very similar to the distribution of the $H\alpha$ flux (Hinze et al. 2004; Gordon et al. 2004a).

Broadbent et al. (1989) proposed a separation technique based on the correlation of radio continuum with 60 μm IR emission. The problem with this technique is that it uses the radio-IR correlation to estimate the thermal emission, i.e. it neglects probable role of the nonthermal emission in the radio-IR correlation. However, it is possible that star forming regions as important energy sources of IR emission emit also strong nonthermal emission (See Chapter 4) or be influenced by the magnetic field. It is also possible that the IR emission be stimulated by the nonthermal processes e.g. by super massive black holes in center of galaxies. Therefore, this method may only be used at places where the radio emission is most probably thermal (like HII regions).

Hydrogen recombination lines

The thermal free-free emission of electrons emerges from photo-ionized gas surrounding hot stars like HII regions or diffuse ionized medium. As far as there is a balance between heating (ionization) and cooling (recombination) mechanisms in these regions, Hydrogen recombination lines are good tracers for the free-free emission. Hydrogen lines have a coverage from the optical wavelengths: Balmer series, to the radio wavelengths: Radio Recombination Lines (RRLs).

To get images in the optical (Balmer) and near-infrared (Paschen and Brackett) lines, observations can be made with an optical telescope equipped with an optical and/or near-infrared CCD camera. Investigating objects in these wavelengths, one needs to be conscious about extinction from both the foreground galaxy and the interior of the external galaxies, caused by the dust grains.

The RRLs are extinction-free and can be detected by means of radio telescopes. However, the weak intensity of the RRLs makes it very difficult to detect them, particularly from diffuse ionized medium.

Among the hydrogen lines, the strength of the $H\alpha$ line is high enough to map both diffuse and compact structures. Therefore, regarding to the possible detecting power of the existing telescopes, the $H\alpha$ emission can be used as the only accessible thermal template for external galaxies. To correct the observed $H\alpha$ flux density it is necessary to know about emitting and absorbing mechanisms of dust grains. We develop a separation method based on the de-extincted $H\alpha$ (this method is referred to as the ‘new method’) and apply it to the nearby galaxy M33.

1.4 Dust emission and absorption

A dust grain in a radiation field may acquire an equilibrium temperature T_d which is determined by the condition that it absorbs energy per second as much as it emits. According to Kirchhoff, in local thermodynamic equilibrium (LTE) the ratio of the emission coefficient (ϵ_ν) to the absorption coefficient (κ_ν) is only a function of temperature and frequency. Although the interstellar space may not be counted as an LTE environment, a grain heated in this medium (say by a photon) distributes very rapidly the excess energy among its many energy levels. The resulting distribution of energy states and hence the grain emission depends only on the dust temperature T_d , as in LTE, $\epsilon_\nu = \kappa_\nu B_\nu(T_d)$.

As the main source of attenuation, dust grains have been extensively studied theoretically and experimentally. So far, significant knowledge about the chemical composition of the dust grains, their sizes and size distribution in the interstellar medium have been obtained. Mathis et al. (1977) showed that a pure (unmixed) composition of silicate and amorphous carbon grains with sizes between 0.02 and 0.3 μm and a power law size distribution (as explained by Biermann & Harwit 1980) fits observational data on interstellar extinction (this kind of grains is known as MRN that stands for Mathis, Rumpl, and Nordsieck 1977). These grains attain a constant temperature in any radiation field. The absorption coefficient is given by $\kappa_\nu \propto \nu^\beta$ with $1 < \beta < 2$. The relevant range of emission (and absorption) of these grains is $\lambda > 10 \mu\text{m}$. The big grains are mostly responsible for the extinction as most of the solid matter of the interstellar medium resides in these grains.

Besides the big grains, a more realistic dust model includes also very small grains (vsg) with sizes smaller than 0.01 μm , and polycyclic aromatic hydrocarbon (PAH) grains. The temperature of these grains fluctuates violently, so no thermal equilibrium condition can be used. The so called ‘standard’ dust is based on the three dust components, MRN+vsg+PAH (that is also considered in this work). The total extinction coefficient of the standard dust as a function of wavelength is shown in Fig. 1.1 (which is more or less identical to that of the MRN, except at far UV wavelengths, Krügel 2003). As the vsg and PAH grains have small contribution in far-IR regime ($\lambda > 40 \mu\text{m}$), the dust emission and absorption can be treated using the Kirchhoff law (i.e. LTE assumption).

1.5 M33, an ideal laboratory

M33, the Triangulum galaxy ($l = 133^\circ.6$ and $b = -31^\circ.3$) is the third brightest Local Group galaxy with an integrated luminosity of $M_v = -18.9$. It is a late type spiral, Scd, with two open spiral arms (and 8 fainter arms) and no clear evidence of any bulge component (Bothun & Rogers 1992; Minniti et al. 1993; McLean & Liu 1996). The mass to light ratio of its nucleus is small ($M/L < 0.4$), ruling out the presence of a supermassive black hole (Kormendy & McClure 1993; Lauer et al. 1998). Like many nearby spiral galaxies, M33 shows a large-scale warp in its outer HI disk. The inclination of the arms and of the optical disk to the plane of the sky increases outward from $\simeq 40^\circ$ near the center to $\simeq 70^\circ$ at a radius of $\simeq 6 \text{ kpc}$ (Sandage & Humphreys 1980). With a metallicity of $[\text{Fe}/\text{H}] \simeq -1.5$ in the halo and $[\text{Fe}/\text{H}] \simeq -0.9$ in the disk, M33 has a lower metallicity (and is $\simeq 10$ times less massive) than M31 and the Milky Way (McConnachie

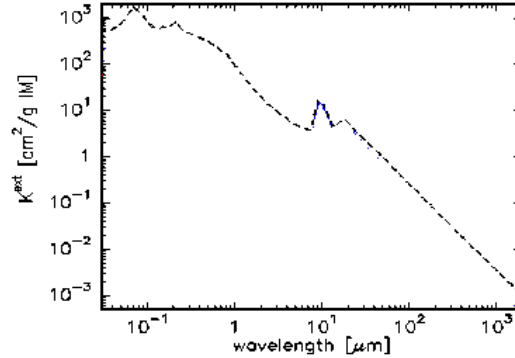


Figure 1.1: Total extinction coefficient (MRN+vsg+PAH) as a function of wavelength for the dust model of diffuse medium (see Krügel 2003).

Table 1.2: Positional data on M33.

Nucleus position (J2000)	RA = $1^h 33^m 51.0^s$ DEC = $30^\circ 39' 37.0''$	de Vaucouleurs & Leach (1981)
Position angle of major axis	23°	Deul & van der Hulst (1987)
Inclination	56°	Regan & Vogel (1994)
Distance ($1'' = 4$ pc)	840 kpc	Freedman et al. (1991)
Optical extent	$60' \times 35'$	

et al. 2006). M33 has been forming stars continuously for most of its lifetime with a rate of $\simeq 0.5 M_\odot/\text{yr}$, with the stellar populations older than 8–10 Gyr in its central regions, about 5–7 Gyr in the outer regions, and less than 3–5 Gyr in the spiral arms (Li et al. 2004).

Because of its proximity, favorite inclination and apparent size (not so large as M31 and not so small as other nearby galaxies), M33 is an ideal nearby galaxy to study astrophysical properties globally and locally. Table 1.2 summarizes the positional characteristics of M33. Fig. 1.2 shows total flux densities of M33 at different wavelengths from archives, and Fig. 1.3 new IR and radio integrated fluxes from our recent observations.

Different components that contribute to the gravitational potential of this galaxy are:

(a) *Stellar disk*

A thin disk is the main stellar component since the central bulge is very small and can be completely neglected. For the stellar disk there is an exponential scale-length of $R_d \simeq 1.4 \pm 0.2$ kpc (Regan & Vogel 1994), as measured in the K-band. M33 is an extremely blue galaxy having $(B - V)_T^0 = 0.46$ (de Vaucouleurs et al. 1991). The total blue luminosity in units of blue solar luminosity is $L_B = 4.2 \times 10^9 L_\odot$ (Sandage & Tammann 1981). The total stellar mass estimated is $\simeq 5 \times 10^9 M_\odot$.

(b) *Atomic gas*

Most of the gaseous mass in M33 is in the form of neutral atomic hydrogen. The results of the detailed survey of the outer disk and of the tilted-ring model fitted to the 21-cm line data have shown a radial extent of the HI, $\simeq 16$ kpc, which is more than 13

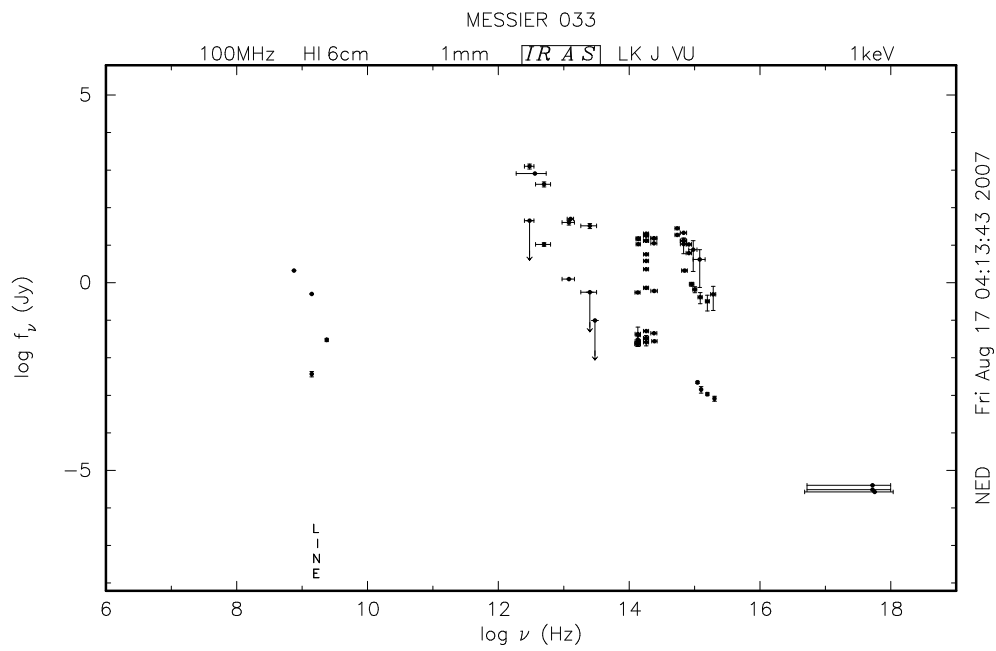


Figure 1.2: Integrated flux densities of M33 from archived data.

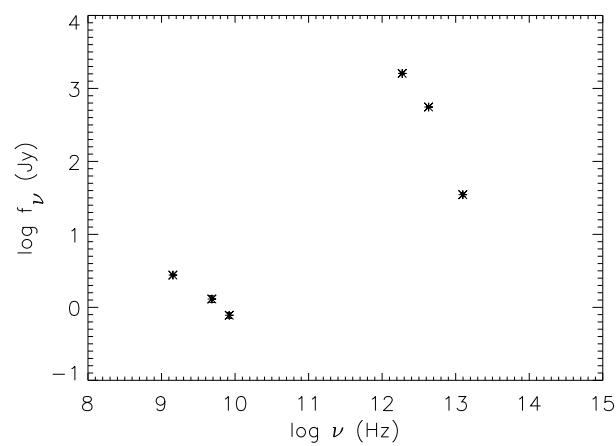


Figure 1.3: Integrated flux densities of M33 from new observations in radio and IR.

times the exponential scale-length of the stellar disk. The outer disk of neutral hydrogen in M33 is warped and oriented at $\sim 30^\circ$ with respect to the inner disk and the global H profile of the outer disk appears symmetric on the low and high velocity wings. The total HI mass is estimated to be $1.8 \times 10^9 M_\odot$ (Corbelli & Schneider 1997).

(c) *Warm ionized gas*

If the background ionizing radiation accounts for the sharp HI fall off seen in the outer disk around $3 \times 10^{19} \text{ cm}^{-2}$ (Corbelli & Salpeter 1993), a similar amount of ionized gas is expected to lie above and below the whole HI disk since this is exposed to the same background radiation field. Taking a column density of ionized gas equal to $3 \times 10^{19} \text{ cm}^{-2}$ ($\sigma_{\text{HII}} = 0.26 M_\odot \text{ pc}^{-2}$) throughout the HI disk, Corbelli & Salucci (2000) obtained an HII mass of $1.9 \times 10^8 M_\odot$. The detailed radial distribution of the warm ionized gas is unknown.

(d) *Molecular gas*

M33 is known to be a galaxy deficient in molecular gas. Maps of the diffuse CO component and interferometric studies show that molecules are not a dominant component of the global gas mass fraction, although individual large molecular complexes with masses of order $10^{5-6} M_\odot$ are prominent in the nuclear region (e.g. Young & Scoville 1982). Within the first kiloparsec the derived H_2 column density is radially constant and of the same order of the HI column density, but at larger radii it drops rapidly. At 2.5 kpc the H_2 mass is $6 \times 10^7 M_\odot$, about half of the HI mass.

Thus, the HI disk accounts for a substantial fraction of the total baryonic mass, and the gas total mass ($\sim 3 \times 10^9 M_\odot$, including helium, molecular hydrogen, atomic neutral and ionized hydrogen) is of the same order of the stellar mass. This implies that ~ 50 per cent of the gas has turned into stars in M33.

(d) *Dark matter*

The rotation curve of M33 (Fig. 1.4) implies a dark halo mass of $\geq 5 \times 10^{10} M_\odot$. The observed rotation curve shows that $V(R)$ increases by $\sim 20 \text{ km s}^{-1}$ across the region $3 \text{ kpc} < R < 8 \text{ kpc}$ and by $\sim 10 \text{ km s}^{-1}$ from 8 to 16 kpc. This indicates that the M33 mass distribution is largely dominated by a non-luminous component down to $R \sim 3 \text{ kpc}$. Results of the best fit to the mass distribution also show that the dark halo controls the gravitational potential from 3 kpc outward, with a matter density which decreases radially as $R^{-1.3}$ (Corbelli & Salucci 2000). No obvious correlation has been found between the radial distribution of dark matter and the distribution of stars or gas.

In M33, the predicted supernova rate is one per 140-250 yr, in general agreement with the absence of historical supernovae (Duric et al. 1995). No satellite has been found for M33, probably due to the strong gravitational force of its neighbor, M31, that is 10-times more massive than M33.

1.6 Overview of the thesis

In this thesis, we develop a new method to separate the thermal and nonthermal components of the radio continuum emission from M33. This method is capable of producing a map for the nonthermal spectral index, hence, makes it possible to study different phases of propagation of cosmic ray electrons through the galaxy.

The resulting thermal and nonthermal distributions help us for a better understanding

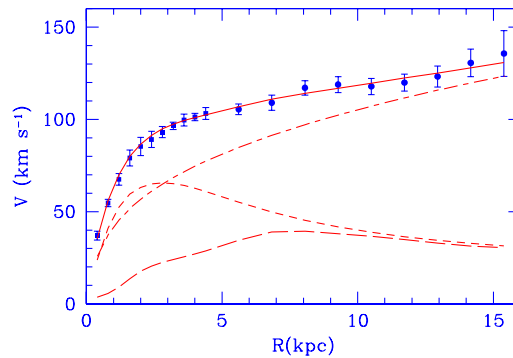


Figure 1.4: M33 rotation curve (points) compared with the best fit model by Corbelli & Salucci (2000)(solid line). Also shown are the halo contribution (dashed-dotted line), the stellar disk (short dashed line) and the gas contribution (long dashed line).

of the origin of the radio–IR correlation in M33. Furthermore, the nonthermal spectral index map provide a more precise measurement of the magnetic field strength across this galaxy.

The thesis is organized as follows:

- In Chapter 2, new radio continuum survey of M33 at 3.6 cm (8.35 GHz), 6.2 cm (4.85 GHz), and 20 cm (1.42 GHz) is presented. Using these data, we investigate distributions of the total power and polarized intensity, spectral index, and radial scale lengths. Chapter 2 was published in *Astronomy & Astrophysics* (Tabatabaei et al. 2007c).
- Chapter 3 presents a thorough analysis of IR emission from M33 and its correlation with radio emission considering different spatial scales of emission. We take *wavelet transform* of the Spitzer IR maps at 24, 70, and 160 μm and study their wavelet spectra and cross-correlations with maps of the radio 3.6 and 20 cm and also $\text{H}\alpha$. This Chapter was published in *Astronomy & Astrophysics* (Tabatabaei et al. 2007a).
- Chapter 4 describes the new thermal/nonthermal separation method, where the standard method is also used and the results from the two methods are compared. This Chapter was published in *Astronomy & Astrophysics* (Tabatabaei et al. 2007b).
- Chapter 5 gives a high-resolution Faraday rotation measure map of M33. Distributions of the nonthermal degree of polarization, Faraday depolarization, and turbulent magnetic field strength are also presented. Furthermore, regular and total magnetic field strengths are determined in rings in the galactic plane.
- In Chapter 6, we summarize the main conclusions of the thesis.

2 High-resolution radio continuum survey

2.1 Introduction

The nearest Scd galaxy at a distance of 840 kpc ($1'' \simeq 4$ pc, Freedman et al. 1991), M33 (NGC 598) has been extensively studied at radio wavelengths. Terzian & Pankonin (1972) detected some diffuse emission at 318 and 606 MHz using angular resolutions of $17'$ and $10'$, respectively. Israel & van der Kruit (1974) observed M33 at 1415 MHz with the Synthesis telescope in Westerbork (WSRT). However, they did not find any extended spiral arm emission. This emission was first revealed by observations with the 100-m Effelsberg dish at 6.2 cm (von Kap-Herr et al. 1978) that was extensively studied by Berkhuijsen (1983). Radio polarization observations of M33 were first made by Beck (1979) at 21.1 cm and 11.1 cm. Buczilowski & Beck (1987) observed this galaxy at 17.4 cm, 6.3 cm, and 2.8 cm. They detected polarization mostly in the northern half of M33 and proposed a bisymmetric magnetic field structure. The next interferometer observations (Duric et al. 1993; Viallefond et al. 1986a; Gordon et al. 1999) were carried out in total intensity to study point sources like HII regions and supernova remnants (SNRs) within M33.

Generally, single-dish observations should be carried out to study the extended radio emission. So far, single-dish observations have been limited by sensitivity because M33 is relatively weak in radio emission, especially in polarized emission (with an integrated flux density of ~ 83 mJy at 6.2 cm, Buczilowski & Beck 1991), and because of M33's large extent in the sky.

This paper is the first in a series providing a detailed investigation of the radio continuum emission of M33. We describe new observations of the radio continuum emission at 3.6 cm, 6.2 cm, and 20 cm with much improved detection limits of total and polarized intensity and with higher spatial resolutions. These data allow a much more detailed study of polarization and the magnetic field within M33 than was possible before. We discuss the distribution and degree of linear polarization, integrated flux densities and distribution of the total spectral index (obtained from total intensities of the radio continuum emission including both thermal and nonthermal emission). We also compare the radial, exponential scale lengths of the radio emission at different wavelengths.

The observations and data reduction are described in Sect. 2.2. Results, including distributions of total intensity and polarization, integrated flux densities, and total spectral index distribution, are discussed in Sect. 2.3. Discussion and concluding remarks are presented in Sect. 2.4.

Table 2.1: Characteristics and performances of the receivers of the 100-m Effelsberg telescope.

λ (cm)	3.6	6.2
Center frequency (GHz)	8.350	4.850
Band width (MHz)	1100	500
HPBW (")	83.6	146
T_{sys} (K)	23-25	25-28
T_b/S_ν (K/Jy)	2.62	2.4

2.2 Observations and data reduction

We performed both single-dish and interferometer observations. The single-dish observations at 3.6 cm and 6.2 cm were made with the 100-m Effelsberg telescope¹. The interferometer observations at 20 cm were carried out with the Very Large Array (VLA²).

2.2.1 Effelsberg single-dish observations

We observed M33 at 3.6 cm during several periods from August 2005 to March 2006 with the broadband system (bandwidth ~ 1100 MHz) centered at 8350 MHz. The receiver is a dual-channel correlation radiometer with cooled HEMT amplifiers and a cooled polarization transducer located in the secondary focus of the 100-m telescope. The system is set up for receiving left hand circular (LHC) and right hand circular (RHC) polarization. M33 was scanned along RA and DEC with a scanning velocity of 50'/min on a grid of 30". The scanned area of 40' \times 50' was centered on the nucleus of the galaxy. The total observing time was about 100 hours. We obtained 56 coverages with a typical sensitivity per scan of 2 mJy/beam area in total intensity and 0.4 mJy/beam area in polarization. The half power beam width (HPBW) at 3.6 cm is 83.6" which corresponds to a linear resolution of about 335 pc.

The sources 3C 48, 3C 286, and 3C 138 were used for pointing and focusing during the observations. Calibration of the flux density and polarization angle was achieved by observing 3C 286. We used the flux density scale given by Baars et al. (1977).

The data reduction was performed in the NOD2 data reduction system (Haslam 1974). In order to remove the scanning effects due to ground radiation, weather condition, and receiver instabilities, we applied the scanning removal program, *Presse*, of Sofue & Reich (1979). The r.m.s. noise after combination of the coverages (Emerson & Graeve 1988) is ~ 220 μ Jy/beam in Stokes I (total intensity) map and ~ 70 μ Jy/beam in Stokes U and Q (polarization) maps. The final maps in U and Q were combined to produce maps in polarized intensity and in polarization angle, correcting for the positive bias in polarized intensity due to noise (Killeen et al. 1986). Figures. 2.1 and 2.2 show the resulting maps of the total and polarized intensities, respectively, smoothed to an angular resolution of 120".

¹The 100-m telescope at Effelsberg is operated by the Max-Planck-Institut für Radioastronomie (MPIfR) on behalf on the Max-Planck-Gesellschaft.

²The VLA is a facility of the National Radio Astronomy Observatory. The NRAO is operated by Associated Universities, Inc., under contract with the National Science Foundation.

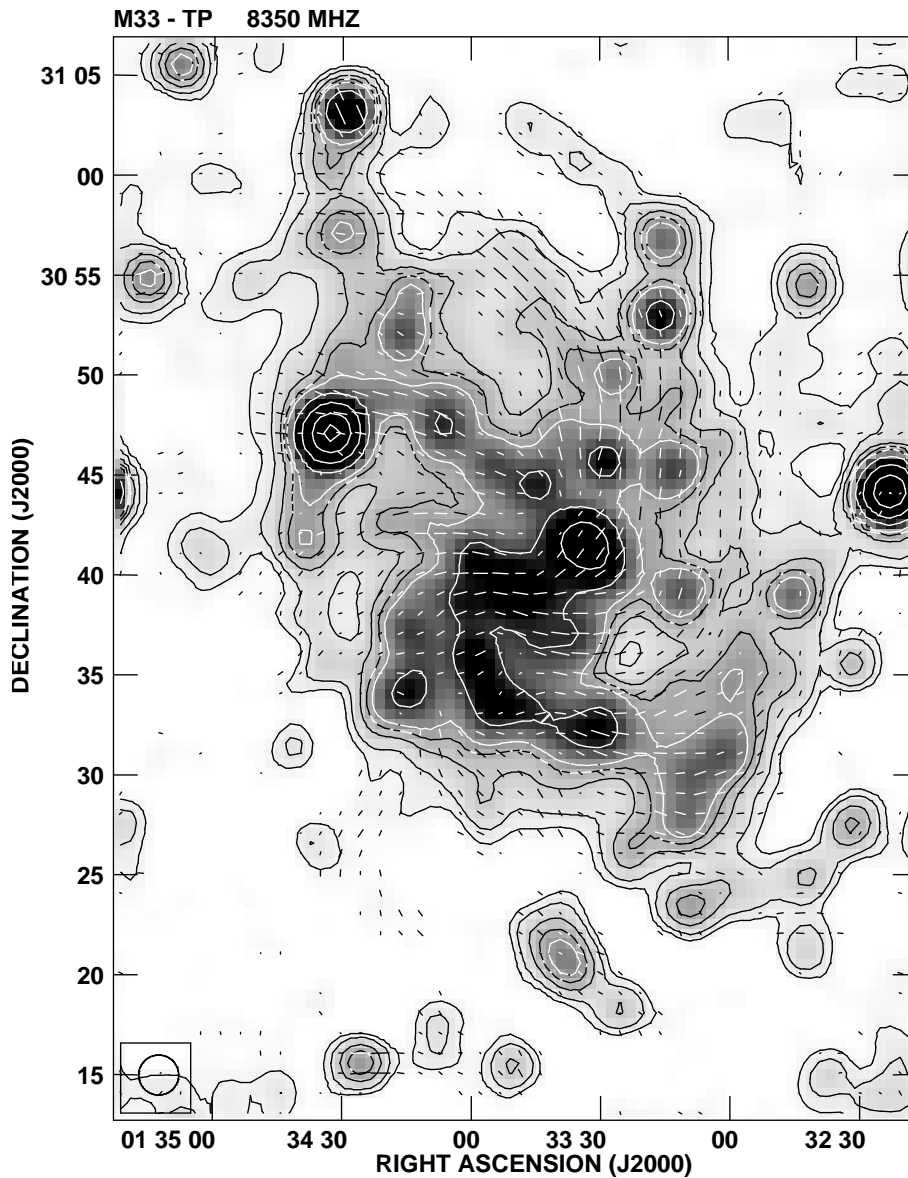


Figure 2.1: Total intensity emission from M33 at 3.6 cm observed with the Effelsberg telescope, with apparent B-vectors (E-vectors rotated by 90°) of polarized intensity superimposed. The HPBW is $120''$ (the beam area is shown in the left-hand corner). Contour levels are 0.5, 1, 2, 3, 4, 8, 16, 32, 64 mJy/beam. The r.m.s. noise is 0.14 mJy/beam in total intensity and 0.04 mJy/beam in linear polarization. The vectors were plotted starting from 0.1 mJy/beam (2.5σ). A vector length of $1'$ represents a polarized intensity of 0.5 mJy/beam. The FITS data of the 3.6 cm total intensity is available at the CDS.

Observations at 6.2 cm were carried out in the summer of 1996 using the 4850 MHz HEMT receiver installed in the secondary focus of the 100-m Effelsberg telescope. This is a 4-channel, 2-beam system with cooled HEMT pre-amplifiers (see Table 2.1 for more information about this receiver). M33 was scanned along its major axis and perpendicular

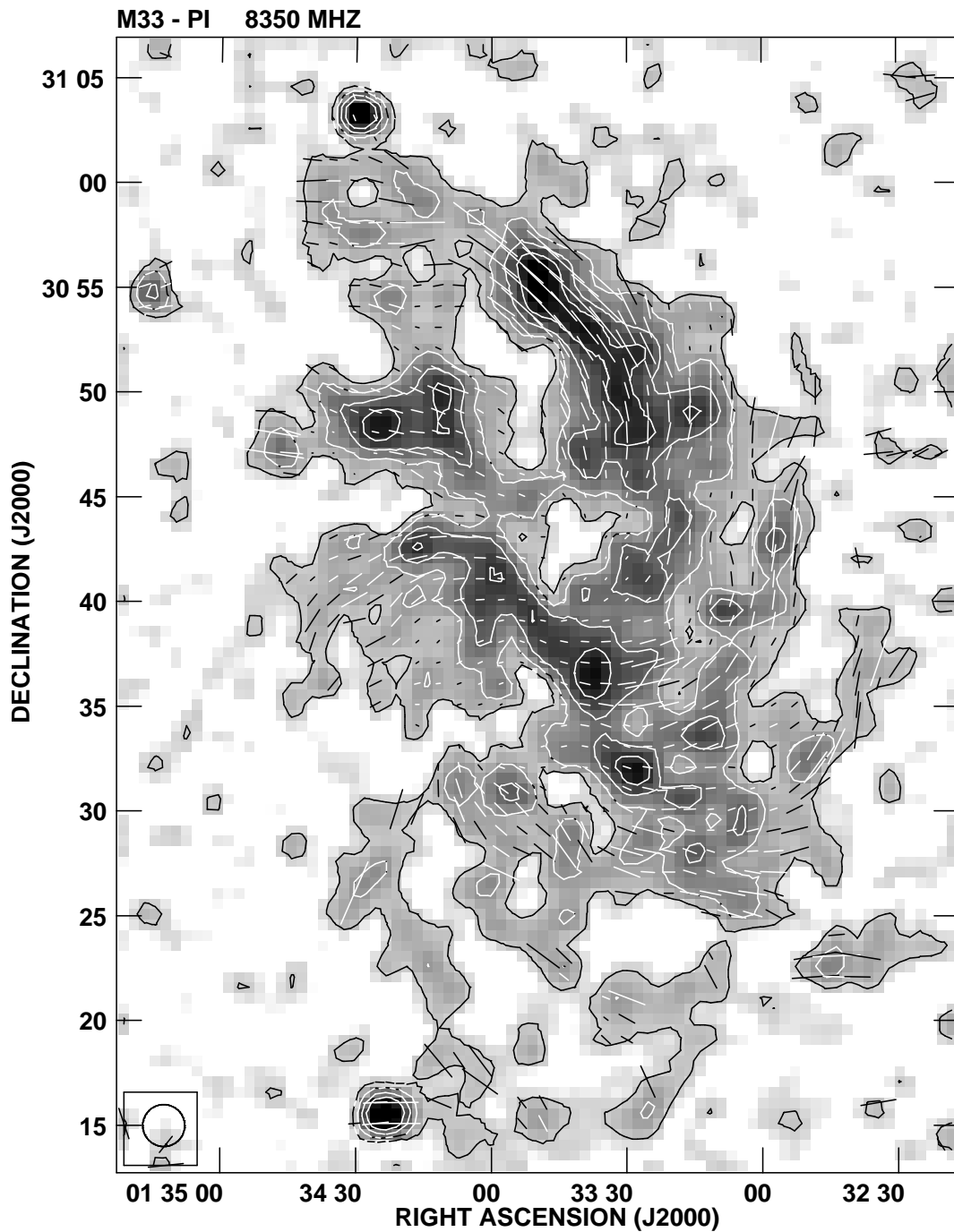


Figure 2.2: Linearly polarized emission (contours and grey scale) and degree of polarization (vector lengths) from M33 at 3.6 cm observed with the Effelsberg telescope, smoothed to an angular resolution of $120''$ (the beam area is shown in the left-hand corner). Position angles of the vectors show the orientation of the apparent magnetic field component perpendicular to the line of sight. Contour levels are 0.1, 0.2, 0.3, 0.4 mJy/beam. The r.m.s. noise is 0.04 mJy/beam. A vector length of $1'$ represents a degree of polarization of 12.6%.

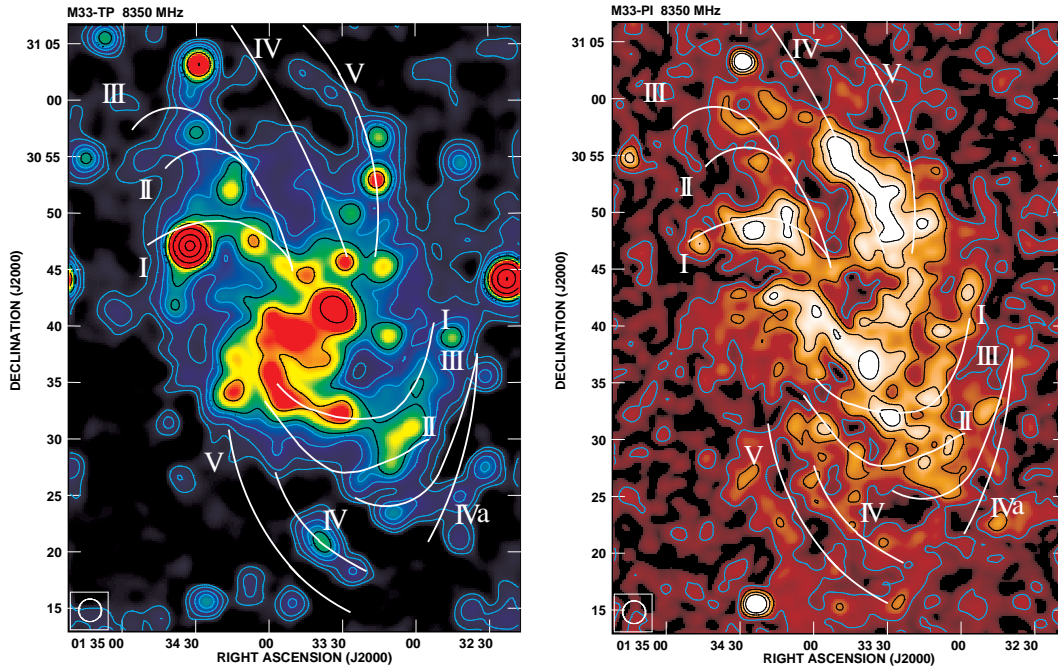


Figure 2.3: A sketch of the optical arms (Sandage & Humphreys 1980) overlaid on the total (left panel) and linearly polarized (right panel) intensities at 3.6 cm (cover illustration, *Astronomy & Astrophysics*, Vol. 472). Grey scales and contour levels are the same as in Figs. 2.1 and 2.2.

to it on a grid of $1'$ with a scanning velocity of $90'/\text{min}$. The field size is $100' \times 80'$. The number of useful coverages is 12 for Stokes I maps and 14 for each of the U and Q maps. The 6.2 cm data reduction was performed similar to that at 3.6 cm. The r.m.s. noise after combination is $\sim 700 \mu\text{Jy}/\text{beam}$ in Stokes I (total intensity) map and $\sim 180 \mu\text{Jy}/\text{beam}$ in Stokes U and Q (polarization) maps. The final maps of total and polarized intensities (smoothed to $180''$) are shown in Figs. 2.5 and 2.6, respectively.

2.2.2 VLA observations

We observed M33 at 20 cm (L-band) in two 50 MHz bands centered at 1385 and 1465 MHz with dual circular polarization in the continuum mode of the VLA D-array. The observation dates were 06-11-05, 07-11-05, 08-11-05, 13-11-05, and 06-01-06. To cover the central $30' \times 45'$ with equal sensitivity, we made a mosaic with 12 pointings with a spacing of half the primary beam width, $15'$, (3 pointings along RA and 4 pointings along DEC). The coordinates of the 12 pointings are listed in Table 2.2. The observations were made in cycles with 6 min on each pointing of the mosaic. This observing cycle was repeated 17 times. At the beginning and end of each 4-cycle, we observed 3C 138 and 3C 48 as the primary flux density calibrators. The antenna gains and phases were calibrated every 43 min with the phase calibrator 0029 + 349. The source 3C 138 was also used for polarization calibration.

The standard procedures of the Astronomical Image Processing System (AIPS) were

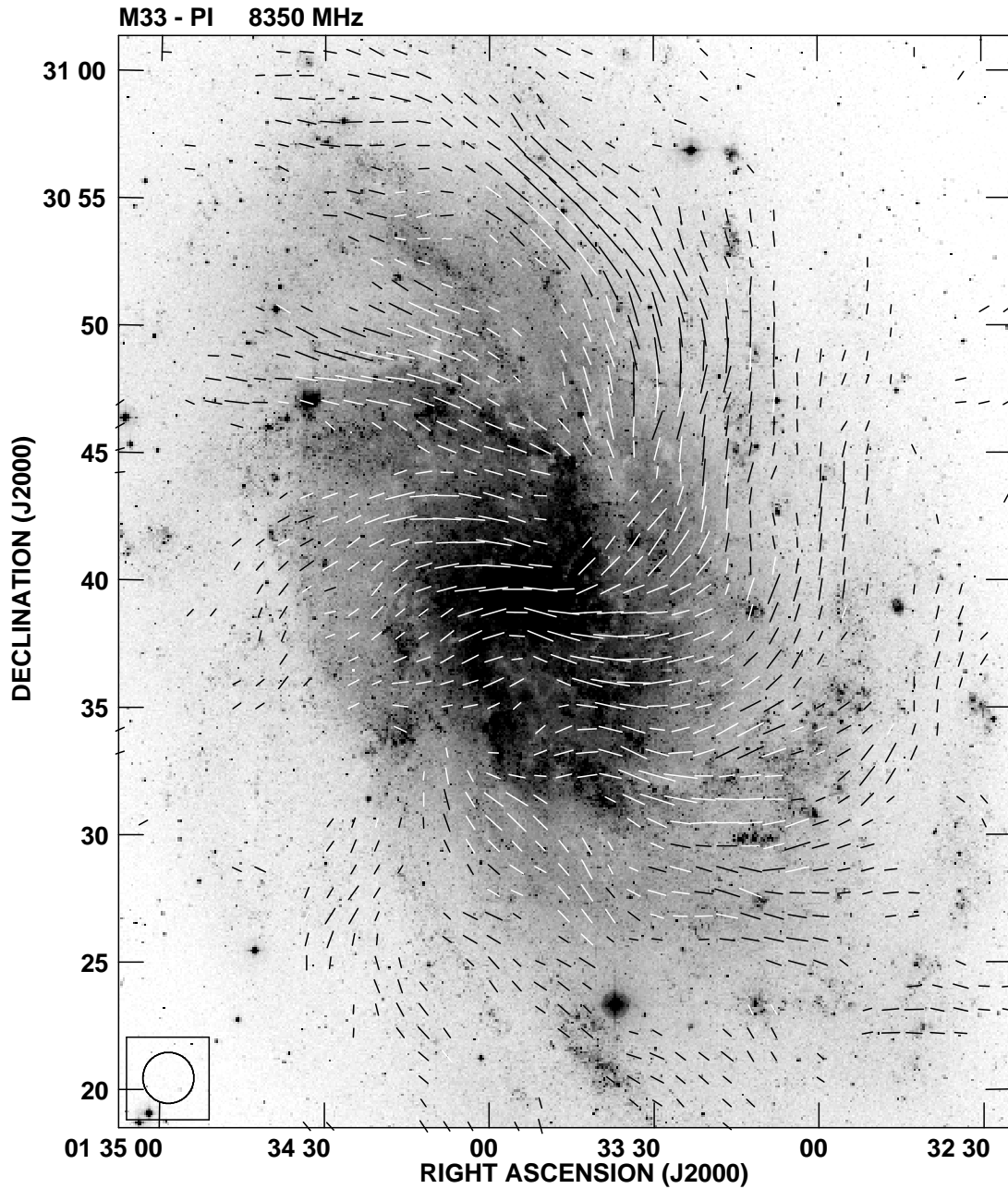


Figure 2.4: Apparent B-vectors (E-vectors rotated by 90°) at 3.6 cm superimposed on an optical image (B-band, taken from the STScI Digitized Sky Survey) of M33. A vector length of $1'$ represents a polarized intensity of 0.3 mJy/beam . The vectors were plotted starting from 1.5σ .

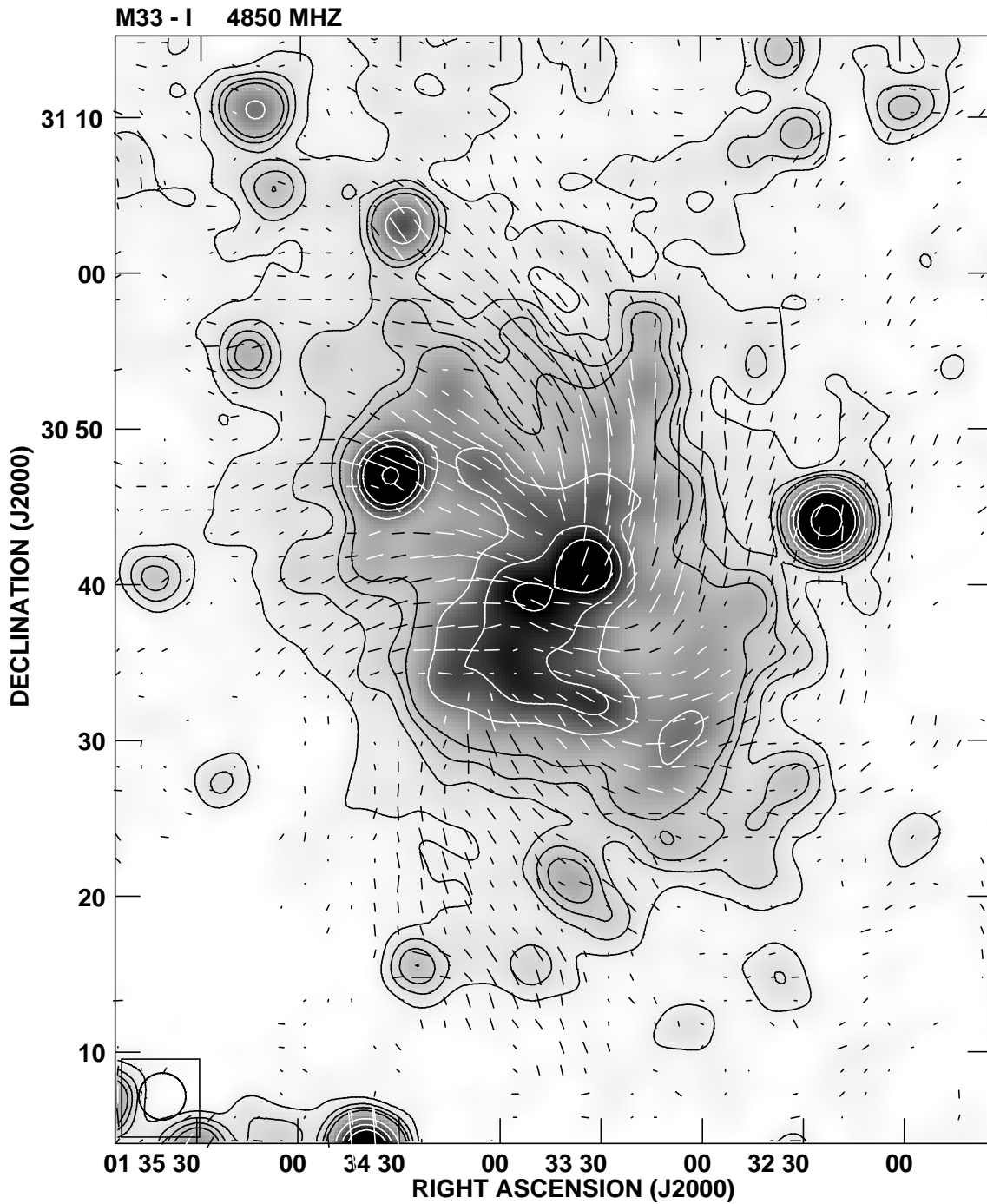


Figure 2.5: Total intensity emission from M33 at 6.2 cm observed with the Effelsberg telescope, with an angular resolution of $180''$ (the beam area is shown in the left-hand corner). Apparent B-vectors of the polarized intensity (E-vectors rotated by 90°) are superimposed. Contour levels are 2.2, 4.4, 6.6, 8.8, 17.6, 26.4, 35.2, 70.4 mJy/beam. The r.m.s. noise is 0.56 mJy/beam in total intensity and 0.12 mJy/beam in polarization. The vectors were plotted starting from 2.5σ . A vector length of $1.5'$ represents a polarized intensity of 1 mJy/beam.

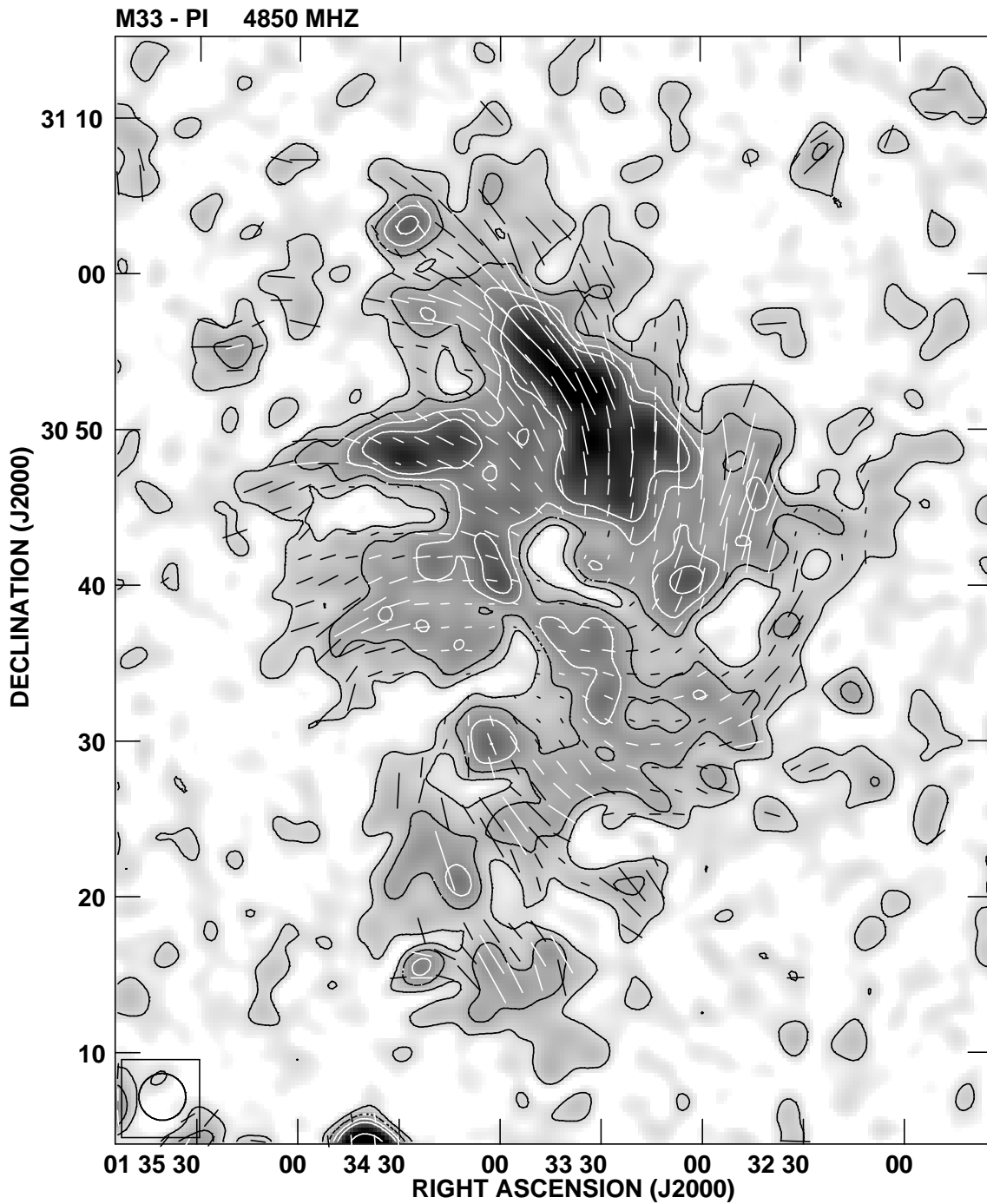


Figure 2.6: Linearly polarized emission (contours and grey scale) and degree of polarization (vector lengths) from M33 at 6.2 cm observed with the Effelsberg 100-m dish, with an angular resolution of $180''$ (the beam area is shown in the left-hand corner). Position angles of the vectors show the orientation of the magnetic field component perpendicular to the line of sight. Contour levels are 0.3, 0.6, 0.9, 1.2, 2.4 mJy/beam area. The r.m.s. noise is 0.12 mJy/beam. A vector length of $1.5'$ represents a degree of polarization of 11.7%.

Table 2.2: Central positions of the 12 fields observed with VLA at 20 cm.

Pointing #	RA (α) (^h ^m ^s)	DEC (δ) ([°] ['] ^{''})	r.m.s.(I) (μ Jy/beam)	r.m.s.(U,Q) (μ Jy/beam)	HPBW (^{''} \times ^{''})
1	01 35 01.26	+30 16 45.00	26	23	50.7 \times 49.5
2	01 33 51.79	+30 16 45.00	23	20	50.2 \times 46.1
3	01 32 42.31	+30 16 45.00	27	18	50.6 \times 43.4
4	01 35 01.26	+30 31 45.00	26	21	48.1 \times 44.0
5	01 33 51.60	+30 31 45.00	28	20	47.8 \times 45.4
6	01 32 41.96	+30 31 45.00	32	19	51.4 \times 42.2
7	01 35 01.26	+30 46 45.00	26	21	50.0 \times 46.1
8	01 33 51.41	+30 46 45.00	34	21	49.2 \times 42.4
9	01 32 41.58	+30 46 45.00	23	19	51.1 \times 44.0
10	01 35 01.26	+31 01 45.00	36	23	48.5 \times 45.2
11	01 33 51.21	+31 01 45.00	24	21	51.1 \times 43.3
12	01 32 41.21	+31 01 45.00	21	19	48.0 \times 44.0

used to reduce the data. The data from each day were calibrated separately to ensure that there were no day-to-day amplitude discrepancies. Then they were split into 12 single-source visibility data sets corresponding to the different pointings. After flagging, we combined the source visibility data from different days of the same source. We self-calibrated the combined visibility data in both phase and amplitude & phase. Final images were made with IMAGR parameter Robust=0. The r.m.s. noise of different pointings in both total intensity (I) and polarization (U and Q) are listed in Table 2.2. We convolved all the single images to the largest clean beam of 51.4'' in both RA and DEC, the individual images were reprojected on a single grid centered at RA = 01^h 33^m 51.41^s and DEC = +30° 46' 45.00''. Then, we combined the single images to a mosaic with equal weights using the task 'LTISS', which also corrects for primary beam attenuation.

There is a considerable lack of flux density in the VLA maps: the integrated total flux is only $\sim 15\%$ in total intensity and $\sim 55\%$ in polarized intensity of those in the Effelsberg maps (determined as described in Sect. 2.3.3). This is not surprising because of the missing short spacings in the forms of severe attenuation of angular scales larger than $\sim 13'$ (corresponding to the shortest spacing of ~ 40 m) and the negative bowl artifact around strong sources. To correct for the missing spacing, we combined the VLA map with the Effelsberg single-dish 20 cm map (Fletcher 2001) in the uv plane. To avoid distortions in the combined total intensity (I) map due to strong sources, we first subtracted these sources from the VLA map. The sources were identified in the Effelsberg map by comparing with the VLA map smoothed to the Effelsberg resolution. Then they were also subtracted from the Effelsberg map. The residual VLA and Effelsberg maps were combined using the task 'IMERG' with a maximum spacing of 0.236 k λ for the Effelsberg map and a minimum spacing of 0.170 k λ for the VLA map in total intensity. The corresponding maximum and minimum spacing adopted in polarization (U and Q) are 0.171 k λ and 0.150 k λ , respectively. These maximum and minimum spacing values were chosen so that the integrated flux densities of the merged maps became equal to those of the Effelsberg maps. After combination, the VLA point sources were added again. The

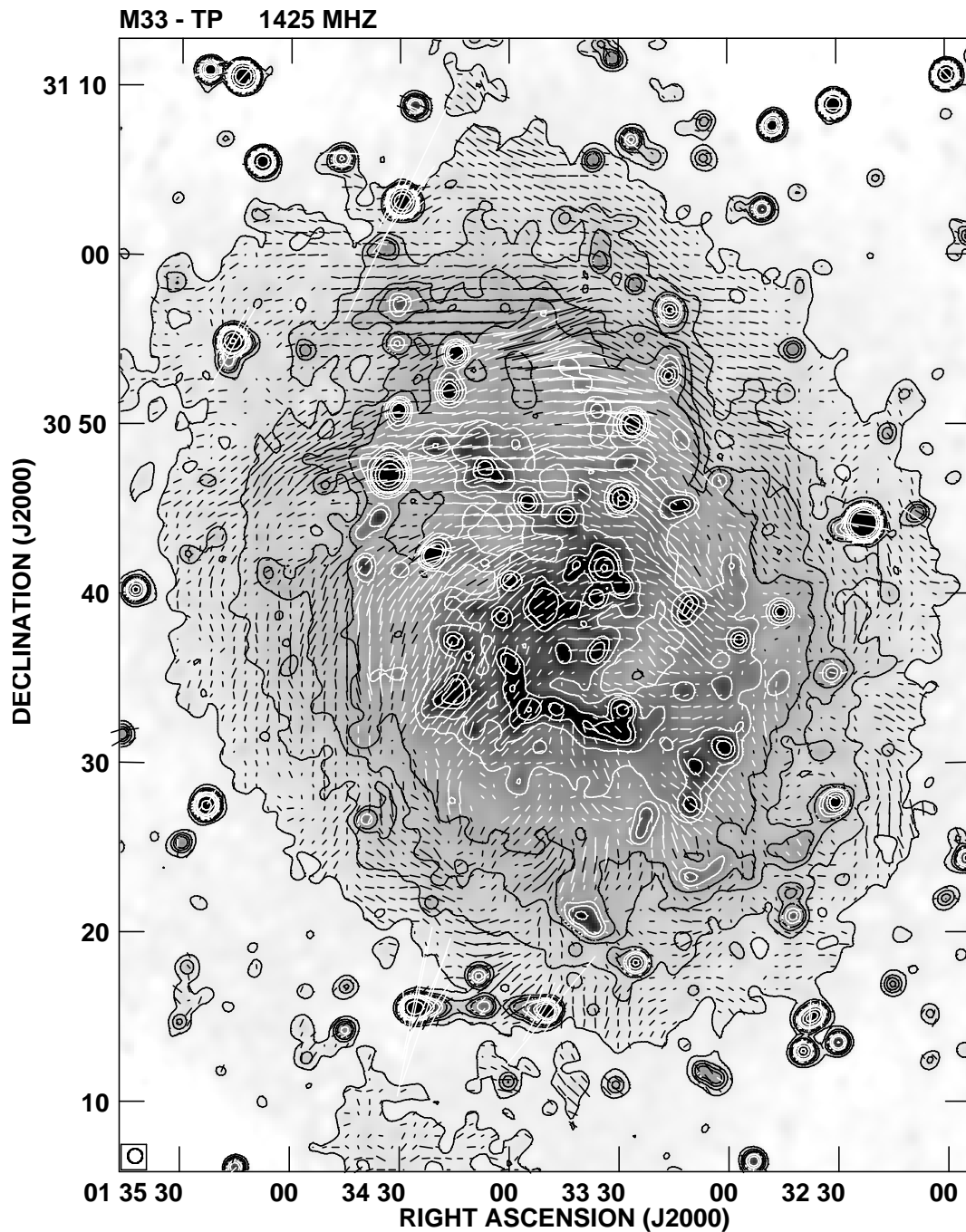


Figure 2.7: The combined VLA+Effelsberg map of the total intensity emission from M33 at 20 cm, with apparent B-vectors of polarized intensity (E-vectors rotated by 90°) superimposed. The HPBW is $51''$ (the beam area is shown in the left-hand corner). Contour levels are 0.3, 0.6, 0.9, 1.2, 1.8, 2.4, 3.6, 4.8, 9.6, 19.2 mJy/beam. The r.m.s. noise is 0.07 mJy/beam in total intensity and 0.025 mJy/beam in polarization. The vectors were plotted starting from 1.5σ . A vector length of $51''$ represents a polarized intensity of 0.1 mJy/beam.

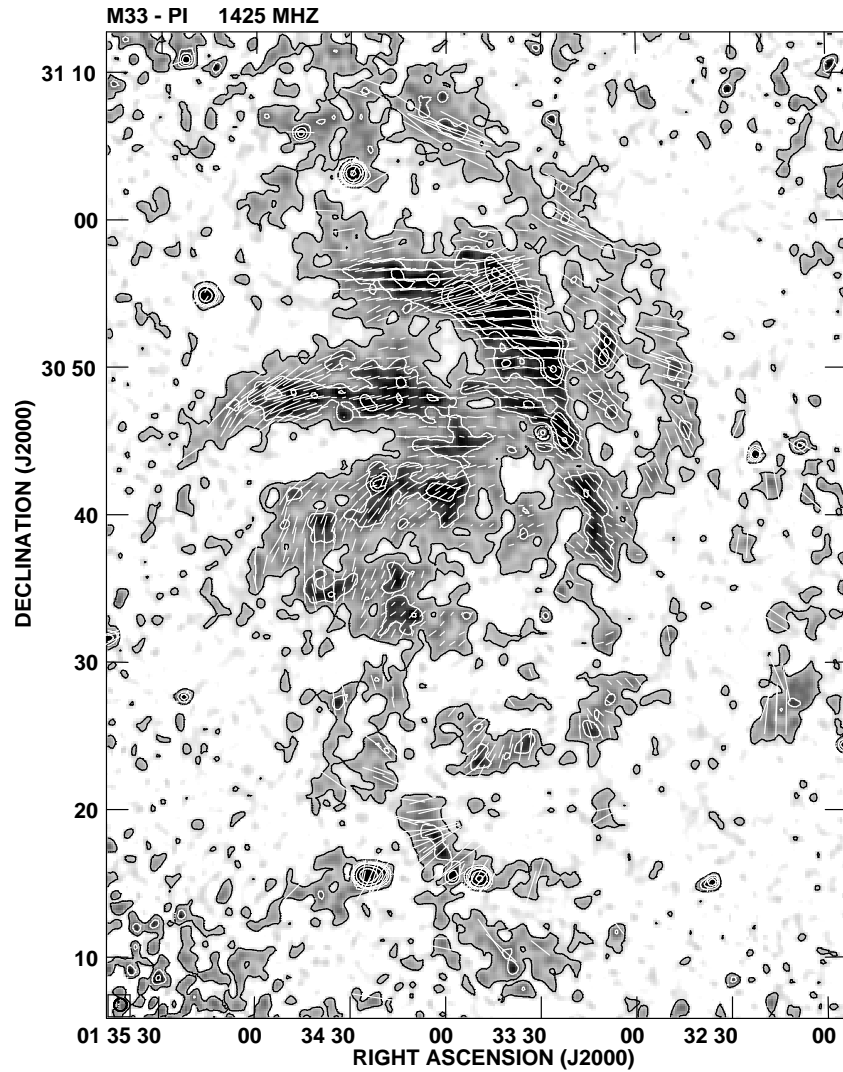


Figure 2.8: The combined VLA + Effelsberg map of the linearly polarized emission (contours and grey scale) and degree of polarization (vector lengths) from M33 at 20 cm. The HPBW is $51''$ (the beam area is shown in the left-hand corner). Contour levels are 0.07, 0.14, 0.21, 0.28, 0.42, 0.56, 0.84 mJy/beam. The r.m.s. noise is 0.015 mJy/beam. A vector length of $51''$ represents a degree of polarization of 8.7%.

Table 2.3: The 11 brightest HII regions at 3.6 cm.

Object	RA (α) ($^h m^s$)	DEC (δ) ($^\circ ' ''$)	Flux density (mJy)
NGC604	1 34 32.9	30 47 19.6	53.7 ± 0.4
NGC595	1 33 32.4	30 41 50.0	20.7 ± 0.7
IC133	1 33 15.3	30 53 19.7	9.4 ± 0.5
B690	1 34 06.5	30 47 40.0	5.3 ± 0.3
B61/62	1 33 44.8	30 44 50.0	4.9 ± 0.5
IC132	1 33 17.1	30 56 51.8	4.7 ± 0.2
IC131	1 33 12.5	30 45 21.5	4.7 ± 0.3
NGC588	1 32 44.7	30 39 20.6	4.5 ± 0.3
IC142	1 33 56.7	30 45 51.8	4.1 ± 0.2
B691	1 34 15.4	30 52 21.8	4.1 ± 0.5
NGC592	1 33 12.6	30 38 51.3	4.1 ± 0.3

r.m.s. noise in the combined maps are $\sim 70 \mu\text{Jy}/\text{beam}$ area in Stokes I and $\sim 25 \mu\text{Jy}/\text{beam}$ area in Stokes U and Q. The resulting total and polarized intensity images are shown in Figs. 2.7 and 2.8, respectively.

2.3 Results

2.3.1 Total intensity

Our total intensity map of M33 at 3.6 cm is a factor of ~ 6 more sensitive than the 2.8 cm map of Buczylowski & Beck (1987). The map at 3.6 cm with the original angular resolution of $84''$ was presented by Tabatabaei et al. (2007a). Even after smoothing to $120''$, the total intensity map (Figs. 2.1 and 2.3) shows that not only are the two main optical arms IS³ and IN pronounced, but also the northern arms IIN, IIIN, IVN, and V N are (at least partly) visible at 3.6 cm. The total intensity of the extended emission is about 4 mJy/beam in the arm IN which increases to 8 mJy/beam in parts of the arm IS. The intensity is lower than 3 mJy/beam in the other arms. The estimated peak flux densities of 11 brightest HII regions at 3.6 cm are presented in Table 2.3.

At 6.2 cm, the r.m.s. noise (0.7 mJy/beam) is improved by a factor of two with respect to the previous observations by Buczylowski & Beck (1987). The northern arms and IS plus parts of the southern arms IIS and IIIS are visible in the second contour in Fig. 2.5.

With a linear resolution of ~ 200 pc ($51.4''$) and a sensitivity of $70 \mu\text{Jy}/\text{beam}$, a large number of point sources are revealed in the total intensity map at 20 cm (Fig. 2.7). A list of the flux densities of the radio point sources at 20 cm at $7''$ resolution was presented by Gordon et al. (1999)⁴. The contour levels shown in Fig. 2.7 starts at the 4σ

³We refer to the arm notation of Humphreys & Sandage (1980); IN to VN for the northern and IS to VS for the southern arms.

⁴They observed M33 with the VLA and WSRT at 1.4 GHz and measured the flux density of point sources, but missed the extended emission.

level. The strongest extended emission is found in the arm IS with total intensities of ≥ 3.6 mJy/beam, followed by parts of the arm IN and the extended central region of the galaxy. At 20 cm, the extended emission is detected up to larger radii and is more radially symmetric than at 3.6 cm and 6.2 cm.

2.3.2 Distribution of polarized emission

The polarized emission at 3.6 cm is shown in Fig. 2.2 in grey scale and with contours. A sketch of the optical spiral arms by Sandage & Humphreys (1980) superimposed on the polarized emission is shown in Fig. 2.3. Strong polarized intensities (more than 0.4 mJy/beam) are found in between and parts of the northern optical arms IV N and IN (see Fig. 2.3) and also in central regions of the galaxy. It seems that the polarized emission, as a whole, obeys a spiral pattern structure. Whether this structure mimics the optical arm structure or not can be seen in Fig. 2.3, where a sketch of optical arms (Sandage & Humphreys 1980) is superimposed on the polarized intensity map. The polarized emission is found partly in the optical arms and partly in between the arms. In the other words, there is no clear correlation between the optical arms and polarization arm-like structure. The vectors in Fig. 2.1 (and also 2.2) show the intrinsic orientation of the ordered magnetic field in the plane of the sky ($PI \sim B_{reg\perp}^2$), as Faraday rotation is not significant at 3.6 cm. A comparison between the orientation of the ordered magnetic field and optical structure is shown in Fig. 2.4. Again, it is seen that the ordered magnetic field traces out some sort of spiral structure that does not coincide closely with the optical spiral arms, although there is a general similarity in the orientations. The strongest arm-like filament of the magnetic field exists in between the northern optical arms IV N and V N, but also covers parts of these two arms. Generally, in some regions the ordered magnetic field aligns parts of the optical arms (like parts of the arms IN and V N), is driven to the optical interarms, or locally distorted in orientation. The last is mostly seen in the southern part of the galaxy.

The vector lengths in Fig. 2.2 represent the degree of polarization, P. Apart from the northern arm IV N, P is high not only where the polarized intensity is strong: the southern optical arms IS and IIS also show high P (greater than 20%). The highest degree of polarization, $\sim 40\%$, is found near NGC604 at RA = $01^h 34^m 49.67^s$ and DEC = $+30^\circ 47' 19.49''$ (Fig. 2.3). However, it is less than 5% within the giant HII regions (e.g. NGC604 and NGC595). This, along with a weaker ordered magnetic field (and low P) in the central southern arm (IS, the strongest arm in radio, IR, and optical bands), indicates that high star-forming activity locally disturbs the regular magnetic field and causes the patchy distribution of the degree of polarization within the arms.

At the angular resolution of 180 arcsec at 6.2 cm, the magnetic arm-like filaments are smoother and not very distinguishable (Fig. 2.6). The strong polarized emission (> 1.2 mJy/beam) again occurs in parts of the arms IV N and IN, but in contrast to the 3.6 cm polarized emission, not in the central regions of the galaxy (Fig. 2.5). The high P at 6.2 cm ($> 20\%$) has almost the same distribution as at 3.6 cm. In the arm IV N, the maximum P is about 30%, similar to that at 3.6 cm.

Figure 2.7 shows, at a linear resolution of ~ 200 pc, how the apparent magnetic field vectors ($E+90^\circ$) at 20 cm are distributed in the plane of the sky. At this wavelength, the vectors are strongly Faraday-rotated and therefore not oriented along the optical arms.

Table 2.4: Integrated flux densities for $R < 8.5$ kpc.

λ (cm)	HPBW (arcsec ²)	S_T (mJy)	S_{PI} (mJy)	\bar{P} %	$S_{PI}(180'')$ (mJy)	$\bar{P}(180'')$ %
3.6	120	779 ± 66	48 ± 5	6.1 ± 0.8	40 ± 4	5.1 ± 0.7
6.2	180	1284 ± 135	89 ± 4	6.9 ± 0.8	89 ± 4	6.9 ± 0.8
20 (combined)	51	2768 ± 63	167 ± 25	6.0 ± 0.9	123 ± 3	4.4 ± 0.1

The polarized signal is strongest in the northern part of the galaxy, where the ordering in a spiral-like pattern is very clear (Fig. 2.8), while the lack of polarized emission in the southern part suggests stronger Faraday depolarization in the southern than in the northern part of M33 (see Sect. 2.3.6). In the northern arms, the degree of polarization \bar{P} is greater than 20%, with a maximum of 30% on the arm IV N and also in a region close to NGC604 in IN.

2.3.3 Integrated flux densities

After subtraction of the background sources (14 sources whose 20 cm peak flux densities were ≥ 5 mJy), we integrated the flux densities in rings in the plane of the galaxy around the center out to a radius of 8.5 kpc (beyond the area shown in Figs. 2.1 to 2.8, see Table 1.1). The integrated flux density in total intensity, S_T , and in linear polarization, S_{PI} , at different wavelengths are given in Table 2.4. The corresponding absolute total flux density errors were obtained considering the systematic error due to the baselevel uncertainty.

The average degree of polarization (\bar{P}), which is the ratio of the integrated flux density in polarized intensity and the integrated flux density in total intensity, is obtained at different wavelengths (Table 2.4). For a consistent comparison, we also obtained the average degree of polarization after smoothing the 3.6 cm and 20 cm maps to the beam width of $180''$, $\bar{P}(180'')$. At 3.6 cm and 20 cm, $\bar{P}(180'')$ is lower than \bar{P} due to beam depolarization, while $\bar{P}(180'')$ is almost the same at 3.6 cm and 6.2 cm, indicating negligible global Faraday depolarization between these two wavelengths.

The integrated total flux densities in total intensity obtained by Buczilowski (1988) of 1100 ± 167 mJy at 6.3 cm and 2990 ± 440 mJy at 20 cm out to a radius of 12 kpc agree with our values of 1300 ± 140 mJy at 6.3 cm and 3164 ± 88 mJy at 20 cm within the errors. Our obtained value at 6.2 cm is even closer to the one obtained by Berkhuijsen (1983) (1300 ± 200 mJy). The integrated total flux density in total intensity found by Buczilowski (1988) at 2.8 cm is significantly lower than what we found at 3.6 cm because the galaxy size is much larger than the maximum spacing of the 2.8 cm multibeam system (Emerson et al. 1979).

2.3.4 Distribution of total spectral index

Because of their wide frequency range, the total intensities at 20 cm and 3.6 cm lead to a reliable spectral index map. After smoothing to the angular resolution of $90''$, the total

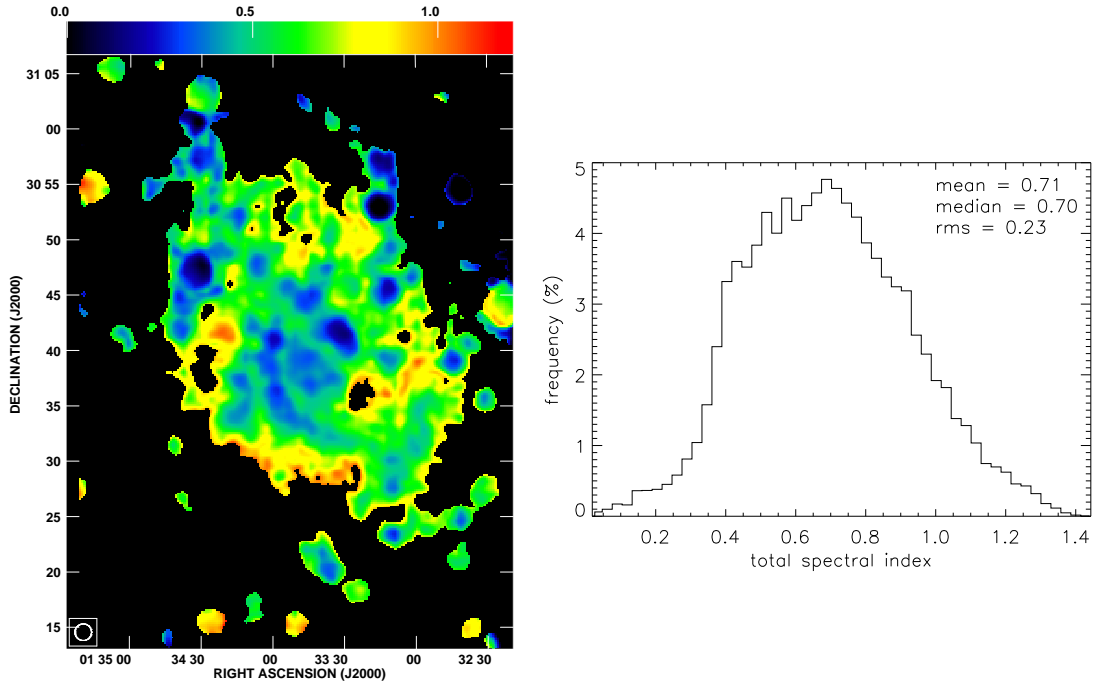


Figure 2.9: *Left*: total spectral index map of M33 as determined between the two wavelengths 3.6 and 20 cm. The angular resolution is $90''$. For the total intensity maps, 3σ level was considered to obtain this spectral index map. *Right*: histogram of the spectral index distribution determined from total intensities.

intensity maps at 20 cm and 3.6 cm were restricted to a common size and interpolated onto the same grid. The spectral index, α ($I \sim \nu^{-\alpha}$), was only computed for pixels with a flux density of at least three times the r.m.s. noise σ at both frequencies. In the resulting spectral index map (Fig. 2.9), the spiral arms and star-forming regions are very visible as flat spectrum regions. Steeper spectra occur in the outer regions and in between arms. The right panel in Fig. 2.9 shows that the total spectral index has a mean value of 0.7. The error in the total spectral index varies from 0.01 in the star-forming regions to 0.23 in the outer parts.

The HII complexes IC 133, NGC 604, and NGC 595 have spectral indices < 0.1 and even negative values, indicating optically thick conditions in these HII regions. Johnson et al. (2001) found several optically thick HII regions (at 6 cm and 20 cm) with the two brightest ones in IC 133.

The most inverted spectrum is due to a source at $RA = 01^h 32^m 42.06 \pm 0.14^s$ and $DEC = +30^\circ 54' 24.8 \pm 1.8''$, which has a spectral index of -0.6 ± 0.1 ($I_{3.6cm} = 3.6 \pm 0.2$ and $I_{20cm} = 1.24 \pm 0.07$). This source, which does not exist in the catalogues of radio sources and HII regions of M33 (e.g. in Gordon et al. 1999), could be a variable radio source or a giant optically thick HII region behind a high concentration of dust. However, the latter possibility is unlikely, since no IR emission is observed from that region.

We obtained the radial distribution of the spectral index α using the integrated total flux densities calculated in rings with a width of 0.5 kpc in the galactic plane. Figure 2.10 presents the radial profile of the spectral index obtained from pairs of the integrated flux

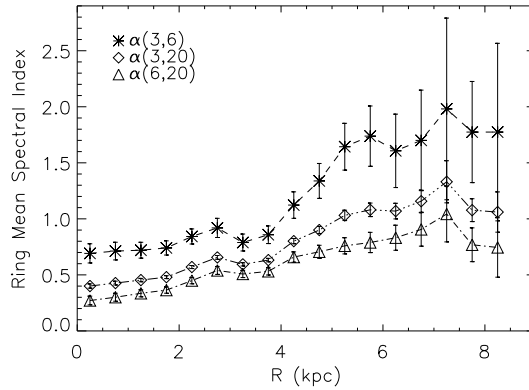


Figure 2.10: Total spectral index averaged in rings of 0.5 kpc width in the galactic plane versus the radial distance from the center of M33. For the total intensity maps, one σ level was considered before integration.

densities at 3.6 cm, 6.2 cm, and 20 cm considering one σ level. There is a general increase in α from the center to a radius of about 7 kpc in all three profiles. Buczilowski (1988) explained this increase as a general decrease in the thermal fraction with radius. However, with our high-resolution study, we detect structures not seen by Buczilowski (1988): a prominent bump around $R=3$ kpc and a steeper increase in α beyond $R=4$ kpc. This indicates that the thermal fraction decreases faster in regions at $R > 4$ kpc than at smaller radii. The bump is located in the ring $2.5 < R < 3$ kpc dominated by interarm regions that are expected to be weak in thermal emission.

Assuming that the radial increase of the spectral index is related to a decrease in the thermal fraction, and considering that the thermal emission contributes more to the radio continuum emission at shorter wavelengths, one expects more variations (or faster radial increase) of the spectral index obtained at short wavelengths. This is indeed visible in Fig. 2.10: $\alpha(3.6, 6.2)$ increases faster than $\alpha(6.2, 20)$ and $\alpha(3.6, 20)$ at $R > 4$ kpc. It is also seen that the longer the wavelengths, the smaller the spectral index (or flatter energy spectrum at longer wavelengths). This is surprising because one expects that the spectrum of the radio continuum emission becomes steeper at longer wavelengths due to the synchrotron emission. This could hint at the nonthermal energy losses at longer wavelengths. The reason may be the same as for the significant flattening of the integrated spectrum of M33 at frequencies lower than 900 MHz: free-free absorption of the nonthermal emission by a cool (< 1000 K) ionized gas (Israel et al. 1992). The presence of the optically thick HII regions (Johnson et al. 2001) could also enhance this trend.

Away from star-forming regions and in the outer parts of the galaxy, the thermal fraction is negligible and the observed spectral index α can be taken as the nonthermal spectral index, α_n . From Fig. 2.9, we obtain $\alpha_n \simeq 1.0 \pm 0.1$, which is equal to what is found in M31 by Berkhuijsen et al. (2003). Assuming that the nonthermal spectral index is constant across M33, we find average thermal fractions of 0.52 ± 0.15 , 0.46 ± 0.12 , and 0.18 ± 0.06 at 3.6 cm, 6.2 cm, and 20 cm, respectively (following the method by Klein et al. 1984). How these values change if the nonthermal spectral index is not assumed to be constant across the galaxy is discussed in Chapter 4.

Table 2.5: Integrated total flux densities from Effelsberg surveys ($R < 50'$).

λ (cm)	ν (MHz)	S (mJy)	Ref.
35.6	842	5377 ± 1217	Buczilowski (1988)
21.1	1420	2990 ± 440	Buczilowski (1988)
20 (21)	1425	2768 ± 63	Tabatabaei et al. (2007c)
17.4	1720	2714 ± 254	Buczilowski (1988)
11.1	2702	1683 ± 168	Buczilowski (1988)
6.3	4750	1100 ± 167	Buczilowski (1988)
6.2	4850	1300 ± 135	Tabatabaei et al. (2007c)
3.6	8350	779 ± 66	Tabatabaei et al. (2007c)
2.8	10700	482 ± 150	Buczilowski (1988)

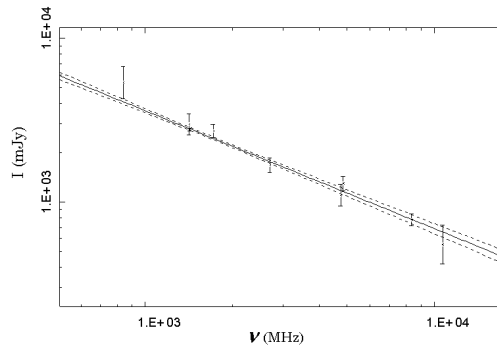


Figure 2.11: Radio spectrum of the integrated emission from M33 using the data listed in Table 2.5.

2.3.5 Integrated radio continuum spectrum

The integrated flux densities for $R < 50'$ (12 kpc) from Effelsberg surveys at 35.6, 21.1, 17.4, 11.1, 6.3, and 2.8 cm were presented by Buczilowski (1988). They obtained a spectrum with a spectral index of 0.91 ± 0.13 , steeper than found in many other spiral galaxies.

We rederived the integrated spectrum of M33 using three more data points from the new surveys. We calculated the integrated flux densities for the 3.6, 6.2, and 20 cm maps for the same area of $R < 50'$. The 3.6 cm and 2.8 cm maps were integrated up to $R = 44'$ and $R = 22.5'$, respectively, providing a lower limit to the total flux density. However, extrapolated values up to $R = 50'$ show that the missing flux densities are within errors. Our values, together with those of Buczilowski (1988) (see Table 2.5), lead to an integrated spectrum (Fig. 2.11) with a spectral index of 0.72 ± 0.04 , which agrees with the mean spectral index obtained in Sect. 2.3.4 even though using a different method.

2.3.6 Exponential scale lengths

Figure 2.12 shows the radial distributions of the total radio and IR (Spitzer 24, 70, and $160 \mu\text{m}$) intensities in M33 with galactocentric radius. There is a break in the profiles near

Table 2.6: Exponential scale lengths.

λ	$l_{R<4\text{kpc}}$ (kpc)	$l_{R>4\text{kpc}}$ (kpc)
20 cm	5.44 ± 0.27	2.74 ± 0.10
6.2 cm	3.73 ± 0.21	2.35 ± 0.14
3.6 cm	3.48 ± 0.53	1.29 ± 0.03
24 μm	2.07 ± 0.23	1.35 ± 0.09
70 μm	2.04 ± 0.19	1.85 ± 0.16
160 μm	2.51 ± 0.19	1.63 ± 0.09

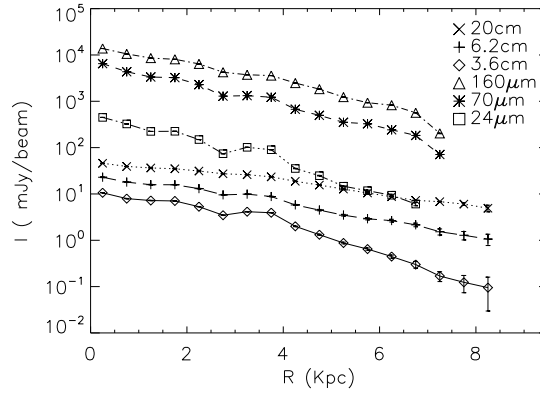


Figure 2.12: Radial profiles of total intensity (surface brightness) at radio and IR wavelengths.

Table 2.7: Northern and southern integrated flux densities in total and polarized intensity plus degree of polarization.

λ	S_T^N	S_T^S	S_T^N/S_T^S	S_{PI}^N	S_{PI}^S	S_{PI}^N/S_{PI}^S	P^N/P^S
(cm)	(mJy)	(mJy)		(mJy)	(mJy)		
3.6	412 ± 18	366 ± 21	1.12 ± 0.08	20 ± 2	20 ± 2	1.00 ± 0.14	0.9 ± 0.1
6.2	631 ± 63	653 ± 70	0.97 ± 0.14	53 ± 4	36 ± 2	1.47 ± 0.14	1.5 ± 0.2
20	1268 ± 73	1435 ± 83	0.88 ± 0.07	81 ± 5	42 ± 3	1.93 ± 0.18	2.2 ± 0.4

$R = 4$ kpc, which can be seen best at 3.6 cm and $24 \mu\text{m}$. All the profiles can be well-fitted by two exponential functions of the form

$$I(R) = \begin{cases} I_0 \exp(-R/l_{R < 4\text{kpc}}) & R < 4 \text{ kpc} \\ I_4 \exp(-R/l_{R > 4\text{kpc}}) & R \geq 4 \text{ kpc}, \end{cases} \quad (2.1)$$

where, I_0 and I_4 are the intensity at $R = 0$ and $R = 4$ kpc, respectively, and l the exponential scale length.

We derived the exponential scale lengths of the radio emission at the three wavelengths along with those of the IR emission (Table 2.6). Generally, the scale lengths are larger in regions at $R < 4$ kpc than at $R > 4$ kpc. This indicates that the surface brightness decreases faster with increasing radius at $R > 4$ kpc at all wavelengths. Since the $24 \mu\text{m}$ emission (and also 3.6 cm emission, Tabatabaei et al. 2007a) traces the star-forming regions, this confirms that the main star-forming regions in M33 are spread over an area with a radius of $R < 4$ kpc without a dominant ‘nuclear concentration’ (different from the situation in NGC6946, Walsh et al. 2002).

Table 2.6 also shows that the scale length increases with increasing wavelength in the radio regime. This can be explained by the fact that at longer wavelengths the nonthermal emission becomes more dominant, and the influence of radial diffusion of cosmic ray electrons becomes more important, leading to larger scale lengths.

2.3.7 North–south asymmetry

Figure 2.8 shows that the polarized emission at 20 cm is much weaker in the southern than in the northern half. To investigate this asymmetry, we calculated the integrated total flux density in both total and polarized intensities separately over each half (Table 2.7). The average degrees of polarization are also given in Table 2.7. At all three radio wavelengths, the beam width is $180''$. The ratio of the northern to the southern integrated total flux density in polarized intensity, S_{PI}^N/S_{PI}^S , and also the ratio of the average degree of polarization, \bar{P}^N/\bar{P}^S , increases with wavelength. The value of S_T^N/S_T^S does not change from 3.6 cm to 6.2 cm and from 6.2 cm to 20 cm within the errors, but, it decreases slightly from 3.6 cm to 20 cm. A wavelength-dependent asymmetry in the polarized intensity and average degree of polarization was also found in other galaxies e.g. NGC 6946 (Beck 2007). The interpretation is that there is an asymmetry in Faraday depolarization along the line of sight that may be caused in several ways:

- asymmetry in the distribution of the thermal emission,
- asymmetry in the uniformity of the magnetic field strength,
- special large-scale structure of the regular magnetic field, like e.g. a large-scale axisymmetric helical magnetic field (Urbanik et al. 1997).

We probe this asymmetry in Faraday depolarization effects in Chapter 5, after separation of the thermal and nonthermal components.

2.4 Discussion and conclusions

Radio observations with high resolution and sensitivity enabled us to obtain much more information about the distribution of the linearly polarized emission in M33 than in previous studies, especially at high frequencies where the Faraday effects are negligible. Using the new data at 3.6 cm, we found that the magnetic field is well-ordered in a spiral structure with the general orientation of the optical spiral arms. No clear anti-correlation between the ordered magnetic field and optical arms, as observed in other galaxies like NGC6946 (Beck et al. 1996), M81 (Krause et al. 1989a), and in parts of IC342 (Krause et al. 1989b; Krause 1993), is found in M33. Detection of high degrees of polarization (higher than 20%), not only in the northern arms but also in the central extended region and in parts of the southern arms at 3.6 cm and 6.2 cm (for the first time), is another significant result of this study. Generally, we found a patchy distribution of the degree of polarization. The degree of polarization in the direction of the HII complexes is less than 5%. We also found a weak degree of polarization and some distortion in the regular magnetic field in the central IS, which could be linked to the high star-forming activity in this region.

We derived a spectral index map of M33 with a high angular resolution ($90''$) (the previous spectral index map was derived at $462''$, Buczilowski 1988). Both the mean total spectral index (0.72 ± 0.07 , obtained from the 3.6 and 20 cm maps) and the total spectral index obtained from the integrated spectrum (0.72 ± 0.04) are consistent with the result of a statistical study of 56 spiral galaxies by Gioia et al. (1982).

The radial profile of the spectral index (Fig. 2.10) shows not only a general increase but also fluctuations at $2 < R < 4$ kpc, confirming that the decrease in the thermal fraction causes an increase in the spectral index. Considering Fig. 2.12, at $2 < R < 4$ kpc, we found opposite fluctuations in total intensity and in spectral index. These fluctuations (in Fig. 2.12) are again stronger at wavelengths at which either the thermal emission is stronger (i.e. 3.6 cm) or the emission correlates well with the thermal emission (i.e. $24 \mu\text{m}$, see Tabatabaei et al. 2007a). The area at $2 < R < 3$ kpc includes the region between the main arm I (IN, IS) and the central extended region of the galaxy, corresponding to the small maximum (bump) in the spectral index profile and a small minimum in the total intensity profile. The area at $3 < R < 4$ kpc includes the arm IN and NGC604, corresponding to the small minimum in Fig. 2.10 and the small maximum in Fig. 2.12.

Like the star formation radial profile ($24 \mu\text{m}$ radial profile, see Sect. 2.3.6), the mostly nonthermal 20 cm radial profile is fitted by a larger exponential scale length at $R < 4$ kpc than at $R > 4$ kpc. This is a surprising result, indicating that even the nonthermal emission (which is less confined to the star-forming regions than the thermal emission) mimics the distribution of its parents, the star-forming regions. A spatial coupling between the nonthermal emission and star-forming regions was also found in other late-type galaxies (Dumke et al. 2000; Chyży et al. 2007). Therefore, it would be highly interesting to derive the distribution of the nonthermal emission for a more realistic non-constant spectral index of the nonthermal emission (Chapter 4).

3 Multi-scale study of radio and IR emission from M33

3.1 Introduction

One of the most important discoveries of the IRAS mission was the correlation between the IR and radio continuum luminosities for a sample of galaxies (e.g., Helou et al. 1985; de Jong et al. 1985; Gavazzi et al. 1986). Beck & Golla (1988) showed that this correlation also holds within several spiral galaxies including M31 and M33. The radio–IR correlation was interpreted by Helou et al. (1985) and de Jong et al. (1985) as a direct and linear relationship between star formation and IR emission. On the other hand, there was concern that the cold dust emission, as a component of the far–infrared (FIR) emission, might not be directly linked to the young stellar population. For the nearby galaxy M31, Hoernes et al. (1998), using IRAS data, found a good correlation between the emission of thermal–radio/warm dust and nonthermal–radio/cold dust with slightly different slopes. They explained the latter correlation by a coupling of the magnetic field to the gas mixed with the cold dust. Such a coupling was also considered by Niklas & Beck (1997) as the origin of the global radio–FIR correlation. Hinz et al. (2004) found similar behavior in M33.

The possibility that the relationship between the radio and IR emission might vary within galaxies (e.g., Gordon et al. 2004b) due to the range of individual conditions makes it necessary to repeat these kinds of studies with improved data in the most nearby galaxies. Furthermore, it is uncertain what component of a galaxy provides the energy that is absorbed and re–radiated in the IR (Kennicutt 1998). For example, from the close correspondence between hydrogen recombination line emission and IR morphologies, Devereux et al. (1994); Devereux et al. (1996, 1997) and Jones et al. (2002) argued that the FIR is powered predominantly by young O/B stars. Deul (1989), Walterbos & Greenawalt (1996), and Hirashita et al. (2003) argued that about half of the IR emission or more is due to dust heated by a diffuse interstellar radiation field that is not dominated by any particular type of star or star cluster. Sauvage & Thuan (1992) suggested that the relative role of young stars compared with the diffuse interstellar radiation field increases with later galaxy type.

Another problem that hinders a better understanding of the radio–IR correlation is the separation of thermal and nonthermal components of the radio continuum emission using a constant nonthermal spectral index (the standard method). Although this assumption leads to a proper estimation for global studies, it cannot produce a realistic image of the nonthermal distribution in highly resolved and local studies within a galaxy, because it

is unlikely that the nonthermal spectral index remains constant across a galaxy (Fletcher et al. 2004).

M33 (NGC 598) is the nearest late-type spiral galaxy, at a distance of 840 kpc (Freedman et al. 1991) and is ideal to compare the morphologies of different components of such a galaxy. With an inclination of $i = 56^\circ$ (Regan & Vogel 1994), it is seen nearly face on. The central position of M33 given by de Vaucouleurs & Leach (1981) is RA(2000) = $1^{\text{h}}33^{\text{m}}51.0^{\text{s}}$ and DEC(2000) = $30^\circ 39' 37.0''$. The position angle of the major axis is $\text{PA} \sim 23^\circ$ (Deul & van der Hulst 1987).

With the Multiband Imaging Photometer Spitzer (MIPS, Rieke et al. 2004) data at 24, 70, and 160 μm , it is possible to interpret the morphology of M33. Hinz et al. (2004) compared the first epoch data of MIPS with $\text{H}\alpha$ images and radio continuum data at 6 cm, using a Fourier filtering technique to distinguish different emission components. We now have multiple epochs of MIPS data that provide a significantly higher-quality image of M33, for example in the suppressing of stripes along the direction of scan caused by slow response from the far infrared arrays. In addition, we use a wavelet analysis technique that Frick et al. (2001) have shown to be more robust against noise than Fourier filtering. Furthermore, the wavelet technique provides more precise and easier analysis of the scale distribution of emission energy, especially at smaller scales of the emitting structures. We apply a 2D-wavelet transformation to separate the diffuse emission components from compact sources in MIPS mid- and far-infrared (hereafter IR), radio (at 3.6 and 20 cm), and $\text{H}\alpha$ images (Table 3.1).

The classical correlation between IR and radio emission has been at the whole galaxy level. However, such a correlation can be misleading when a bright, extended central region or an extended disk exists in the galactic image. This technique gives little information in the case of an anticorrelation on a specific scale (Frick et al. 2001). The ‘wavelet cross-correlation’ introduced by Frick et al. (2001) calculates the correlation coefficient as a function of the scale of the emitting regions. Hughes et al. (2006) applied this method to study the radio-FIR correlation in the Large Magellanic Cloud (LMC).

Hippelein et al. (2003) found evidence for a local radio-FIR correlation in the star forming regions of M33. In this paper, we investigate this correlation not only for the star forming regions but also for other structures within M33 at spatial scales between 0.4 and 4 kpc using the wavelet cross-correlation. Instead of the standard method to separate the thermal and nonthermal components of the radio continuum emission, we use the radio continuum data both at high and low frequency (3.6 and 20 cm, respectively). We compare our radio images to the $\text{H}\alpha$ image (which is taken as a tracer of the thermal free-free emission) to distinguish the components of the radio continuum emission.

We study the structural characteristics of the MIPS IR images using the 2D-wavelet transformation in Sect. 3.3. The distribution of the emission energy at both IR and radio regimes and the dominant spatial scale at each wavelength are discussed in Sect. 3.4. We show how the different MIPS images are correlated at different scales and how the radio-IR correlation varies with components of the galaxy (e.g. gas clouds, spiral arms, extended central region and extended diffuse emission) in Sect. 3.5. In Sect. 3.6, we use the $\text{H}\alpha$ map to probe the energy sources of IR and radio emission. Results and discussion are presented in Sect. 3.7. An overview of the preliminary results was presented in Tabatabaei et al. (2005).

Table 3.1: M33 data used in radio-IR correlation study.

Wavelength	Resolution (arcsec)	Telescope	Ref.
20 cm	51	VLA	Tabatabaei et al. (2007c)
20 cm	540	Effelsberg	Fletcher (2001)
3.6 cm	84	Effelsberg	Tabatabaei et al. (2007c)
160 μm	40	Spitzer	Tabatabaei et al. (2007a)
70 μm	18	Spitzer	Tabatabaei et al. (2007a)
24 μm	6	Spitzer	Tabatabaei et al. (2007a)
6570Å ($\text{H}\alpha$)	2 (pixel size)	KPNO	Hoopes & Walterbos (2000)

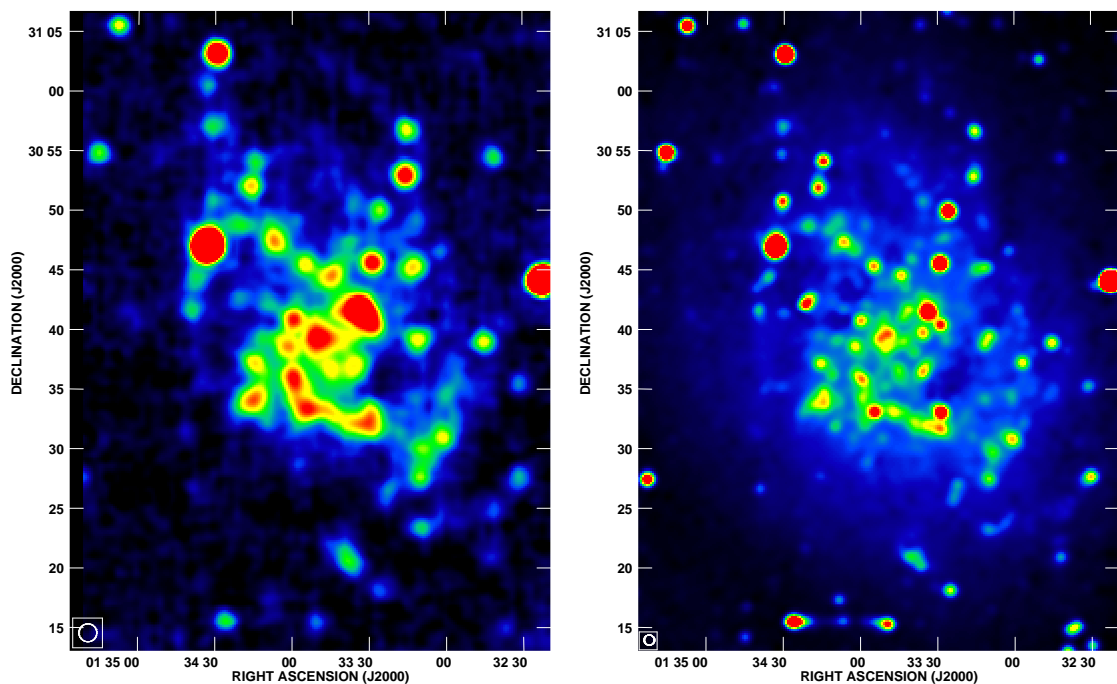


Figure 3.1: The 3.6 cm radio map of M33 (left panel) observed with the 100-m radio telescope in Effelsberg, and the combined 20 cm radio map (right panel) from the VLA and Effelsberg observations. The half power beam widths (HPBWs) of 84'' and 51'', respectively, are shown in the lower left corners.

3.2 Observations and data reduction

Table 3.1 summarizes the data used in this work. The 3.6 cm radio observations were made with the 100-m Effelsberg telescope¹ during several periods (18 nights) between August 2005 and March 2006. The reduction was done in the NOD2 data reduction system (Haslam 1974). The r.m.s. noise after combination (Emerson & Graeve 1988)

¹The 100-m telescope at Effelsberg is operated by the Max-Planck-Institut für Radioastronomie (MPIfR) on behalf of the Max-Planck-Gesellschaft.

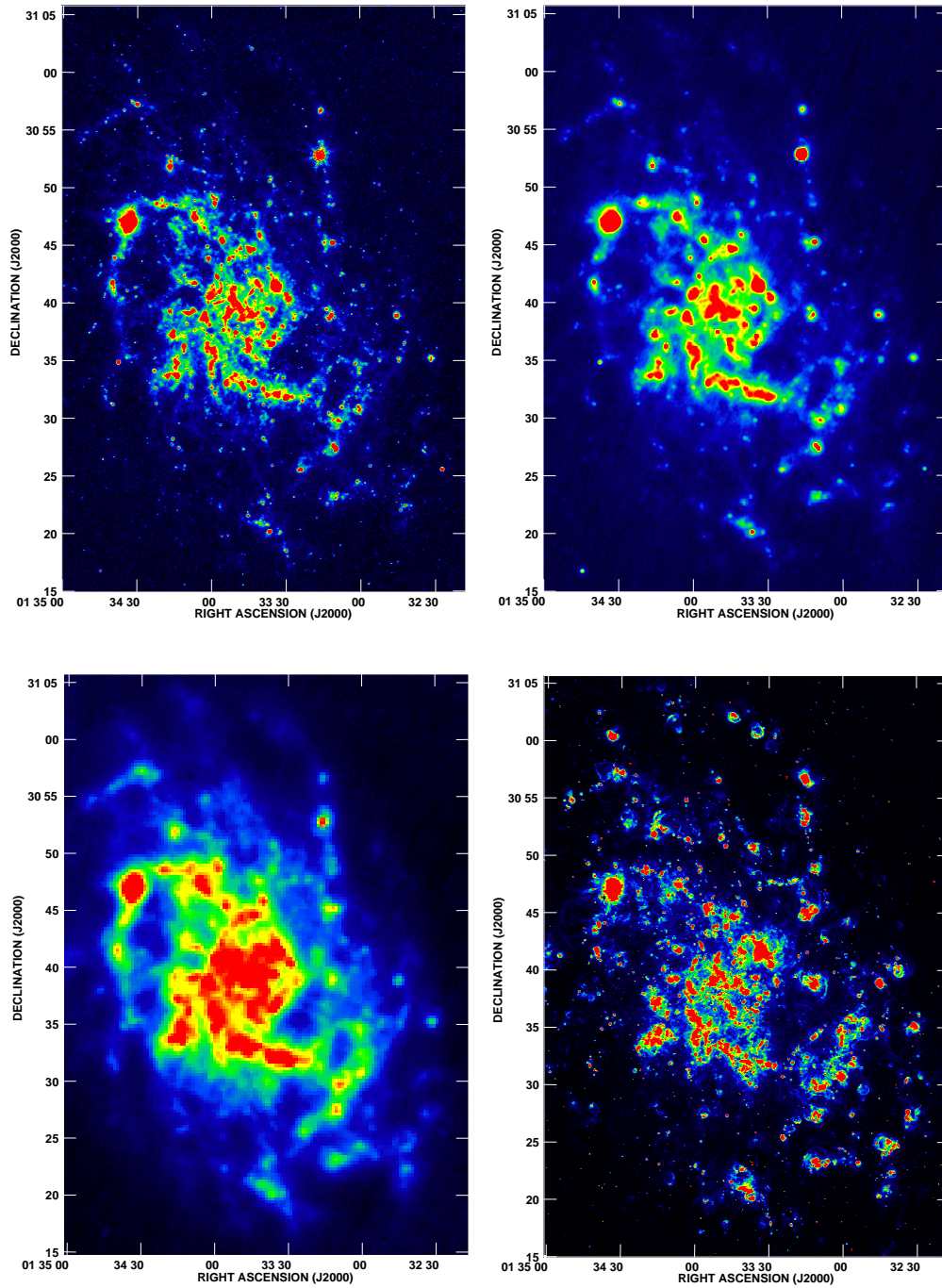


Figure 3.2: *Top*: the Spitzer MIPS images of M33 at 24 μm (left panel) and 70 μm (right panel). *Bottom*: the Spitzer MIPS image at 160 μm (left panel) and the H α map (right panel) from KPNO Hoopes & Walterbos (2000). The resolutions are given in Table 3.1.

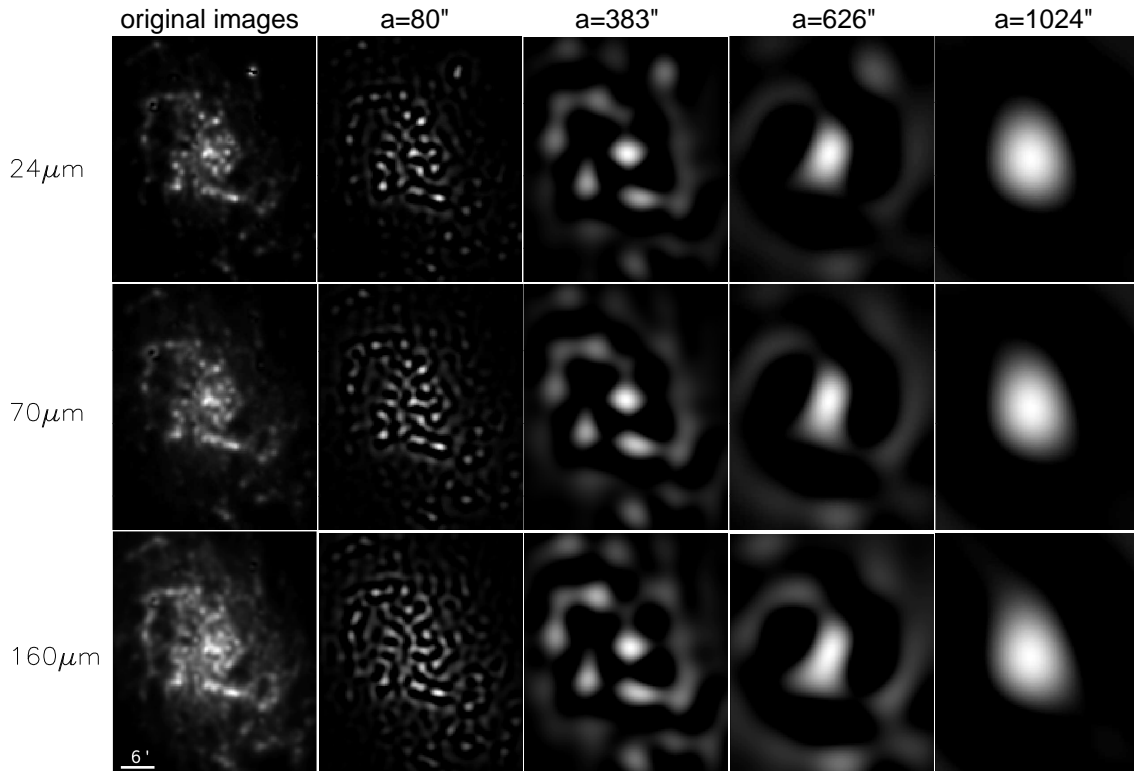


Figure 3.3: MIPS maps of M33 at $40''$ resolution (first column) and their wavelet decompositions for 4 different scales: $80''$ (second column), $383''$ (third column), $626''$ (fourth column), and $1024''$ (fifth column). At the distance of 840 kpc, $1''$ is equivalent to 4 pc. The maps at 24, 70, and $160 \mu\text{m}$ are shown from top to bottom. Before the decomposition, huge HII regions like NGC 604 were subtracted from the original images (Sect. 3.4). Maps are shown in RA–DEC coordinate system and centered at the center of the galaxy. The field size is $34' \times 41'$.

of 36 coverages is $\sim 220 \mu\text{Jy}/\text{beam}$. We also observed M33 at 20 cm with the B–band VLA² D-array during 5 nights in November 2005 and January 2006 (from 06 to 08-11-05, 13-11-05, and 06-01-06). The reduction, calibration, and mozaicing of 12 fields were accomplished using the standard AIPS programs. The VLA interferometric data will miss much of the extended emission of the galaxy. For example, Viallefond et al. (1986b) showed that the WSRT interferometric map at 1.4 GHz accounted for only about 16% of the total emission. Therefore, we combined the VLA map with the new Effelsberg 20 cm map (Fletcher 2001) to recover the emission from extended structures in M33 (see Chapter 2). Both radio maps are shown in Fig. 3.1 at their original resolutions.

M33 was mapped in the IR by MIPS (Rieke et al. 2004) four times on 29/30 December 2003, 3 February 2005, 5 September 2005, and 9/10 January 2006. Each observation consisted of medium-rate scan maps with $1/2$ array cross-scan offsets and covering the full extent of M33. The basic data reduction was performed using the MIPS instrument team Data Analysis Tool versions 3.02-3.04 (Gordon et al. 2005). At $24 \mu\text{m}$ extra steps

²The VLA is a facility of the National Radio Astronomy Observatory. The NRAO is operated by Associated Universities, Inc., under contract with the National Science Foundation.

were carried out to improve the images including readout offset correction, array averaged background subtraction (using a low order polynomial fit to each leg, with the region including M33 excluded from this fit), and exclusion of the first five images in each scan leg due to boost frame transients. At 70 and 160 μm , the extra processing step was a pixel dependent background subtraction for each map (using a low order polynomial fit, with the region including M33 excluded from this fit). The background subtraction should not have removed real M33 emission as the scan legs are nearly parallel to the minor axis resulting in the background regions being far above and below M33.

The 24 μm image used consisted of just the 9/10 January 2006 observations as the depth reached in a single mapping was sufficient for this work. The 70 μm image used was a combination of the last three observations as the 29/30 December 2003 70 μm map suffered from significant instrumental residuals. These instrumental residuals were much reduced when the operating parameters of the 70 μm array were changed after the first M33 map was made and before the second. The 160 μm image used consisted of a combination of all four maps. The combination of multiple maps of M33 taken with different scan mirror angles results in a significant suppression of residual instrumental signatures (seen mainly as low level streaking along the scan mirror direction). The images used in this work have exposure times of ~ 100 , 120, and 36 seconds/pixel for 24, 70, and 160 μm , respectively.

The $\text{H}\alpha$ observations by Hoopes & Walterbos (2000) were carried out on the 0.6 meter Burrell–Schmidt telescope at the Kitt Peak National Observatory, providing a $68' \times 68'$ field of view. The MIPS and $\text{H}\alpha$ images are shown in Fig. 3.2.

To obtain a proper comparison with the 3.6 cm radio map, all images of M33 were convolved to the angular resolution of $84''$. For higher angular resolution studies, maps at $18''$, $40''$, and $51''$ were also made. The PSF (point spread function) of the MIPS data is not Gaussian, in contrast to that of the radio data. Thus, convolutions of the MIPS images were made using custom kernels created using Fast Fourier Transforms (FFTs) to account for the detailed structure of the MIPS PSFs. Details of the kernel creation can be found in Gordon et al. (2007, in prep.). After convolution, the maps were normalized in grid size, rotation and reference coordinates. Then, they were cut to a common field of view ($34' \times 41'$ in RA and DEC, respectively).

In the following sections, we discuss the results with and without bright compact sources at each resolution to investigate how these sources affect the energy distribution at each wavelength and the correlations between wavelengths. After convolving to each resolution, the bright sources, common to all images, were subtracted using Gaussian fits including baselevels ('Ozmapax' program in the NOD2 data reduction system). For instance, the giant HII complexes NGC604 and NGC595 were subtracted at all resolutions. We also subtracted strong steep-spectrum background radio sources from the 20 cm image. Detailed descriptions of the source subtraction at each resolution are given in Sect. 3.4.

3.3 Wavelet analysis of IR emission

Wavelet analysis is based on a spatial-scale decomposition using the convolution of the data with a family of self-similar basic functions that depend on the scale and location

Table 3.2: Source subtraction thresholds $S(\lambda)$ and number of subtracted sources at different spatial resolutions.

HPBW asec	Subt. sources #	$S_{24\mu\text{m}}$ $\mu\text{Jy/asec}^2$	$S_{70\mu\text{m}}$ $\mu\text{Jy/asec}^2$	$S_{160\mu\text{m}}$ $\mu\text{Jy/asec}^2$	$S_{20\text{cm}}$ $\mu\text{Jy/b.a.}$	$S_{3.6\text{cm}}$ $\mu\text{Jy/b.a.}$
18	40	460	2650	–	–	–
51	15	115	1570	2865	7190	–
84	11	85	900	2340	8260	5780

of the structure. Like the Fourier transformation, the wavelet transformation includes oscillatory functions; however, in the latter case these functions rapidly decay towards infinity. As a result, Frick et al. (2001) show that the wavelet method is more resistant to noise and the smoother spectra allow better determination of the true frequency structure. The cross-correlation of wavelet spectra lets us compare the structures of different images systematically as a function of scale.

The wavelet coefficients of a 2D continuous wavelet transform are given by:

$$W(a, \mathbf{x}) = \frac{1}{a^\kappa} \int_{-\infty}^{+\infty} f(\mathbf{x}') \psi^* \left(\frac{\mathbf{x}' - \mathbf{x}}{a} \right) d\mathbf{x}', \quad (3.1)$$

where $\psi(\mathbf{x})$ is the analysing wavelet, $\mathbf{x} = (x, y)$, $f(\mathbf{x})$ is a two-dimensional function (an image), and a and κ are the scale and normalization parameters, respectively, (the * symbol denotes the complex conjugate). The above transformation decomposes an image into ‘maps’ of different scale. In each map, structures with the chosen scale are prominent as they have larger coefficients than those with smaller or larger scales. To obtain a good separation of scales and to find the scale of dominant structures in M33, we use the ‘Pet–Hat’ wavelet that was introduced by Frick et al. (2001) and applied there to NGC 6946. It is defined in Fourier space by the formula:

$$\psi(\mathbf{k}) = \begin{cases} \cos^2 \left(\frac{\pi}{2} \log_2 \frac{k}{2\pi} \right) & \pi \leq \mathbf{k} \leq 4\pi \\ 0 & \pi > \mathbf{k} \text{ or } \mathbf{k} > 4\pi, \end{cases} \quad (3.2)$$

where \mathbf{k} is the wavevector and $k = |\mathbf{k}|$.

We decomposed the Spitzer images into 10 different scales a to compare the morphologies at 24, 70, and 160 μm at each scale³. Fig. 3.3 shows the original maps and the decomposed maps at 4 scales. The original 24 and 70 μm maps were smoothed to the MIPS 160 μm PSF with FWHM (full width half maximum) = 40'' before decomposition. The maps at scale $a = 80''$ (0.3 kpc) show the smallest detectable emitting structures. Most of the morphological differences among the MIPS images are found at this scale. At scale $a = 383''$ (1.5 kpc), the prominent structures are spiral arms and the center of the galaxy. The central extended region is more pronounced at scale $a = 628''$ (2.5 kpc). The emission emerges from a diffuse structure at scale $a = 1024''$ (4 kpc), and it is not possible to distinguish the arm–structure anymore. This structure can be identified as an underlying diffuse disk with a general radial decrease in intensity. The similarity of the 4 kpc

³To have both physically meaningful results and a sufficiently large number of independent points, the scale a varies between a minimum of about twice the resolution and a maximum of about half of the image size, $a < 1100''$, for all images studied in this paper.

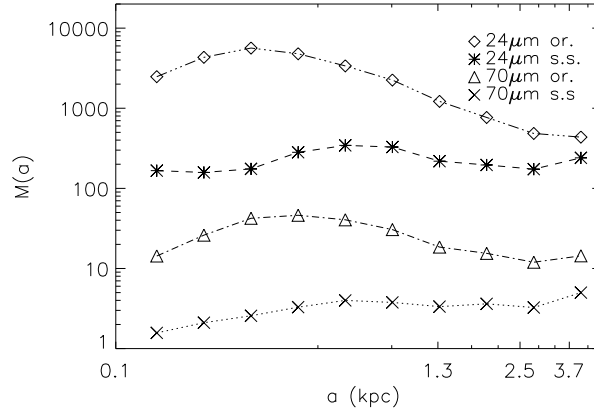


Figure 3.4: The wavelet spectra of the 24 and 70 μm images before (or.) and after (s.s.) subtraction of the same sources from the two images at $18''$ resolution. The data points correspond to the scales 0.14, 0.20, 0.29, 0.45, 0.62, 0.90, 1.32, 1.92, 2.79, 4.06 kpc. The spectra are shown in arbitrary units.

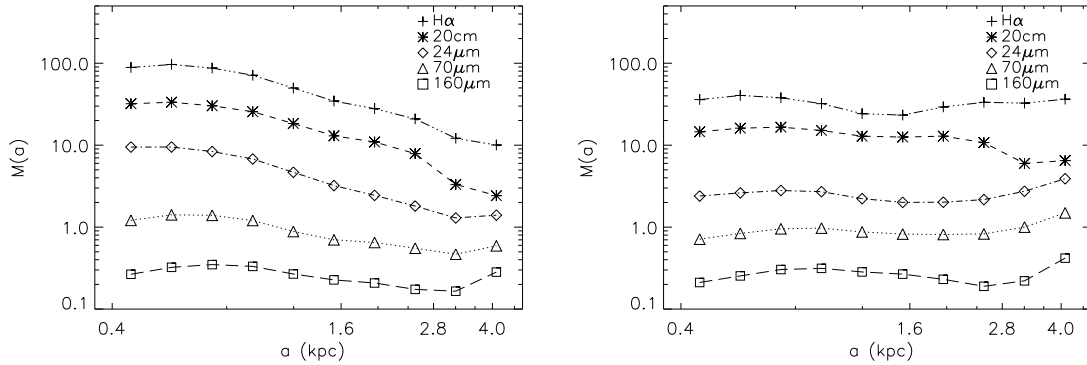


Figure 3.5: The wavelet spectra of the 20 cm radio and IR images at $51''$ resolution before (left) and after (right) subtraction of the same sources. For comparison, the wavelet spectrum of the $\text{H}\alpha$ emission is also plotted. The data points correspond to the scales 0.45, 0.57, 0.73, 0.94, 1.20, 1.53, 1.96, 2.50, 3.20, 4.09 kpc. The spectra are shown in arbitrary units.

maps at different wavelengths indicates that the large-scale diffuse emission has the same structure at different mid- and far-infrared wavelengths.

At the smallest scale, the emission emerges from spot-like features aligned along filaments with the width of the scale. At $24\ \mu\text{m}$ the spots corresponding to HII regions contain most of the energy at this scale (see Sect. 3.6). Diffuse filaments are more pronounced at $160\ \mu\text{m}$. As shown in the next section, the fraction of the energy at this scale at $160\ \mu\text{m}$ is less than that at $24\ \mu\text{m}$. The situation in the $70\ \mu\text{m}$ map is in between the 24 and $160\ \mu\text{m}$ maps. It seems that the star forming regions provide most of the energy of the 24 and $70\ \mu\text{m}$ emission, if the spots correspond to these regions, as is discussed in the following sections.

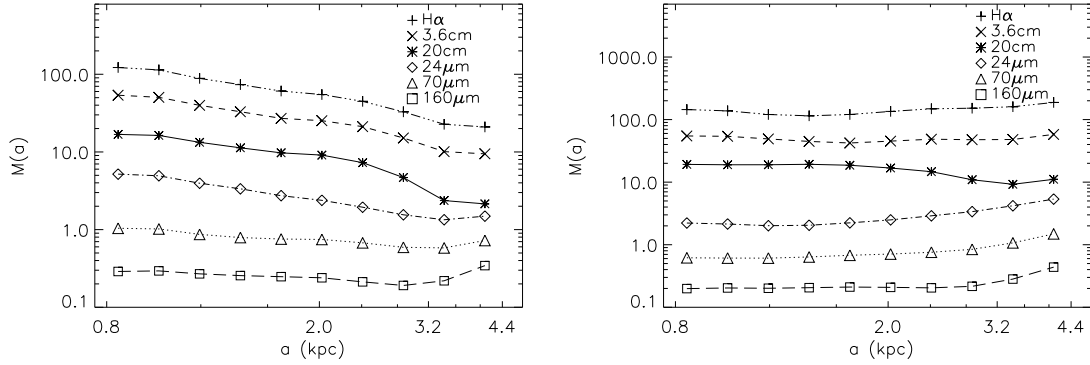


Figure 3.6: The wavelet spectra of the 3.6 cm radio and IR images at $84''$ resolution before (left) and after (right) subtraction of the same sources. For comparison, the spectrum of the $H\alpha$ emission is also plotted. The data points correspond to the scales 0.84, 1.00, 1.19, 1.42, 1.67, 2.02, 2.41, 2.87, 3.42, 4.08 kpc. The spectra are shown in arbitrary units.

3.4 Spectral characteristics of IR and radio maps

In this section, we demonstrate how the wavelet spectra can be used to investigate the scaling properties of the emission. This spectrum is defined as the energy in the wavelet coefficients of scale a (Frick et al. 2001)⁴:

$$M(a) = \int_{-\infty}^{+\infty} \int_{-\infty}^{+\infty} |W(a, \mathbf{x})|^2 d\mathbf{x}. \quad (3.3)$$

After smoothing the $24 \mu\text{m}$ map to the MIPS $70 \mu\text{m}$ PSF with $\text{FWHM} = 18''$, about 40 bright sources (mostly corresponding to HII regions) were subtracted from both maps (equivalent to removing sources with fluxes higher than the lower limits, $S(\lambda)$, given in Table 3.2.). Fig. 3.4 shows the wavelet spectra, $M(a)$, of the $24 \mu\text{m}$ and $70 \mu\text{m}$ maps before and after source subtraction. Clearly, the small scales are the dominant scales before source subtraction. The scale at which the wavelet energy is maximum is $\sim 70''$ (280 pc) at $24 \mu\text{m}$ and $\sim 110''$ (440 pc) at $70 \mu\text{m}$. After source subtraction, the spectra become flatter. The larger size of the dominant scale at $70 \mu\text{m}$ caused by these sources (by a factor of ~ 1.6 at this resolution) indicates a slightly more extended distribution of dust grains emitting at $70 \mu\text{m}$ than at $24 \mu\text{m}$ in the vicinity of star forming regions. Moreover, the ratio of the maximum to minimum energy in the original spectrum at $24 \mu\text{m}$ is larger (by a factor of 3) than that at $70 \mu\text{m}$. This indicates that either star forming regions provide more energy for the $24 \mu\text{m}$ emission, or the large-scale diffuse emission is stronger at $70 \mu\text{m}$ than $24 \mu\text{m}$.

At the next angular resolution, $51''$, the HPBW (half power beam width) of the 20 cm radio map, 15 bright sources (HII regions) visible at all maps were subtracted from the 20 cm map and the smoothed 24, 70, and $160 \mu\text{m}$ IR maps. In addition to these sources, 9 background radio sources plus the supernova remnants SN1, SN2, and SN3 (Viallefond

⁴It is also called ‘wavelet power spectrum’, however following some authors (e.g. Frick et al. 2001; Zhou & Adeli 2003), we refer to $M(a)$ as the ‘wavelet energy’ (see Appendix B).

et al. 1986a) were subtracted from the 20 cm radio map. The wavelet spectra of the MIPS and 20 cm radio maps at this resolution are plotted in Fig. 3.5. The $H\alpha$ spectrum is also given for comparison. The 24 and 70 μm maps show a smoothed version of their distributions in Fig. 3.4 (the linear smoothing factor is ~ 3 between Figs. 3.4 and 3.5). However, the effect of the sources can still be seen by comparing the left panel with the source subtracted spectra in the right panel.

The 160 μm map is hardly influenced by the smoothing, as its original resolution is 40'' (the smoothing factor is ~ 1.3). The 160 μm spectrum is more similar to the 70 μm spectrum than to the other spectra. It seems that the compact sources have less effect on the energy distribution at 160 μm , because the smallest scale is not the dominant scale. Hence, there is no important change in the spectrum after the source subtraction. The energy shows an increase at the scale of complexes of dust and gas clouds ($\sim 250''$ or 1 kpc), then a second increase in transition to the large-scale structures or diffuse dust emission.

The spectrum of the 20 cm radio image is also dominated by bright sources. There is a maximum at the scale $a = 140''$ (560 pc), then a decrease towards the larger scales with a slope of -0.9. However, a flat spectrum remains for the scales less than the size of the central extended region ($\sim 600''$ or 2.4 kpc) after the source subtraction.

The spectra of all the maps at the resolution of the 3.6 cm data (HPBW = 84'')⁵ are shown in Fig. 3.6 (left panel). The spectra after subtracting the 11 brightest HII regions are plotted in the right panel. Again, because of these sources, the small scales are dominant at 3.6 cm. As shown in comparing the left and right panels, they also are seen in all the infrared bands, strongly at 24 μm and much more weakly at 160 μm . Here, the smoothing effect is seen in all 3 MIPS wavelet spectra.

Before source subtraction, the 20 and 3.6 cm spectra are similar to each other and to the $H\alpha$ spectrum up to the scale of the central extended region, $\sim 600''$ (2.4 kpc). All three spectra become steeper between $a \sim 2.4$ kpc and $a \sim 3.4$ kpc, which means that the wavelet energy from structures with scales of about half of the size of the galaxy ($\sim 900''$ or 3.6 kpc) is not as significant as that from smaller structures. It seems that a minimum in the wavelet spectra of the radio and $H\alpha$ emission, as was also shown in NGC 6946 (see Fig. 3.7 in Frick et al. 2001), is a characteristic of this scale. However, while this decrease disappears in the 3.6 cm and $H\alpha$ spectra after source subtraction, it remains in the 20 cm spectrum. This implies that besides the bright HII regions there are sources of nonthermal emission within the spiral arms and central extended region which emit significantly at 20 cm.

To estimate how much of the wavelet energy $M(a)$ is provided by the subtracted sources, we consider the following definition:

$$\Delta(a) \equiv \frac{M_{or.}(a) - M_{s.s.}(a)}{M_{or.}(a)}, \quad (3.4)$$

where $M_{or.}(a)$ and $M_{s.s.}(a)$ represent the wavelet energy before and after source subtraction. Table 3.3 shows the fraction of energy produced by the 11 HII regions in IR and

⁵Gaussian PSFs with FWHM = 51'' and 84'' are considered to convolve the IR maps to the angular resolutions of the 20 and 3.6 cm radio maps, respectively.

Table 3.3: Fractions of the wavelet energy provided by the 11 brightest HII regions at different scales (Eq. 4).

λ	$\Delta(210'')$	$\Delta(505'')$	$\Delta(1020'')$
24 μm	0.94	0.81	0.35
70 μm	0.80	0.57	0.14
160 μm	0.52	0.33	0.11
3.6 cm	0.86	0.69	0.16

at 3.6 cm for 3 different scales (at $84''$ resolution). The corresponding fractions at 20 cm are not shown in this table, as some nonthermal radio sources were also subtracted at this wavelength. The emission at 24 μm has the largest energy fraction $\Delta(a)$ at all scales. The smallest $\Delta(a)$ occurs at 160 μm . This indicates that HII regions play a more important role in providing energy for dust emission at 24 μm than at 160 μm .

We estimate the uncertainties of the wavelet energies of each map by making a noise map with the distribution and amplitude of the real noise in the corresponding observed map. A linear combination of uniform and Gaussian distributions simulates the real noise in each observed image. The wavelet spectra of the derived noise maps were obtained using Eq. 3.3. The resulting wavelet energies of the noise maps are taken as the uncertainties of the wavelet energies of the observed maps at different scales. The estimated values are at least three orders of magnitude less than the wavelet energies of the observed maps. Therefore, the results from our wavelet spectrum analysis are not substantially affected by the noise in the maps.

3.5 Wavelet cross-correlations

A useful method to compare images at different wavelengths is the wavelet cross-correlation. The wavelet cross-correlation coefficient at scale a is defined as:

$$r_w(a) = \frac{\int \int W_1(a, \mathbf{x}) W_2^*(a, \mathbf{x}) d\mathbf{x}}{[M_1(a)M_2(a)]^{1/2}}, \quad (3.5)$$

where the subscripts refer to two images of the same size and linear resolution. The value of r_w varies between -1 (total anticorrelation) and +1 (total correlation). Plotting r_w against scale shows how well structures at different scales are correlated in intensity and location. The error is estimated by the degree of correlation and the number of independent points, n :

$$\Delta r_w(a) = \sqrt{\frac{1 - r_w^2}{n - 2}}, \quad (3.6)$$

where, $n = 2.13 \left(\frac{L}{a}\right)^2$, and L is the size of the maps.

First, we examine the cross-correlations between the 3 MIPS maps of M33 (Fig. 3.7). There are significant correlations between each pair of the MIPS maps at different scales within $0.4 < a < 4 \text{ kpc}$, as $r_w > 0.75$ (Frick et al. 2001). These scales include gas clouds,

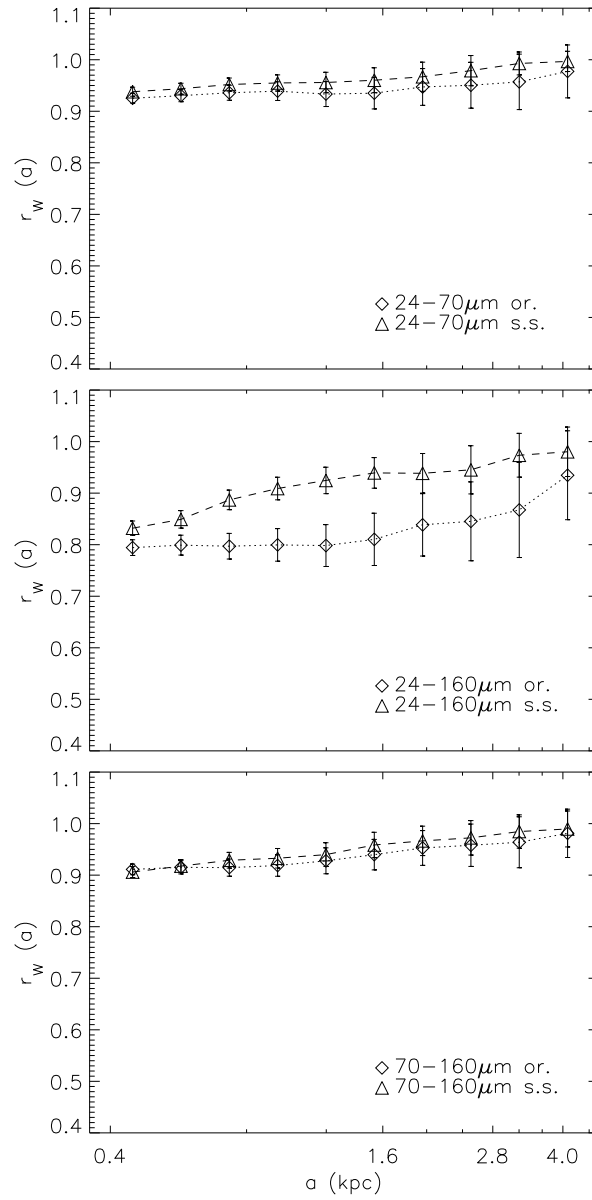


Figure 3.7: The cross-correlation between 24 and 70 μm (top), 24 and 160 μm (middle), and 70 and 160 μm (bottom) images at $51''$ resolution before (or.) and after (s.s.) source subtraction.

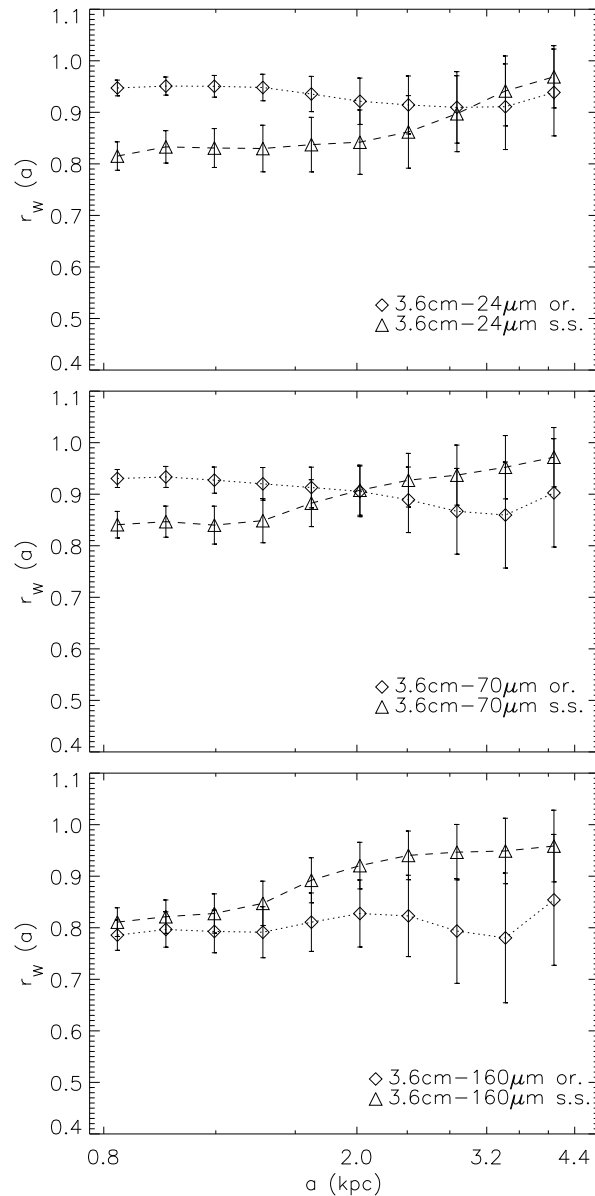


Figure 3.8: The cross-correlation between 3.6 cm radio and IR before and after subtraction of the same sources at $84''$ resolution.

spiral arms, and the central extended region. Comparing the plots, the 24–160 μm correlation is weaker than the two other correlations, especially at scales smaller than the spiral arms ($a < 400''$ or 1.6 kpc). This is due to significantly different contributions of HII regions in providing energy for dust emission at 24 and 160 μm (see Table 3.3), as the 24–160 μm correlation coefficients increase after subtracting these sources. This indicates that HII regions influence the correlations at scales larger than their sizes (the width of the huge HII region NGC604 is about $100''$ or 0.4 kpc).

Second, we study the cross-correlations between the infrared and the radio continuum emission at 3.6 cm. As shown in Fig. 3.8, the correlations between 3.6 cm radio and the

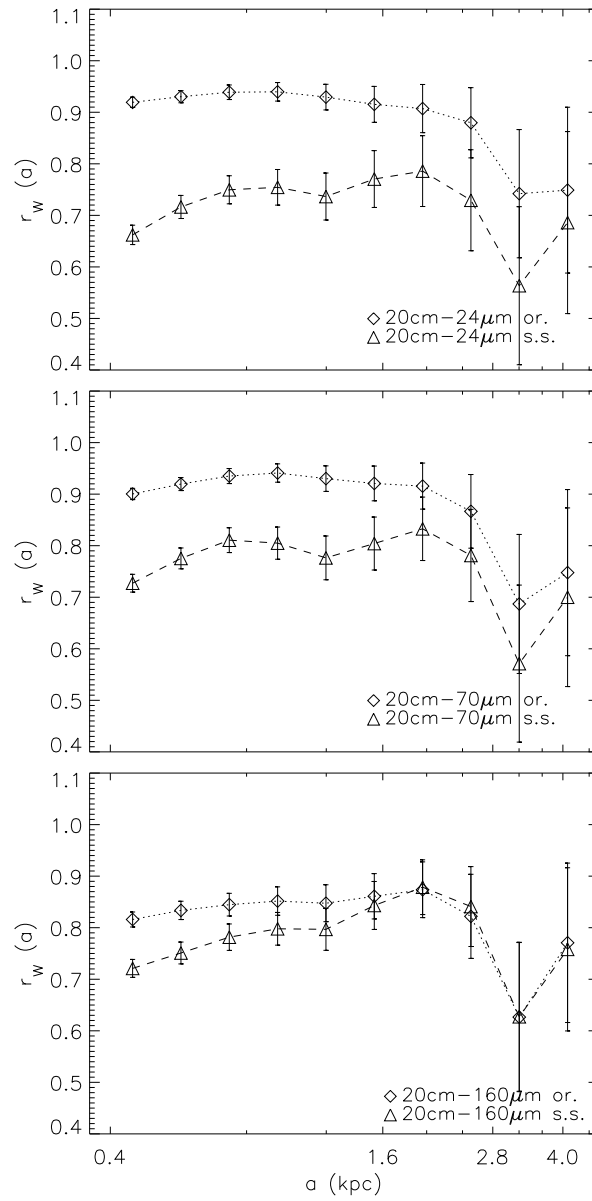


Figure 3.9: The correlation of the 20 cm radio with IR before and after subtraction of the same sources at $51''$ resolution (please note that this figure starts from $100''$ and not $200''$).

three infrared emission are strong at all scales. At scales smaller than the width of the spiral arms (1.6 kpc), the correlations are higher between 3.6 cm and 24 μm emission (and also 70 μm) than between 3.6 cm and 160 μm emission. The source subtraction reduces the 3.6 cm–24 μm and 3.6 cm–70 μm correlations at scales smaller than the spiral arms. This indicates that young massive stars are the most common and important energy sources of the 3.6 cm, 24 and 70 μm emission at these scales.

Third, the cross-correlations with the radio continuum emission at 20 cm are presented in Fig. 3.9. Before the source subtraction, the correlations between 20 cm radio and the three IR bands are strong at scales smaller than the width of the spiral arms. After the source subtraction, the coefficients of the IR–20 cm correlations decrease dramatically so that they become less than 0.75 at small scales. The reason is possibly that besides HII regions there are other unresolved sources of the 20 cm radio emission like supernova remnants that are stronger than at 3.6 cm but do not emit significantly in the infrared. Studies within our Galaxy have demonstrated that the ratio of far-infrared to radio continuum emission for supernova remnants is much smaller than that for HII regions (Fürst et al. 1987).

Comparing Fig. 3.8 with Fig. 3.9, a drop in correlation coefficient at the scale of 800'' (3.2 kpc) is more prominent in the MIPS correlations with 20 cm than with 3.6 cm. This is due to the strong minimum in the 20 cm spectrum at this scale (Fig. 3.5) that persists even after the source subtraction (in contrast to the situation in the 3.6 cm spectrum shown in Fig. 3.6).

3.6 Comparison with $\text{H}\alpha$

If we take the $\text{H}\alpha$ emission as a tracer of star forming regions that both heat the warm dust and ionize the gas giving the free–free emission, we expect a correlation between $\text{H}\alpha$ emission, IR and thermal radio emission. The cross-correlations involving $\text{H}\alpha$ and IR images are shown in Fig. 3.10. The significant correlation of $\text{H}\alpha$ with the 24 and 70 μm images at the smallest scale confirms that most of the compact structures in the MIPS decomposed maps at 24 and 70 μm (Fig. 3.3) correspond to the HII regions. The 160 μm emission is also correlated with $\text{H}\alpha$ emission, although the correlations are weaker than the correlations at 24 and 70 μm . It is deduced that the role of star forming regions in heating the dust, even the cold dust (emitting mainly at 160 μm), is generally important at scales smaller than 4 kpc.

Between $\text{H}\alpha$ and 3.6 cm there is a *perfect correlation* for both small-scale and extended structures: $r_w \geq 0.95$ (right panel in Fig. 3.10). This is not surprising as the wavelet spectra of the $\text{H}\alpha$ and 3.6 cm maps are very similar (see Fig. 3.6). Thus, not only are the star forming regions mostly responsible for the 3.6 cm emission, but also the radio continuum emission is dominated by the thermal free–free emission at 3.6 cm for $a < 4$ kpc.

After smoothing the 20 cm map to the spatial resolution of the 3.6 cm map, we obtain the $\text{H}\alpha$ –20 cm correlation (Fig. 3.10). At scales smaller than 600'' or 2.4 kpc, the coefficients are the same as for the $\text{H}\alpha$ –3.6 cm correlation. This means that the bright HII regions are also important sources of the 20 cm radio emission. It seems that the correlation decreases at larger scales, but it is not certain because of the large errors.

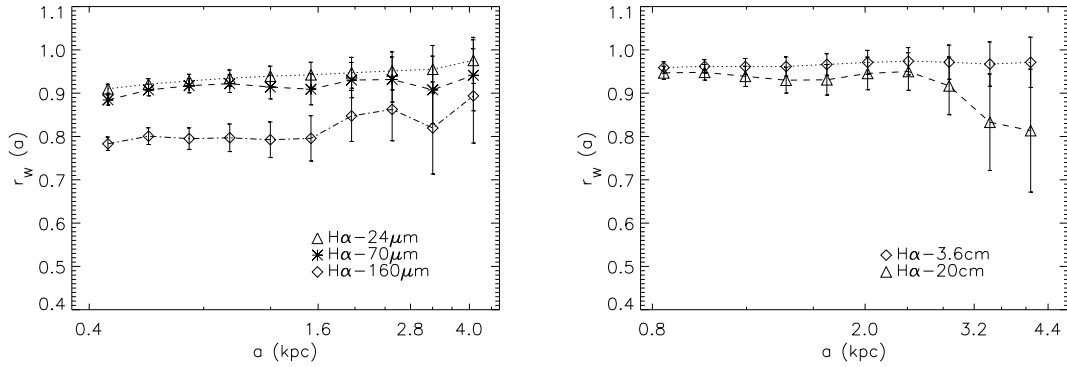


Figure 3.10: The correlation of H α with IR (top) at 51'' and with 3.6 and 20 cm radio (bottom) at 84'' resolution. The maps include all HII regions.

3.7 Discussion

We studied the spectral characteristics of the MIPS mid- and far-infrared, radio and H α maps and obtained cross-correlation coefficients between pairs of maps. Here, we discuss the implications of our results for the understanding of the energy sources powering the IR and radio emission from M33. Further, we compare the results of our analysis on M33 with that of Frick et al. (2001) on NGC 6946.

3.7.1 IR emission

From the wavelet analysis of the MIPS IR maps the following results are found.

- The 24 and 70 μm emission emerge mostly from the bright sources corresponding to star forming and HII regions. The influence of HII regions on the IR emission is highest at 24 μm (see Table 3.3). As expected, at small scales the 24 μm map is better correlated with the 70 μm than with the 160 μm map.
- The 160 μm emission emerges from both compact and extended structures. The compact structures correspond to star forming and HII regions. As shown in Table 3.3, the fraction of wavelet energy provided by the 11 brightest HII regions at 160 μm varies between 1/2 and 1/3 of that at 24 μm at different scales. The 160 μm map does not show small-scale dominance in its spectrum. The 160 μm spectrum shows an increase when it reaches the scale of complexes of dust and gas clouds of ~ 1 kpc, and a second increase in transition to the large-scale structures or diffuse dust emission.

While it is clear that the ionizing stars heat the warm dust, the mechanism heating the cold dust is still in debate. According to our wavelet analysis, the direct role of the young stellar population decreases with increasing IR wavelength. As shown in Table 3.3, at small scales ($< 200''$ or 0.8 kpc), the relative contribution of the 11 brightest HII regions to the total emission energy is about 50% at 160 μm which means that the contribution of all HII regions of M33 is much larger than 50%. Hence, it seems that at least up to scales

of 0.8 kpc the cold dust is effectively heated by UV photons from massive ionizing stars. On the other hand, the $160\ \mu\text{m}$ – $\text{H}\alpha$ correlation coefficients are smaller than those of the $24\ \mu\text{m}$ (or $70\ \mu\text{m}$)– $\text{H}\alpha$ correlation (Fig. 3.10). This means that the number of structures with a specific scale emitting strongly in both IR and $\text{H}\alpha$ becomes less at $160\ \mu\text{m}$. This indicates that besides UV photons from massive ionizing stars, other heating sources contribute also to heating the cold dust. These could be non-ionizing UV photons either from intermediate-mass stars (5 – $20\ M_{\odot}$) (Xu 1990) or from HII regions (Popescu et al. 2000, 2002; Misiriotis et al. 2001), or optical photons from solar mass stars (Xu & Helou 1996; Bianchi et al. 2000); they should contribute to an average radiation field as the $160\ \mu\text{m}$ wavelet spectrum is smooth.

Our findings confirm the arguments of e. g. Hinz et al. (2004), Devereux et al. (1994); Devereux et al. (1996, 1997) and Jones et al. (2002) that the IR is powered predominantly by young O/B stars, specifically at 24 and $70\ \mu\text{m}$. This is not necessarily at variance or in accordance with the argument of Xu & Helou (1996) that only 27% of the diffuse dust emission from M31 can be attributed to the heating by UV photons, because of two reasons. First, our wavelet study does not include diffuse structures with scales larger than 4 kpc. Second, the late-type galaxy M33 is more densely populated with young stars than the earlier-type galaxy M31. This may mean that the relative role of young stars in heating the dust increases with later galaxy type (Sauvage & Thuan 1992). For a more precise comparison, it is necessary to accomplish wavelet analysis for other nearby galaxies.

Hoernes et al. (1998) showed that the cold dust emission in M31 has a weaker correlation with the thermal radio than with the nonthermal radio emission. Since the contribution of the thermal emission is higher at 3.6 cm than at 20 cm, one may expect a weaker correlation between the $160\ \mu\text{m}$ and 3.6 cm emission. In M33, we did not find significant differences between the $160\ \mu\text{m}$ –3.6 cm and $160\ \mu\text{m}$ –20 cm correlations (Figs. 3.8 and 9) at scales of $200''$ (0.8 kpc) $< a < 700''$ (2.8 kpc), even after subtracting strong thermal sources (bright HII regions). This could be due to the larger role of UV photons from O/B stars in heating the cold dust in M33 than in M31, as discussed in the previous paragraph. However, a better $160\ \mu\text{m}$ correlation with the nonthermal than with the thermal radio is probable at the scale of the whole galaxy. For instance, Hinz et al. (2004) showed that the morphology of the smoothed $160\ \mu\text{m}$ emission from M33 is most similar to that of the radio emission at 17.4 cm.

3.7.2 Radio emission and radio–IR correlation

From the wavelet analysis of the radio maps we obtain the following results for the 3.6 and 20 cm emission from M33.

- The shape of the 3.6 cm wavelet spectrum is very similar to that of the $\text{H}\alpha$ spectrum (Fig. 3.6) and, hence, there is a perfect correlation between 3.6 cm and $\text{H}\alpha$ at all scales (Fig. 3.10). This indicates that not only the star forming regions are mostly responsible for the radio emission at 3.6 cm, but also the thermal (free–free) emission is significant at this wavelength. But it could also be that the nonthermal (synchrotron) emission correlates well with the thermal emission. Our recent estimation of the thermal fraction of the 3.6 cm radio continuum emission gives

$f_{th} \sim 50\%$ for the whole galaxy including the extended disk emission (Tabatabaei et al., in prep.). As a higher percentage of the thermal fraction is expected at scales ≤ 4 kpc, this result is consistent with our wavelet study. The nearly parallel 3.6 cm and $H\alpha$ wavelet spectra indicates that extinction is scale-independent and has no significant effect on $H\alpha$ emitting structures.

- The combined 20 cm (VLA+Effelsberg) wavelet spectrum represents both compact and diffuse structures of thermal and nonthermal emission. The bright HII regions (or complexes) give strong contribution to the 20 cm emission. The strong $H\alpha$ –20 cm correlation at scales smaller than the width of the central extended region (~ 2.5 kpc) also indicates that the nonthermal emission correlates perfectly with the thermal emission at these scales.
- Generally, there are strong 3.6 cm–IR correlations at all scales in the range of 0.8–4 kpc within M33 (Fig. 3.8). The 3.6 cm correlations with 24 and 70 μm are better than that with 160 μm before subtracting bright HII regions. However, these correlations become approximately the same after subtracting HII regions. That is because the 24 and 70 μm emission are more influenced by the HII regions than the 160 μm emission.
- The strong 20 cm–IR correlations are mainly due to the bright HII regions, as the correlations fall after source subtraction (Fig. 3.9). Here, the weakest correlation is between the 20 cm and the 24 μm maps. This indicates that the nonthermal sources which are associated with star forming regions are not as effective as HII regions in heating the dust.

In their multi-resolution analysis of the radio–IR correlation in the LMC, Hughes et al. (2006) found strong correlations in the regions where the thermal fraction of the radio emission is high. This is in agreement with our results that the 24 and 70 μm –radio correlations are higher before subtracting HII regions. Even, the 160 μm –20 cm correlation follows this pattern before subtracting the thermal radio regions. For NGC6946, Frick et al. (2001) also found a better correlation between the thermal 3.6 cm radio and IR emission up to scales of the width of spiral arms, although the nonthermal emission dominates in this galaxy (Ehle & Beck 1993). There are indications for similar trends in other nearby galaxies (Murphy et al. 2006).

3.7.3 Comparison with NGC 6946

It is instructive to compare the results of the wavelet analysis of M33 with those obtained by Frick et al. (2001) for NGC 6946, which is also a late-type Scd galaxy.

NGC 6946 was studied at a linear resolution of 0.4 kpc corresponding to our analysis at $84''$ HPBW. Comparing Fig. 3.6 (in this paper) to Fig. 3.7 in the Frick et al. (2001) paper at scales between 0.8 and 4 kpc, the dominant scale of the $H\alpha$ wavelet spectrum is at the scale of the width of the spiral arms (1.5 kpc) in NGC 6946, while in M33 it is at the smallest scale ($\sim 200''$ or 0.8 kpc in Fig. 3.6). Even after subtracting the 11 brightest HII regions the scales corresponding to the spiral arms ($\sim 400''$) are not dominant in M33. This is because the spiral arms in M33 are not as pronounced as those in NGC 6946. Instead, the $H\alpha$ emission in M33 has a rather clumpy distribution.

The spectrum of dust emission from NGC 6946 at 12–18 μm shown in Fig. 3.7 in the Frick et al. (2001) paper is more similar to the spectrum of dust emission from M33 at 160 μm than to that at 24 μm . So, the excess of hot dust emission near the massive stars found in M33 is not visible in NGC 6946.

Frick et al. (2001) found signatures of three-dimensional Kolmogorov-type turbulence (Kolmogorov 1941) for the ionized gas ($\text{H}\alpha$ and thermal radio continuum emission at 3.6 cm) at scales less than 0.6 kpc in NGC 6946. An increasing part of the spectrum ($\log I - \log a$) with a slope of 5/3 is typical for this type of turbulence (Spangler 1991). They obtained this slope considering the first point at the scale of 0.3 kpc (the resolution of their maps was 0.4 kpc), making the slope estimate of 5/3 uncertain. At the same resolution we cannot investigate this turbulence for M33, as the smallest scale in Fig. 3.6 is larger than 0.6 kpc. However, at higher spatial resolutions the spectra of the radio, IR, and $\text{H}\alpha$ emissions from M33 do not show such an increase at scales less than 0.6 kpc (Figs. 3.4 and 3.5). The steepest increasing slope is about 1.1 at scales between 140 and 320 pc (in the 24 μm spectrum) (Fig. 3.4). The slopes become less at 51'' resolution (Fig. 3.5). They vary between 0 and 0.6 at increasing parts of the spectra and between 0 and -0.9 at decreasing parts of the spectra. After subtracting HII regions, the slopes become even flatter.

Comparing Fig. 3.12 in the Frick et al. (2001) paper to Fig. 3.10 (in this paper), the 3.6 cm– $\text{H}\alpha$ cross-correlation coefficients are less at the small scales in NGC 6946 than in M33. As the extinction is proportional to the dust density and because higher dust densities can be found at smaller scales, one expects more extinction of $\text{H}\alpha$ at smaller scales. This leads to a weaker correlation with the radio free-free emission at smaller scales. Hence, it seems that absorption by dust at scales < 1.2 kpc (Fig. 3.12, Frick et al. 2001) is less significant in M33 than in NGC 6946. The existence of considerable extinction in NGC 6946 caused by a patchy dust distribution has been shown by Trewhealla (1998).

3.8 Conclusions

Highly resolved and sensitive Spitzer MIPS images of M33 at 24, 70, and 160 μm enabled us to compare the morphology of different dust components of this galaxy. A 2D-wavelet transformation was used to find dominant scales of emitting structures and correlations of the MIPS images with new radio (3.6 and 20 cm) maps as well as with an $\text{H}\alpha$ image of M33. We compared the results of wavelet analysis with and without bright HII regions at different resolutions (18'', 51'', 84''). We found that at a characteristic scale of 210'' or 0.8 kpc, 80% or more of the wavelet energy at 24 and 70 μm and 3.6 cm is from the 11 brightest HII regions. These sources cause better correlations between pairs of the 24 and 70 μm and 3.6 cm maps, while they cause a smaller 24–160 μm correlation. Bright HII regions improve the correlations between the 20 cm radio map and each of the MIPS IR maps. The $\text{H}\alpha$ emission shows a better correlation with IR emission at 24 and 70 μm than at 160 μm . It is perfectly correlated with the 3.6 cm radio emission out to scales of 4 kpc and also with the 20 cm radio emission out to scales of the width of the central extended region (~ 2.5 kpc). This is understandable because the radio continuum emission at 3.6 cm is dominated by thermal emission and that at 20 cm by nonthermal emission.

The most important conclusions of this study are:

- The longer the IR wavelength, the more extended is the distribution of dust grains emitting at that wavelength (Sects. 3.3 and 3.4).
- HII regions influence the IR emission with a strength inversely depending on wavelength: more influence at $24\ \mu\text{m}$ and less influence at $160\ \mu\text{m}$ (Sect. 3.4).
- The nonthermal radio emission correlates well with the thermal radio and $\text{H}\alpha$ emission out to the scale of the central extended region, $\sim 2.5\ \text{kpc}$ (Sect. 3.7).
- The warm dust–thermal radio correlation is stronger than the cold dust–nonthermal radio correlation at scales smaller than $4\ \text{kpc}$ (about half the size of the galaxy) (Sects. 3.5 and 3.7).
- The effect of extinction in $\text{H}\alpha$ is independent of the scale of structures in M33 and is smaller than in NGC6946.

In Chapter 4, we obtain maps of the thermal and nonthermal radio continuum emission and compare them with the IR emission, separately.

4 Thermal and nonthermal radio emission from M33

4.1 Introduction

The problem of separating the two components of the radio continuum emission, free-free (thermal) and synchrotron (nonthermal) emission, dates back to the beginnings of radioastronomy. The mostly applied techniques are based on either assuming a constant nonthermal spectral index (e.g. Klein et al. 1984) or a correlation between thermal radio and infra-red (IR) emission (Broadbent et al. 1989).

Although the assumption of constant nonthermal spectral index may be reasonable for global studies (Sect. 4.10), it does not lead to a feasible thermal/nonthermal distribution in detailed studies. Under this simplification, it is not possible to investigate the origin and energy loss processes of the electron component of cosmic rays (CRs) within a galaxy. Discrete synchrotron emitting sources are mainly identified as supernova remnants. The synchrotron emission from supernova remnants can be described as power law ($S_\nu \sim \nu^{-\alpha_n}$) with a typical spectral index of $\alpha_n \simeq 0.6$. Propagating from these sources, electrons suffer energy losses that steepens the power law spectrum. In the interstellar medium, the typical spectral index attributed to the emission under the leakage loss is $\simeq 0.9$, and under synchrotron loss and inverse Compton scattering $\simeq 1.1$ (Biermann 1995). These electrons further diffuse to the interarm regions and outer parts of spiral galaxies within their life time. Hence, variations of the nonthermal spectral index should be distinguishable particularly by comparing arms with interarm regions and outer parts of the galaxies.

The thermal/nonthermal separation based on the assumption that the radio-IR correlation is due to a correlation between the thermal radio and IR emission is not generally correct, as nonthermal phenomena e.g. super massive black holes or energetic CRs may stimulate the IR emission. For instance, the possibility of heating the diffuse dust (emitting in IR) by CRs was shown by Helou & Bicay (1993) and Bicay & Helou (1990). Moreover, supernovae, the ultimate sources of most of the nonthermal emission, explode close to the star-forming regions in which their progenitor stars formed. Together with the increased magnetic field strength in the spiral arms, this causes a correlation between the thermal and nonthermal sources, making a less direct link between the IR and thermal emission. Finally, the slope of the radio-IR correlation depends on the synchrotron spectral index (Niklas & Beck 1997).

Templates for free-free emission could be provided by emission of recombination lines as they originate from within ionized regions, like the free-free emission. The $H\alpha$

emission, the strongest Balmer line, is observationally most preferred, particularly from nearby galaxies. Both the $H\alpha$ and free-free emission are linearly proportional to the number of ionizing photons produced by massive stars. On the other hand, the $H\alpha$ emission suffers from extinction by dust leading to an underestimate of the free-free emission if no extinction correction is made. Note that the emission of radio recombination lines is extinction free and hence ideal for tracing the free-free emission. However, these kinds of emission are too weak from the diffuse ionized gas in external galaxies to be detected using the present facilities. For example, our attempt to map radio recombination lines emission from diffuse regions within IC 342 and M33 using the 6.2 cm receiver of the Effelsberg Telescope was not successful.

The nearest Scd galaxy, M33 (NGC 598), at a distance of 840 kpc ($1'' \simeq 4$ pc, Freedman et al. 1991) has been extensively studied at radio and IR wavelengths. With an inclination of $i = 56^\circ$ (Regan & Vogel 1994), its spiral structure is well visible. So far, extinction studies in M33 have mostly focused on HII regions using either the Balmer (and Paschen) line ratios (e.g. Kwitter & Aller 1981; Melnick et al. 1987; Petersen & Gammelgaard 1997) or the ratio of $H\alpha$ to radio emission (e.g. Israel & Kennicutt 1980; Devereux et al. 1997). In the line ratio method the emission from the diffuse ionized medium can hardly be detected in most of these recombination lines. The method based on the radio emission only works well when the thermal component of the radio continuum is independently known. For instance, the radio emission from single HII regions (and not HII complexes with a possible nonthermal emission contribution like NGC 604 and NGC 595, Dodorico 1978; Gordon et al. 1993) may be considered as the thermal emission.

Using the ISOPHOT 60 and $170 \mu\text{m}$ data, Hippelein et al. (2003) found an anticorrelation between the flux density ratio of $H\alpha/60 \mu\text{m}$ and $170 \mu\text{m}$ flux density, suggesting the extinction to be related to the cold dust in M33.

We obtain the distribution of the dust optical depth at the $H\alpha$ wavelength for the whole M33 (an extinction map) by analysis of dust emission and absorption using the high sensitivity and resolution Multiband Imaging Photometer Spitzer (MIPS, Rieke et al. 2004) FIR data at 70 and $160 \mu\text{m}$. This leads to an $H\alpha$ map corrected for extinction (de-extincted $H\alpha$ map), our free-free template. The thermal and nonthermal maps at 3.6 and 20 cm are obtained at an angular resolution of $90''$ (equivalent to a linear resolution of 360 pc) by both the new (using a free-free template) and the standard method (assuming a constant nonthermal spectral index) and the results are compared. Further, we determine variations of the nonthermal spectral index across M33 as detected by the new method and discuss the exponential scale lengths of both thermal and nonthermal emission.

In Sect. 4.3 we derive distribution of dust color temperature. This temperature and the $160 \mu\text{m}$ flux density are used to obtain the dust optical depth (extinction) and its distribution in Sects. 4.4 and 4.5. We correct the $H\alpha$ emission for the extinction and then convert it to the thermal radio emission, following Dickinson et al. (2003) (Sect. 4.6). The nonthermal intensity and spectral index maps are produced in Sects. 4.7 and 4.8. We discuss and compare the results from the new and standard methods in Sect. 4.9. Finally, conclusions are presented in Sect. 4.10.

4.2 Data

The radio continuum data at 3.6 and 20 cm were presented in Chapter 2 (Tabatabaei et al. 2007c). At 3.6 cm, M33 was observed with the 100-m Effelsberg telescope of the MPIfR¹. The 20 cm data were obtained from observations with the Very Large Array (VLA²) corrected for missing spacing using the Effelsberg data at 20 cm. We also used the latest combined epochs of MIPS Spitzer data at 70 and 160 μm (as presented in Tabatabaei et al. 2007a, 2005). The H α map is from Kitt Peak National Observatory (KPNO) (Hoopes & Walterbos 2000).

4.3 Temperature distribution of dust

The intensity I_ν towards a uniform dust layer of optical thickness τ_ν and temperature T is

$$I_\nu = B_\nu(T) (1 - e^{-\tau_\nu}) , \quad (4.1)$$

so that an observer receives from a solid angle Ω the flux

$$F_\nu = B_\nu(T) (1 - e^{-\tau_\nu}) \Omega . \quad (4.2)$$

The flux ratio at two frequencies, marked by the subscripts 1 and 2, becomes

$$\frac{F_1}{F_2} = \frac{B_1(T) [1 - e^{-\tau_1}] \Omega_1}{B_2(T) [1 - e^{-\tau_2}] \Omega_2} . \quad (4.3)$$

It is customary to obtain the dust temperature from (4.3) under the following conditions:

- The emission is optically thin, which is usually true in the FIR.
- The observational frequencies do not lie in the Rayleigh-Jeans limit of the Planck function.
- The dust temperature in the source is uniform.
- The ratio of the dust absorption coefficients, κ_1/κ_2 , over the frequency interval from ν_1 to ν_2 , or equivalently the exponent β in $\kappa_\nu \sim \nu^\beta$ (Sect. 1.4) is known.

Then Eq. (4.3) simplifies to

$$\frac{F_1}{F_2} = \frac{\nu_1^\beta}{\nu_2^\beta} \frac{B_1(T)}{B_2(T)} . \quad (4.4)$$

We use the Spitzer FIR maps at 70 μm and 160 μm and obtain an average dust temperature attributed to each pixel. The power law index of the absorption efficiency at the FIR wavelengths, β , is set to 2, which should be appropriate for interstellar grains at $\lambda > 30 \mu\text{m}$ (Krügel 2003; Andriess 1974; Draine & Lee 1984). The MIPS FIR maps

¹The 100-m telescope at Effelsberg is operated by the Max-Planck-Institut für Radioastronomie (MPIfR) on behalf of the Max-Planck-Gesellschaft.

²The VLA is a facility of the National Radio Astronomy Observatory. The NRAO is operated by Associated Universities, Inc., under contract with the National Science Foundation.

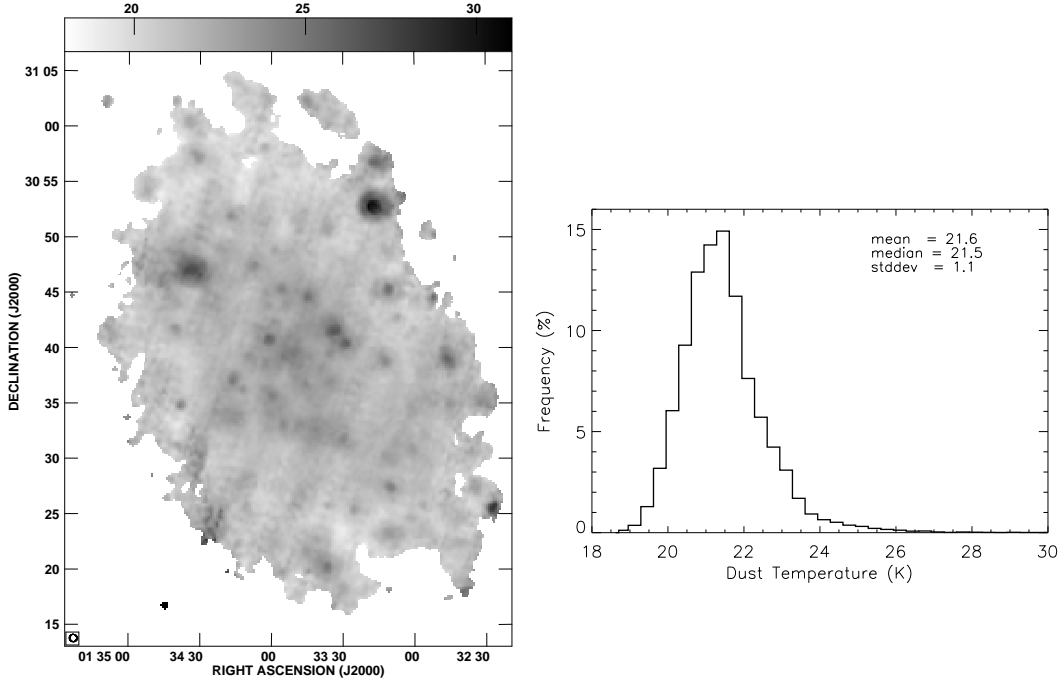


Figure 4.1: *Left*: dust temperature map of M33 obtained from $I_{70\mu\text{m}}/I_{160\mu\text{m}}$ ratio (only pixels with intensity above 3σ level were used). The angular resolution of $40''$ is shown in the lower left-hand corner of the map. The bar at the top gives the dust temperature in Kelvin. *Right*: Histogram of the dust temperature map. It shows the population of pixels as a function of the temperature intervals. The number of bins used for this plot is 80.

at 70 and $160\mu\text{m}$ have been smoothed to an angular resolution of $40''$ and normalized to the same grid and center position. The resulting dust temperature distribution is shown in Fig. 4.1, indicating variations between 19 and 28 K. Fig. 4.1 displays the relative frequency of occurrence of the temperature intervals in $10'' \times 10''$ pixels. The maximum is attained at 21.5 K, close to the mean value of 21.6 K. Warmer dust with $T > 25$ K dominates in star-forming regions and in the center of the galaxy. The highest temperatures are found in the HII complexes NGC 604, NGC 592, and IC 133.

4.4 Optical depth at $160\mu\text{m}$

Having determined T , we obtain the optical depth from the equation

$$\tau_{160\mu\text{m}} = I_{160\mu\text{m}}/B_{160\mu\text{m}}(T) , \quad (4.5)$$

where $I_{160\mu\text{m}}$ is the intensity. The distribution of $\tau_{160\mu\text{m}}$ over the disk in M33 is plotted in Fig. 4.2. Because the temperature variations are very moderate, the optical depth $\tau_{160\mu\text{m}}$ usually follows the $160\mu\text{m}$ intensity map quite closely (see Tabatabaei et al. 2007a). Nevertheless, for a fixed intensity, a warm region (26 K) has a three times lower optical depth than a cold one (19 K).

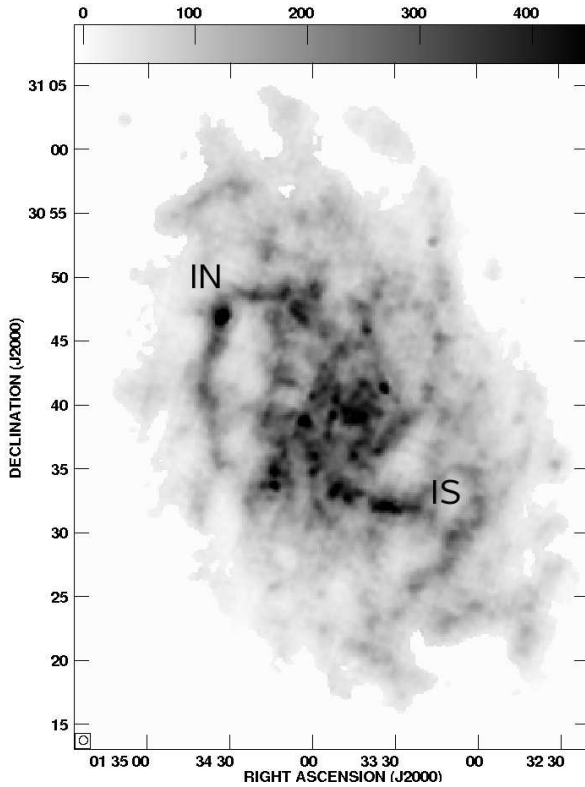


Figure 4.2: Distribution of the dust optical depth at $160\ \mu\text{m}$ wavelength in M33. The bar at the top shows $10^6 \times \tau_{160\ \mu\text{m}}$. The main northern (IN) and southern (IS) spiral arms are indicated. The angular resolution of $40''$ is shown in the lower left-hand corner of the map.

4.5 Distribution of extinction

To convert $\tau_{160\ \mu\text{m}}$ into the dust optical depth at the wavelength of the $\text{H}\alpha$ line, $\tau_{\text{H}\alpha}$, we have to multiply it by $\kappa_{\text{H}\alpha}/\kappa_{160\ \mu\text{m}}$, the ratio of the dust extinction coefficient per unit mass at the corresponding wavelengths. Using the extinction curve given by a standard dust model for the diffuse medium (see, e.g. Figure 12.8 of Krügel 2003), we estimate $\tau_{\text{H}\alpha} \simeq 2200 \tau_{160\ \mu\text{m}}$. Therefore, after multiplication with 2200, Fig. 4.2 gives also the distribution of $\tau_{\text{H}\alpha}$ across the galaxy at a linear resolution of 360 pc.

$\tau_{\text{H}\alpha}$ is around one half in the extended central region and in the two main arms, IN and IS, and it is somewhat smaller in other arms (mostly between 0.2 and 0.4). In the center of the galaxy and in massive star forming regions, specifically in the southern arm IS and the HII complexes NGC604, NGC595, and B690, $\tau_{\text{H}\alpha}$ exceeds 0.7. The highest dust optical depth one finds in the center of the galaxy and in NGC604 where $\tau_{\text{H}\alpha} \simeq 0.97$ and 0.88, respectively (at the linear resolution of 360 pc). Therefore, M33 is generally almost transparent for photons with $\lambda \simeq 6560\ \text{\AA}$ propagating towards us.

To estimate how much the detected $\text{H}\alpha$ radiation has been attenuated, we note that $\text{H}\alpha$ photons are usually emitted from sources *within* the galaxy. The optical depth $\tau_{\text{H}\alpha}$ therefore only gives an upper limit. Following Dickinson et al. (2003), we define f_d , the effective dust fraction in the line of sight actually absorbing the $\text{H}\alpha$ so that the effective thickness is $\tau_{\text{eff}} = f_d \times \tau_{\text{H}\alpha}$ with $f_d < 1$ (note that $f_d = 1$ or the whole thickness is used for correcting the $\text{H}\alpha$ emission from background sources); the attenuation factor for the $\text{H}\alpha$ flux is then $e^{-\tau_{\text{eff}}}$.

At 360 pc resolution, one may assume that the $\text{H}\alpha$ emitters, ionized gas in HII regions

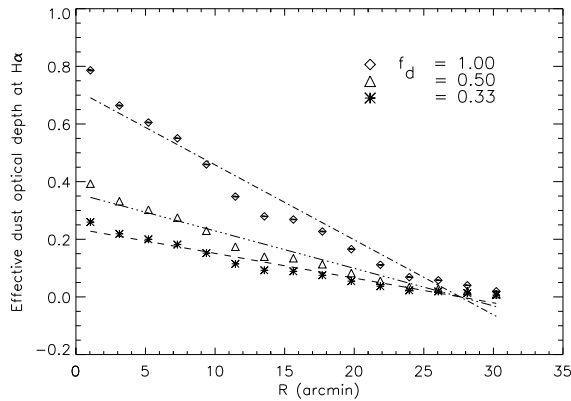


Figure 4.3: Radial distribution of the mean effective optical depth at H α (τ_{eff}) in rings of width of 0.5 kpc in the galactic plane for $f_d = 0.33$, 0.5 and 1.0. The errors are smaller than the size of the symbols.

and diffuse gas, are uniformly mixed with the dust, which would imply $f_d \simeq 0.5$. Dickinson et al. (2003) found $f_d = 0.33$ for the Milky Way (because the z-distribution of the H α emission is smaller than that of the dust) and we adopt their value also for M33. But, as will be shown in Sect. 4.9.4, the determination of the thermal fraction of the radio emission is not very sensitive to the particular choice of f_d .

Of course, it would be preferable not to use a uniform value f_d for the whole galaxy, but one that is adapted to the geometry (well mixed diffuse medium or shell-like in HII regions, Witt & Gordon 2000) and the dust column density. This needs to specify the location of the stellar sources and the absorbing dust and to solve the radiative transfer problem with massive numerical computations. Gordon et al. (2000) developed a flux ratio method to determine the dust attenuation which accounts for different geometries using a Monte Carlo radiative transfer model together with a stellar evolutionary synthesis model. These models are not used in this study, as they would require additional assumptions as well as more data to constrain them.

An interesting related question is how the extinction in M33 changes with galactic radius R . To investigate this, we integrated Spitzer FIR flux densities at 70 and 160 μm in rings of 0.5 kpc width in the galactic plane (inclination of 56° , Regan & Vogel 1994). We first derived the mean dust temperature of each ring and then the mean dust optical depth τ_{eff} . Fig. 4.3 shows τ_{eff} versus the galactocentric radius R . For $f_d = 0.33$, the dependence can be described by $\tau_{\text{H}\alpha}(R) = (-0.009 \pm 0.002) R + (0.24 \pm 0.03)$. As f_d rises, the slope gets steeper. The case $f_d = 1$ (for the full layer), which is appropriate for pure background sources of M33, is shown for comparison. Generally, a decrease of the extinction with galactocentric radius is expected as it reflects the decrease in surface density towards the periphery. From a comparison of H α data with radio flux densities at 6.3 and 21 cm, Israel & Kennicutt (1980) and Berkhuijsen (1982, 1983) found a rather steep radial gradient of the extinction: considering 8 bright HII regions, Berkhuijsen (1982) derived the relation $\tau_{\text{H}\alpha} = A_{\text{H}\alpha}/1.086 = (-0.038 \pm 0.003) R + (1.45 \pm 0.05)$, with R in arcmin. Qualitatively similar results were reported by Petersen & Gammelgaard (1997),

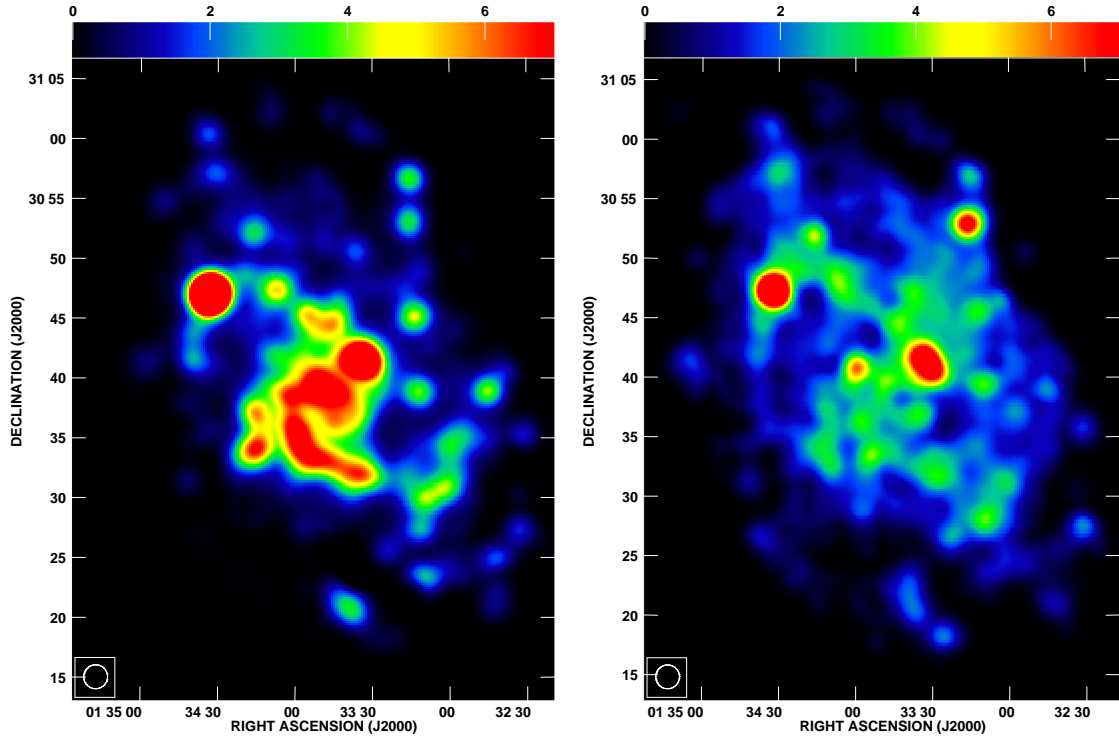


Figure 4.4: Thermal (*left*) and nonthermal (*right*) maps at 3.6 cm. The grey-scale gives the flux density in mJy/beam. The angular resolution is $90''$ (shown in the lower left of the images) with a grid size of $10''$. The bright HII complexes NGC604 (RA = $1^h 34^m 32.9^s$ & DEC = $30^\circ 47' 19.6''$) and NGC 595 (RA = $1^h 33^m 32.4^s$ & DEC = $30^\circ 41' 50.0''$) are clearly visible in both maps, whereas IC133 (RA = $1^h 33^m 15.3^s$ and DEC = $30^\circ 53' 19.7''$) appears stronger in the nonthermal map.

using Balmer and Paschen emission lines, and by Hippelein et al. (2003) based on a study of the $H\alpha$ to the $60 \mu\text{m}$ ISOPHOT flux ratio in HII regions. The only discrepant result by Devereux et al. (1997) who, from their pixel-to-pixel comparison of $H\alpha$ and 6 cm thermal radio maps, did not find any systematic decline in A_V , Hippelein et al. (2003) were able to explain by assuming that the radial gradient of the cold dust ($170 \mu\text{m}$ ISOPHOT) is stronger in the HII regions than in the diffuse gas.

4.6 Distribution of free-free emission

From the observed $H\alpha$ intensity, I , and the effective extinction, τ_{eff} , we derive the intrinsic $H\alpha$ intensity, I_0 , according to

$$I = I_0 e^{-\tau_{\text{eff}}} . \quad (4.6)$$

Note that using this equation is likely that we solve the radiative transfer equation for an artificial absorbing medium with an effective thickness τ_{eff} in front of an only emitting medium. In a more realistic approach, one should solve the radiative transfer equation

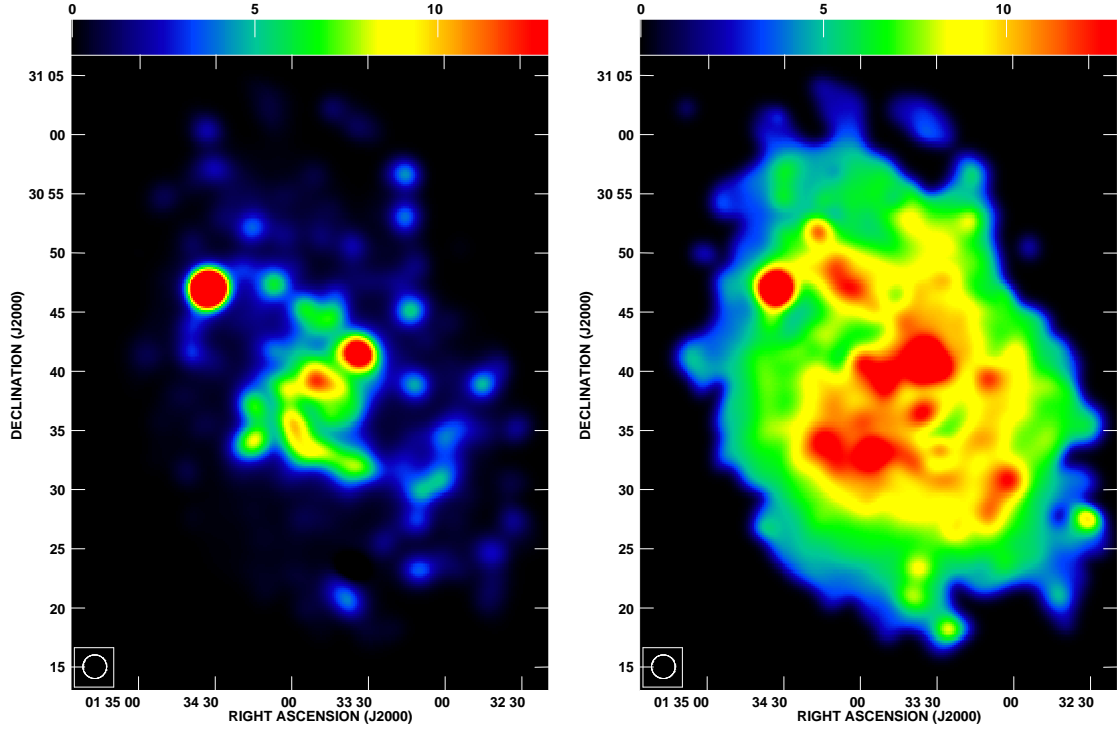


Figure 4.5: Thermal (*left*) and nonthermal (*right*) maps at 20 cm. The grey-scale gives the flux density in mJy/beam. The angular resolution is $90''$ (shown in the lower left of the images) with a grid size of $10''$.

considering a mixed distribution of emitters and absorbers. Usually, solving the radiative transfer equation needs massive numerical computations and additional free parameters. However, for a homogeneous distribution of emitters and an optically thin condition ($\tau \leq 1$) a mixed medium of sources and absorbers is equivalent to consider an effective absorber medium of $\tau_{\text{eff}} (= \frac{1}{2} \tau)$ in front of the emitting medium (see Appendix C).

Integration of the $H\alpha$ maps out to a radius of 7.5 kpc yields a ratio of corrected to observed total $H\alpha$ flux density of 1.13 for $f_d = 0.33$ and 1.25 for $f_d = 0.5$. Thus only 13% (25%) of the total $H\alpha$ emission is obscured by dust. The small extinction within M33 was predicted by the wavelet study of 3.6 cm and $H\alpha$ emission (Tabatabaei et al. 2007a).

The emission measure (EM) follows from the $H\alpha$ intensity via the expression Valls-Gabaud (1998)

$$I_{H\alpha} = 9.41 \times 10^{-8} T_{e4}^{-1.017} 10^{-\frac{0.029}{T_{e4}}} \text{EM}, \quad (4.7)$$

where the electron temperature, T_{e4} , is in units of 10^4 K, EM in $\text{cm}^{-6} \text{pc}$, and it is assumed that the optical depth of HI resonance lines is large (usually denoted as case B). Taking into account the contribution from the fraction of He atoms, all of which are assumed to be singly ionized, Eq. (1.22) is written as

$$\tau_\nu = 8.235 \times 10^{-2} a T_e^{-1.35} \nu_{\text{GHz}}^{-2.1} (1 + 0.08) \text{EM}. \quad (4.8)$$

Table 4.1: Estimated thermal flux density and thermal fraction at 3.6 cm ($f_d=0.33$ and $T_e=10,000$ K).

Object	Observed flux density (mJy)	Thermal flux density (mJy)	Thermal fraction %
NGC604	50.44 ± 0.13	38.55 ± 0.08	76.4 ± 0.3
NGC595	17.95 ± 0.18	12.13 ± 0.11	67.6 ± 0.9
IC133	9.08 ± 0.11	2.66 ± 0.04	29.3 ± 0.5
B690	4.51 ± 0.11	3.11 ± 0.10	68.9 ± 2.7
B61/62	3.72 ± 0.11	2.24 ± 0.07	60.2 ± 2.6
IC132	4.89 ± 0.05	3.25 ± 0.02	66.5 ± 0.8
IC131	4.59 ± 0.07	3.26 ± 0.05	71.0 ± 1.5
NGC588	4.64 ± 0.09	3.24 ± 0.06	69.8 ± 1.8
IC142	3.51 ± 0.08	2.73 ± 0.10	77.8 ± 3.3
B691	4.60 ± 0.13	2.35 ± 0.06	51.1 ± 2.0
NGC592	4.28 ± 0.08	2.76 ± 0.06	64.5 ± 1.9
M33 (mJy):			
R < 7.5 kpc	761 ± 63	391 ± 74	51.4 ± 10.6

The brightness temperature of the radio continuum emission, T_b , then follows from

$$T_b = T_e (1 - e^{-\tau_\nu}). \quad (4.9)$$

At $\nu = 1.4$ GHz, the calculated τ_ν is smaller than 4×10^{-4} in M33 (at 360 pc linear resolution), hence the optically thin condition is valid: $T_b = T_e \tau_\nu$. Finally, the free-free brightness temperature in terms of the $H\alpha$ intensity is given by

$$\frac{T_b}{I_{H\alpha}} = 3.484 \times 10^4 a \nu_{\text{GHz}}^{-2.1} T_e^{0.667} 10^{\frac{0.029}{T_e^4}} (1 + 0.08). \quad (4.10)$$

Whereas the electron temperature in the Milky Way is known to increase with galactocentric radius (Shaver et al. 1983) as a result of decreasing metallicity (Panagia 1979), M33 does not show significant variations in metallicity (e.g. Willner & Nelson-Patel 2002; Magrini et al. 2007). Crockett et al. (2006) derived the electron temperature from forbidden line ratios in 11 HII regions with galactocentric distances from 1 to 7 kpc. Their T_e values range from 7300 K to 12800 K with a mean value of 10,000 K and no clear radial gradient. As there are no T_e measurements for the diffuse ionized gas in M33, we adopt a fixed value of $T_e = 10,000$ K.

The conversion factors from brightness temperature (K) to the observed radio flux density (Jy/beam) are 2.6 and 74.5 at 3.6 and 20 cm, respectively. The final free-free maps are shown in Figs. 4.4 and 4.5. At both wavelengths, the strongest thermal emission emerges from HII regions, in particular, the HII complexes NGC604 and NGC595, but the southern arm IS (Chapter 2) and the center of the galaxy are also very bright. At both wavelengths, the thermal fraction of the diffuse emission is $< 25\%$ in interarm regions. The average error in the thermal fraction obtained using the error propagation method is 7%.

Table 4.2: Estimated thermal flux density and thermal fraction at 20 cm ($f_d=0.33$ and $T_e=10,000$ K).

Object	Observed flux density (mJy)	Thermal flux density (mJy)	Thermal fraction %
NGC604	62.75 ± 0.21	45.46 ± 0.09	72.4 ± 0.2
NGC595	20.50 ± 0.22	14.31 ± 0.14	69.8 ± 1.0
IC133	5.35 ± 0.07	3.11 ± 0.03	58.1 ± 0.9
B690	5.80 ± 0.12	3.69 ± 0.12	63.6 ± 2.5
B61/62	4.00 ± 0.21	2.69 ± 0.08	67.2 ± 4.1
IC132	5.52 ± 0.05	3.81 ± 0.02	69.0 ± 0.7
IC131	4.12 ± 0.07	3.84 ± 0.06	93.2 ± 2.1
NGC588	4.67 ± 0.17	3.74 ± 0.06	80.0 ± 3.2
IC142	4.14 ± 0.08	3.09 ± 0.13	74.6 ± 3.4
B691	7.40 ± 0.20	2.43 ± 0.04	32.8 ± 1.0
NGC592	5.43 ± 0.14	3.27 ± 0.08	60.2 ± 2.2
M33 (mJy):			
R < 7.5 kpc	2722 ± 60	478 ± 85	17.6 ± 3.1

Integrating the thermal maps in rings around the galaxy center out to a radius of 7.5 kpc, we obtain the total thermal flux densities and thermal fractions at 3.6 and 20 cm (see Tables 4.1 and 4.2). These Tables also give the thermal flux densities and thermal fractions at the position of the 11 brightest HII regions (the coordinates of these HII complexes are listed in Chapter 2).

4.7 Distribution of nonthermal emission

Subtracting the maps of the thermal emission from the observed maps at each wavelength, maps of the nonthermal emission are obtained (Figs. 4.4 and 4.5). The latter maps exhibit diffuse emission extending to large radii. They also show strong features in the spiral arms and central region of the galaxy. The strongest nonthermal emission emerges from the HII complexes NGC604 and NGC595 at both 3.6 and 20 cm. Typically, HII complexes host tens of young O/B stars, many of which end as supernovae whose remnants contribute to a mixed (thermal and nonthermal), flat spectrum of the total radio emission from these regions (as discovered in NGC 604 and NGC 595, Dodorico 1978; Gordon et al. 1993; Yang et al. 1996). Supernova remnants with central energy sources in the form of young pulsars (Crab-like remnants) also have flat nonthermal spectra. Note that using a lower electron temperature decreases the thermal fraction and increases the nonthermal contribution (see Eq. 4.10). For example, the thermal fraction decreases from $\simeq 76\%$ to 57% and from $\simeq 68\%$ to 52% in the position of NGC604 and NGC595, respectively, using $T_e = 7000$ K.

Another strong feature in the 20 cm nonthermal map belongs to the active star-forming region in the central southern arm IS. This confirms our previous conclusion about the

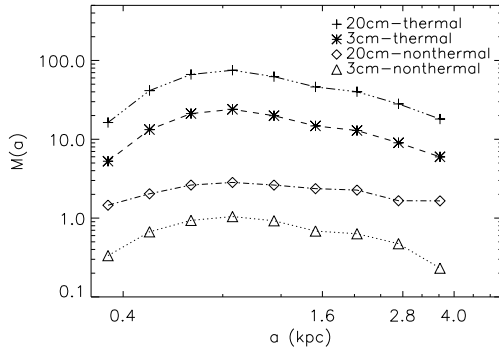


Figure 4.6: The wavelet spectra of the 3.6 and 20 cm thermal and nonthermal emission at $90''$ resolution. The data points correspond to the scales 0.36, 0.48, 0.64, 0.86, 1.14, 1.52, 2.03, 2.72, 3.63 kpc.

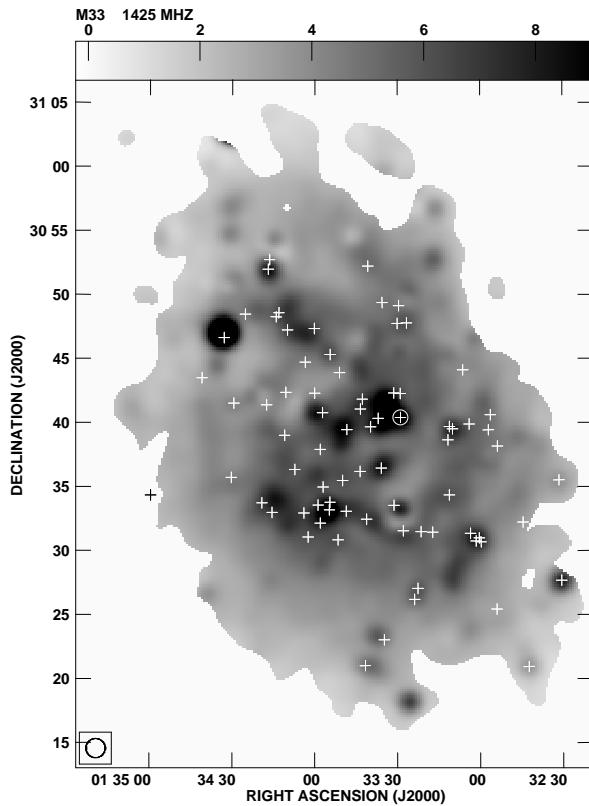


Figure 4.7: The same 20 cm nonthermal map as shown in Fig. 4.5 with supernova remnants (crosses) superimposed. The supernova remnants with a signal-to-noise ratio of larger than 0.7 were selected from the catalogue of Gordon et al. (1998). The circle shows an HII region with nonthermal spectral index (Gordon et al. 1999).

spatial coupling of the nonthermal emission with the starforming regions (Chapter 2). There are also other point-like sources which are not resolved. Looking at the 3.6 cm map, the giant HII region IC133 (RA = $1^h 33^m 15.3^s$ and DEC = $30^\circ 53' 19.7''$) is also strong, but not at 20 cm. Hosting the two strongest optically thick HII regions (Johnson et al. 2001), IC133 has an inverted spectrum. The appearance of this source in the 3.6 cm nonthermal map is due to the assumption that the free-free emission is optically thin (equivalent to the thermal spectral index of 0.1 when $S_{th} \sim \nu^{-0.1}$). Furthermore, IC133 probably contains some nonthermal emission as Schulman & Bregman (1995) found it associated with a bright X-ray source located in a hole in the HI layer of the galaxy, indicating energetic stellar winds and supernovae from massive stars.

Tabatabaei et al. (2007a) discussed the wavelet spectrum of the total radio continuum maps. Here, we present the wavelet energy of the thermal and nonthermal emission at different scales. Fig. 4.6 shows that the wavelet spectrum of the nonthermal emission is smoother than that of the thermal emission at both wavelengths. Furthermore, the distribution of the nonthermal wavelet energy is smoother at 20 cm than at 3.6 cm. Scales smaller than the width of the spiral arms ($\simeq 400''$ or 1.6 kpc) and larger than the size of the giant starforming regions ($\simeq 100''$ or 0.4 kpc) at 20 cm are not as prominent as those at 3.6 cm, where the synchrotron photons have higher energies. In fact the synchrotron emission distribution reflects the combined distribution of the interstellar magnetic field and the cosmic ray electrons. Hence, assuming that the distribution of the interstellar magnetic field is the same at both wavelengths, one can conclude: the higher the energy of CRs, the more dominant the localized structures (which can be linked to the cosmic ray ‘sources’ e.g. supernova remnants). This is expected as energy losses of CR electrons increase with electron energy and field strength. Studying propagation effects with self-consistent Galactic wind simulations, Breitschwerdt et al. (2002) predicted a similar energy-dependence for the CR nucleon distribution in our Galaxy. They expect that the high energy (TeV) γ -rays from CR sources dominate the diffuse γ -ray emission, while the Galactic γ -ray observations in the GeV range (with EGRET and COS-B) have shown a roughly uniform distribution of the γ -ray emissivity in the Galactic plane.

The dominant scales of the wavelet spectra of the thermal (at 3.6 and 20 cm) and the 3.6 cm nonthermal emission are the same, indicating that the distribution of the cosmic ray sources is similar to that of the thermal sources. At scales larger than $a = 214''$ (0.86 kpc), the 3.6 cm nonthermal spectrum decreases twice as fast as the 20 cm nonthermal spectrum. The smaller energy losses of the CR electrons with lower energies (at 20 cm) than of those with higher energies (at 3.6 cm) may cause a smoother distribution of the emission at all scales. This indicates that besides the CR sources embedded in the star-forming regions, there is another component of the synchrotron emission in the form of a diffuse disk or a galactic halo that is better visible at 20 cm than 3.6 cm. This could be verified by multiwavelength observations of edge-on galaxies at resolutions higher than those of the existing data.

Fig. 4.7 shows the the supernova remnants from Gordon et al. (1998) superimposed on the nonthermal 20 cm map. There is general coincidence between nonthermal features and supernova remnants, the powerful sources of the relativistic electrons. Gordon et al. (1999) diagnosed 17 supernova remnants embedded in HII regions. They also found some 30 HII regions with nonthermal radio components of which it was not clear whether they belong to these regions or were external radio sources. The circle in Fig. 4.7 shows the position of the strongest ($S_{20} = 7.0 \pm 0.2$ mJy, $\alpha \simeq 0.2$) HII region with nonthermal emission. As this HII region is not resolved in our thermal maps with $90''$ resolution, it is not listed amongst the bright HII regions in Tables 4.1 and 4.2.

4.8 Nonthermal spectral index

From the nonthermal radio fluxes at 3.6 and 20 cm, we obtained the spectral index of the nonthermal emission which was only computed for pixels with flux densities of at least three times the rms noise σ at both frequencies. Fig. 4.8 shows that the nonthermal

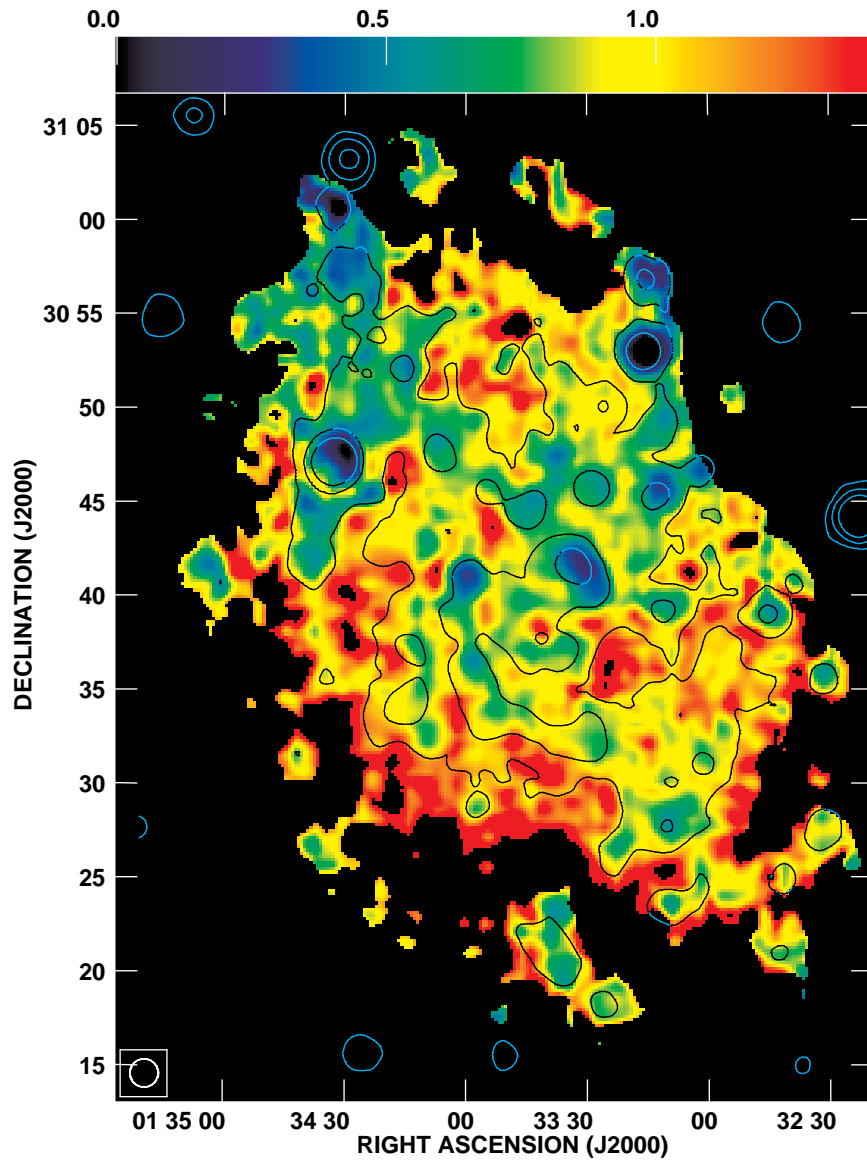


Figure 4.8: Nonthermal spectral index (α_n) map obtained from the nonthermal radio fluxes at 3.6 and 20 cm. The spiral arms are indicated by contours of the total radio emission at 3.6 cm superimposed. Contour levels are 1.5, 4.5, and 12 mJy/beam. The angular resolution is $90''$ with a grid size of $10''$.

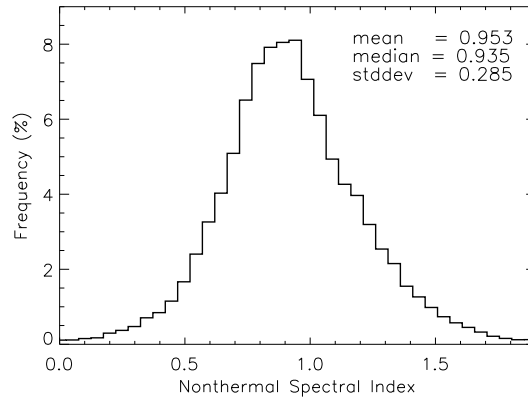


Figure 4.9: A histogram of the nonthermal spectral index map. The number of bins used for this plot is 50.

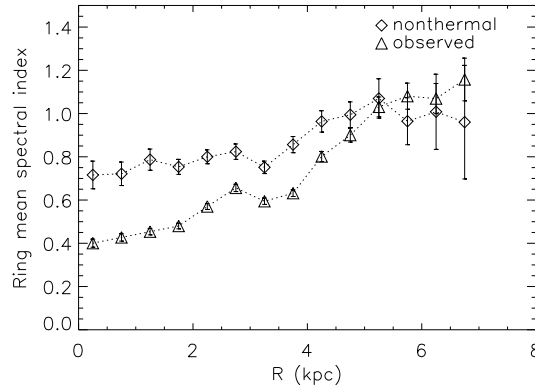


Figure 4.10: Mean nonthermal spectral index in rings of 0.5 kpc width in the galactic plane versus galactocentric radius. The total (observed) spectral index is also shown for comparison. The minima at $3 < R < 4$ kpc is due to the HII complex NGC604.

spectral index, α_n , has a clumpy distribution. Note that the fainter regions have steeper spectra. The most probable value of α_n distributed across the galaxy is 0.95 (Fig. 4.9). This is in perfect agreement with the mean nonthermal spectral index derived by Klein (1988) for a sample of galaxies. In the star-forming regions, the nonthermal spectrum is relatively flat with an average value of α_n of 0.6 ± 0.1 , the typical spectral index of supernova remnants, but α_n increases to 1.2 ± 0.2 in the interarm regions and outer parts of the galaxy. This indicates energy losses of the relativistic electrons while they diffuse away from their origin in star-forming regions towards the interarm regions and the outer parts of the galaxy. For the first time, a nonthermal spectral index map can be used to achieve more realistic models for the propagation of CR electrons.

Integration of the nonthermal intensity in rings of 0.5 kpc in the galactic plane yields the mean nonthermal spectral index in each ring. The radial variation of the ring mean spectral index is shown in Fig. 4.10, where the ring mean spectral index of the total radio continuum emission is also plotted for comparison. Up to $R \simeq 4$ kpc, there is no increas-

ing trend for the nonthermal spectral index with radius as for the total spectral index. Here the ring mean nonthermal spectral index varies between 0.65 and 0.9, indicating that CRs are injected by sources related to massive stars, and under leakage and synchrotron losses (Biermann 1995). Towards the outer parts of the galaxy the nonthermal and total spectral indices converge, confirming that the total radio continuum emission is mostly nonthermal at $R > 4.5$ kpc. This region corresponds to the synchrotron and inverse Compton loss dominated regime as $\alpha_n \simeq 1$ on the average (Biermann 1995). Note that changing the electron temperature from 10,000 K to 7000 K changes α_n from $\simeq 0.18$ to 0.31 and from $\simeq 0.01$ to 0.03 for NGC604 and NGC595, respectively, and hence does not make their flat nonthermal spectra much steeper. This may indicate a strong free-free energy-loss in these HII complexes.

It seems that the nonthermal emission have a steeper spectrum from the southern than the northern half of the galaxy, indicating a more important role of synchrotron and leakage losses in the southern half.

4.9 Discussion

4.9.1 Comparison with the standard method

In this section, we first obtain the distribution of the thermal and nonthermal emission assuming that the nonthermal spectral index is constant across the galaxy (standard method). Then we compare the results from the two methods.

Because the thermal emission is weak in the outer parts of the galaxy, one may consider the total spectral index from these parts as the pure nonthermal spectral index³, α_n (e.g. Berkhuijsen et al. 2003). The total spectral index map of M33 gives $\alpha_n = 1.0 \pm 0.1$ (see Fig. 2.9). For a total spectral index, α , obtained from the observed flux densities at frequencies ν_1 and ν_2 and the constant value of α_n , the thermal fraction at frequency ν_1 is given by

$$F_{th}^{\nu_1} = \left[\left(\frac{\nu_2}{\nu_1} \right)^{-\alpha} - \left(\frac{\nu_2}{\nu_1} \right)^{-\alpha_n} \right] / \left[\left(\frac{\nu_2}{\nu_1} \right)^{-0.1} - \left(\frac{\nu_2}{\nu_1} \right)^{-\alpha_n} \right], \quad (4.11)$$

(Klein et al. 1984). Then the thermal flux density at frequency ν_1 , $S_{th}^{\nu_1}$, is obtained from

$$S_{th}^{\nu_1} = S^{\nu_1} \times F_{th}^{\nu_1}, \quad (4.12)$$

and the nonthermal flux density at frequency ν_1 , $S_n^{\nu_1}$ is

$$S_n^{\nu_1} = S^{\nu_1} - S_{th}^{\nu_1}. \quad (4.13)$$

Using the data at 3.6 and 20 cm in the above formulae, the corresponding thermal and nonthermal maps are derived; those at 20 cm are shown in Fig. 4.11. The main difference between the standard and our new method (Fig. 4.5) concerns the distribution of the nonthermal emission, while the thermal maps show almost the same structures. The nonthermal emission from the standard method is weaker than that from the new method

³This is confirmed by the new method, as mentioned in Sect. 4.8.

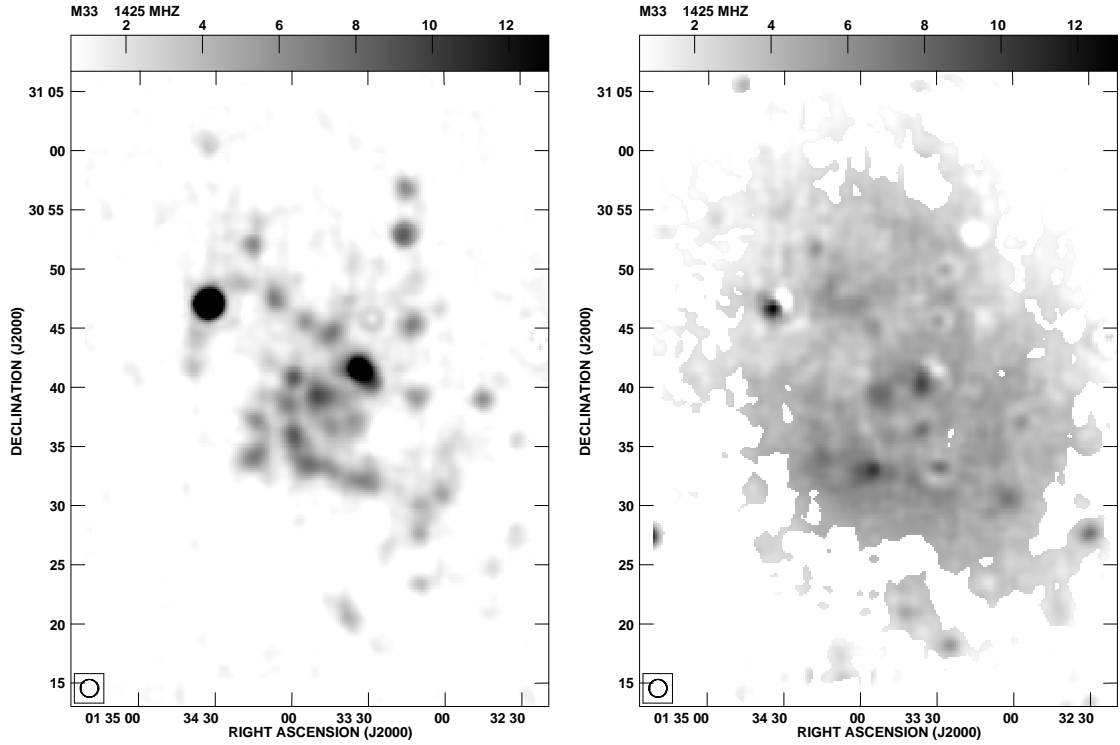


Figure 4.11: Thermal and nonthermal 20 cm maps obtained from the standard method. The grey-scale gives the flux density in mJy/beam. The angular resolution is $90''$ with a grid size of $10''$.

and hardly shows emission from star-forming regions in the arms. Often it is even weaker in the arms than in between the arms and in the outer parts of the galaxy.

In contrast to what is assumed in the standard method, large variations of the nonthermal spectral index are found across M33 by the new method (Fig. 4.8). We interpret this as clear evidence that CR electrons suffer energy losses diffusing away from their places of origin in the arms towards interarm and outer regions.

Table 4.3 lists the thermal fractions of the 11 bright HII regions and of M33 (from the integrated flux density maps up to $R = 7.5$ kpc) at 3.6 cm obtained from both methods. The thermal fractions of all the sources are larger when obtained from the standard method than from the new method. Some even exceed 100%, causing very weak or negative nonthermal fluxes. The thermal fraction of M33 from the standard method is $23\% \pm 14\%$ higher than that from the new method. In Chapter 2, we used the standard method with $\alpha_n = 1.0 \pm 0.1$ to estimate the thermal fraction from the integrated spectrum, based on data at 35.6, 21.1, 17.4, 11.1, 6.3, 6.2, 3.6, and 2.8 cm, as 0.49 ± 0.15 which agrees with the value 0.51 ± 0.04 obtained from the new method. This indicates that the assumption of a constant nonthermal spectral index is reasonable to estimate mean values for global studies, when the integrated spectrum is used.

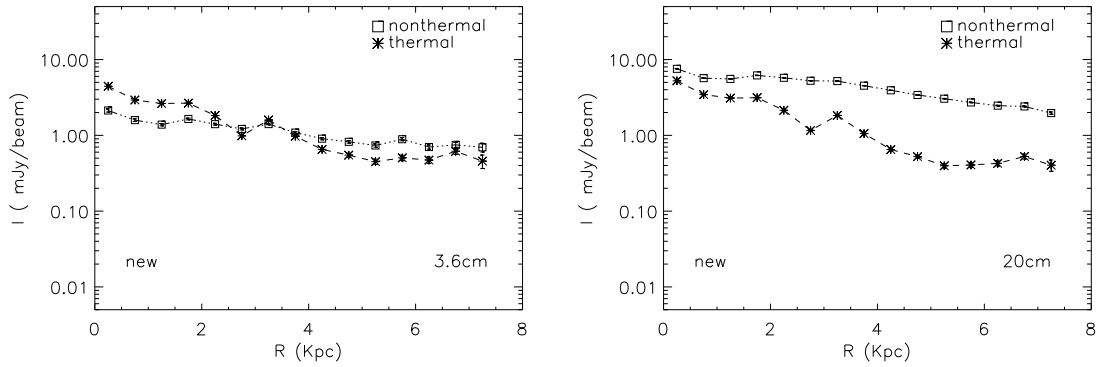


Figure 4.12: Radial profiles of the thermal and nonthermal intensities at 3 cm (left) and 20 cm (right) obtained from the *new* separation method. The thermal intensities show a bump at $3 < R < 4$ kpc which is due to the HII complex NGC604.

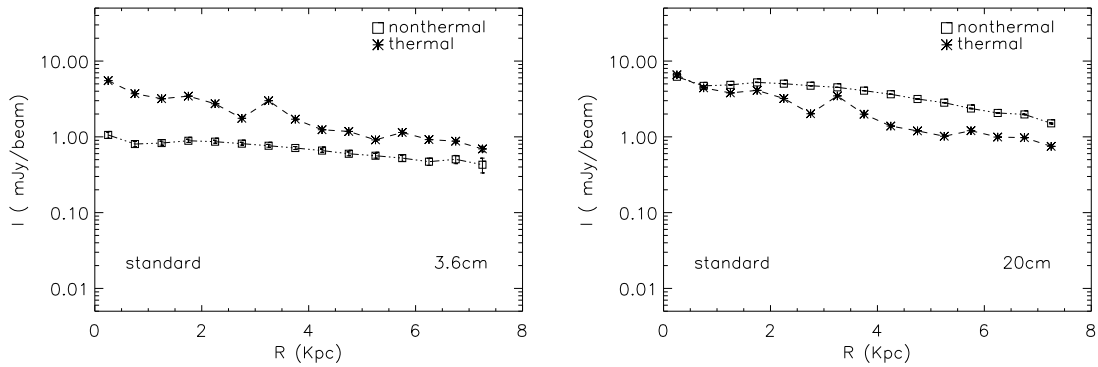


Figure 4.13: Radial profiles of the thermal and nonthermal intensities at 3 cm (left) and 20 cm (right) obtained from the *standard* separation method. The thermal intensities show a bump at $3 < R < 4$ kpc which is due to the HII complex NGC604.

4.9.2 Radial scale lengths

Fig. 4.12 shows the exponential distributions of the thermal and nonthermal intensities at 3.6 and 20 cm with galactocentric radius. The radial profiles of the nonthermal emission are smoother and flatter than those of the thermal emission at both wavelengths. The fluctuations in the thermal profiles at $2 < R < 4$ kpc cause similar fluctuations observed in the profile of the total emission (presented in Tabatabaei et al. 2007c).

The same profiles obtained from the standard method are shown in Fig. 4.13 for comparison. The nonthermal radial profiles are slightly smoother (especially at 3.6 cm) than those from the new method, caused by the assumption of a constant nonthermal spectral index. Although the thermal radial profiles exhibit the same variations as those in Fig. 4.12, the over-estimation of the thermal emission from the standard method is obvious.

The exponential scale length, l , is obtained by fitting an exponential function of the form $I(R) = I_0 \exp(-R/l)$, where I_0 is the intensity at $R=0$. Table 4.4 shows the

Table 4.3: Thermal fractions at 3.6 cm obtained from the new and standard methods. It is shown that the thermal fraction obtained from the standard method is over-estimated especially for the HII complexes.

Object	$\alpha_{(3.6,20)}$	F_{th} (new method) %	F_{th} (standard method) %
NGC604	0.12 ± 0.01	76.4 ± 0.3	99.2 ± 0.4
NGC595	0.07 ± 0.03	67.6 ± 1.3	101.6 ± 1.4
IC133	-0.30 ± 0.03	29.3 ± 0.8	106.5 ± 1.6
B690	0.14 ± 0.05	68.9 ± 3.9	99.1 ± 3.6
B61/62	0.04 ± 0.08	60.2 ± 3.7	104.3 ± 4.2
IC132	0.07 ± 0.02	66.5 ± 1.0	101.6 ± 1.5
IC131	-0.06 ± 0.03	71.0 ± 2.2	107.2 ± 2.4
NGC588	0.00 ± 0.05	69.8 ± 2.6	103.1 ± 2.9
IC142	0.09 ± 0.04	77.8 ± 4.6	96.9 ± 3.6
B691	0.27 ± 0.05	51.1 ± 2.6	93.0 ± 3.4
NGC592	0.13 ± 0.04	64.5 ± 2.6	97.9 ± 2.8
M33 :			
R < 7.5 kpc	0.72 ± 0.04	51.4 ± 10.6	63.2 ± 13.4

exponential scale lengths of the thermal emission, l_{th} , and nonthermal emission, l_n , from both methods. Generally, the scale lengths of the nonthermal emission are larger than those of the thermal emission (by a factor of $\simeq 2$). In Sect. 4.7, we show that the CR sources follow the distribution of the thermal sources, i.e. star-forming regions. Hence, the radial distribution of the CR sources decreases faster than that of the synchrotron emission. This is a direct observational result indicating diffusion of the cosmic rays from their places of origin to larger distances.

Using the standard method, Buczilowski (1988) determined the scale length of the 6.3 cm thermal and nonthermal emission as 1.8 ± 0.2 kpc and 4.2 ± 0.3 kpc, respectively. These scale lengths are smaller than those obtained here (even smaller than those obtained from the standard method), although the ratio of the nonthermal to thermal scale lengths is the same ($\simeq 2$). Due to the low signal-to-noise ratio of the old 6.3 cm Effelsberg receiver used by Buczilowski (1988) much of the diffuse emission in the outer parts of the galaxy had been missed, leading to steeper radial profiles and smaller scale lengths. For the same reason also the scale lengths derived by Berkhuijsen & Klein (1985) are too small. They obtained the distribution of the thermal emission at 6.2 cm from a catalogue of HII regions in H α (Boulesteix et al. 1974) where the diffuse emission was not completely included.

In case of equipartition between the magnetic field and CRs, the scale length of the CR electrons is given by $l_{cr} = l_n(3 + \alpha_n)/2$ and that of the magnetic field by $l_B = 2 l_{cr}$ (e.g. Klein et al. 1982). Taking $\alpha_n \simeq 1$, we obtain $l_{cr} \simeq 12$ kpc and $l_B \simeq 24$ kpc.

For NGC6946, Walsh et al. (2002) found a nonthermal scale length of $l_n \sim 4$ kpc which gives a smaller CR scale length of $l_{cr} \simeq 8$ kpc. Although NGC6946 is a Scd-type galaxy like M33, it is a starburst system and it hosts stronger star formation in its central region than M33. This may cause a steeper radial profile of the total intensity and consequently a smaller nonthermal (and cosmic ray) scale length than in M33.

Table 4.4: Exponential scale lengths of the thermal (l_{th}) and nonthermal (l_n) components of the radio continuum emission from M33 at 3.6 and 20 cm. Results from both methods (new and standard) are listed.

λ	l_{th} (kpc)	l_n (kpc)
new		
20 cm	2.4 ± 0.2	5.8 ± 0.5
3.6 cm	2.6 ± 0.2	6.1 ± 0.7
standard		
20 cm	3.5 ± 0.5	6.2 ± 0.7
3.6 cm	3.7 ± 0.5	8.9 ± 0.9

Table 4.5: North-South ratios of the integrated flux densities of the thermal, nonthermal, and total radio emission. Results from both methods (new and standard) are listed.

λ (cm)	S_{th}^N/S_{th}^S	S_n^N/S_n^S	S_T^N/S_T^S
new			
3.6	0.89 ± 0.05	1.15 ± 0.08	1.10 ± 0.08
20	0.86 ± 0.05	0.75 ± 0.07	0.82 ± 0.07
standard			
3.6	1.20 ± 0.07	0.67 ± 0.07	1.10 ± 0.08
20	1.14 ± 0.06	0.77 ± 0.08	0.82 ± 0.07

4.9.3 North–south asymmetry

From Figs. 4.4 and 4.5 it seems that the thermal emission is stronger in the southern than in the northern half of M33. To investigate this north-south (N-S) asymmetry, we obtain the integrated flux density of the thermal, nonthermal, and total emission in each half separately. Table 4.5 shows the results from both the new and the standard method. The thermal emission from the new method is slightly stronger in the southern than in the northern half of the galaxy at both wavelengths. This may be the reason for the higher Faraday depolarization found in the southern half than in the northern half (Tabatabaei et al. 2007c). In Chapter 5, we will discuss whether the asymmetry in the Faraday depolarization can be caused by this N-S asymmetry in the thermal emission distribution. Note that, from the standard method, the thermal emission in the southern half is weaker.

The nonthermal emission at 20 cm from the new method in the southern half is also stronger than in the northern half (in contrast to the 3.6 cm nonthermal emission). This is expected as the stronger supernova remnants are concentrated in the southern half especially in the arm IS, which produce stronger nonthermal emission at longer wavelengths. The existence of the strong optically thick HII regions (e.g. IC133) in the northern half of the galaxy also causes the different N-S ratios of the nonthermal emission at 3.6 cm.

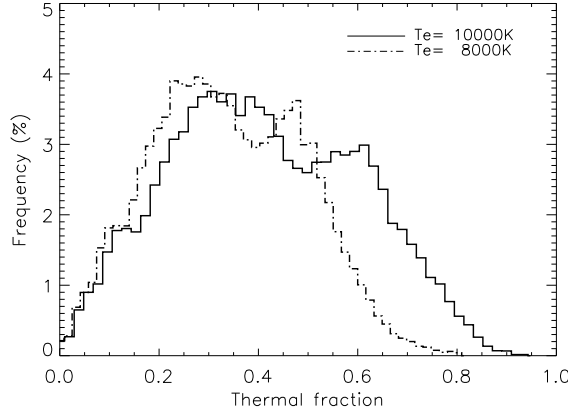


Figure 4.14: Distribution (histogram) of the thermal fraction at 3.6 cm in M33. The number of bins used for this histogram is 50.

4.9.4 Uncertainties

How do the assumptions of the new method of separating thermal and nonthermal emission influence the results? We take the thermal fraction (e.g. at 3.6 cm) as the final result and define U as the uncertainty in F_{th} when one of the assumptions changes,

$$U \equiv \frac{|F_{th} - F'_{th}|}{F_{th}}. \quad (4.14)$$

F_{th} and F'_{th} are the thermal fractions before and after changing an assumption, respectively.

One of the assumptions is the choice of effective extinction factor $f_d=0.33$ (non-uniform ionization). For a homogeneous distribution of dust and ionized gas, $f_d=0.5$, the average uncertainty in the thermal fraction at 3.6 cm is only $U = 2\%$ with a standard deviation of 1%.

Changing T_e from the adopted 10,000 K to 8000 K, the most probable uncertainty across the galaxy is $U = 17\%$ with a standard deviation of 3%. Fig. 4.14 shows that the thermal fraction decreases with decreasing electron temperature. Larger differences in the thermal fraction are found for regions with higher thermal emission like HII regions, and the influence of changing T_e is relatively small in diffuse regions with small F_{th} . Thus, we find that the uncertainty resulting from the new method is mainly determined by uncertainty of the electron temperature.

Another question is which method, the new method with its electron temperature assumption or the standard method with its constant nonthermal spectral index assumption, faces larger uncertainty in the thermal fraction. For this comparison, we first obtain the nonthermal spectral indices for different electron temperatures. For $T_e=10,000$ K the most probable nonthermal spectral index is 0.9, while it is 0.8 for $T_e=8000$ K. Then, from the standard method, we calculate the thermal fractions assuming $\alpha_n=0.9$ and 0.8, respectively, which leads to an uncertainty of $U = 40\%$, much larger than that determined from our method (17%). We conclude that the thermal fraction is more sensitive to vari-

Table 4.6: Average thermal fraction of M33 at 3.6 cm for different assumptions. The uncertainty U of each assumption is calculated with respect to the case $T_e = 10,000$ K and $f_d = 0.33$.

T_e (K)	&	f_d	F_{th} (%)	U (%)
10,000	&	0.33	51	(...)
10,000	&	0.50	54	5
8000	&	0.33	41	20
8000	&	0.50	43	16

ations of the nonthermal spectral index in the standard method than to variations of the electron temperature in the new method.

Table 4.6 shows the thermal fractions obtained from the thermal and total flux densities of M33 (integrated for $R < 7.5$ kpc) for different combinations of the assumptions of T_e and f_d .

4.9.5 Thermal/nonthermal radio–IR correlation

The correlation between the IR and total radio continuum emission was presented at different scales of emitting structures in Chapter 2. Assuming that the radio emission is mostly thermal at 3.6 cm and mostly nonthermal at 20 cm, we concluded that the warm dust–thermal radio correlation is stronger than the cold dust–nonthermal radio correlation. However, a more precise conclusion requires comparison with the thermal and nonthermal radio emission, separately.

We obtained the wavelet cross-correlations between the MIPS IR maps and the 3.6 cm thermal and nonthermal maps separated from the new method. The results not only confirm the stronger warm dust–thermal radio than the cold dust–nonthermal radio correlation, but also show a stronger warm dust–nonthermal radio than the cold dust–nonthermal radio correlation at some scales (Fig. 4.15). It is also found that the cold dust has a better correlation with the thermal than the nonthermal emission. This is in contradiction with what Hoernes et al. (1998) found in M31. This could be due to a) the spatial correlation of the nonthermal emission with the thermal emission e.g. because of a stronger magnetic field or cosmic rays with higher density in the location of the star forming regions and b) the larger role of UV photons from O/B stars in heating the cold dust in M33 than in M31 at least up to the scales of 3.5 kpc, as discussed in Chapter 2.

Another interesting point is that the IR correlations with the ‘nonthermal’ emission is better at a medium scale of $\sim 200'' - 500''$ (or 0.8 kpc–2 kpc, including the size of the giant molecular clouds and star forming regions, spiral arms, and the central extended region of M33), whilst the IR correlation with the ‘thermal’ radio emission increases with scale, monotonically.

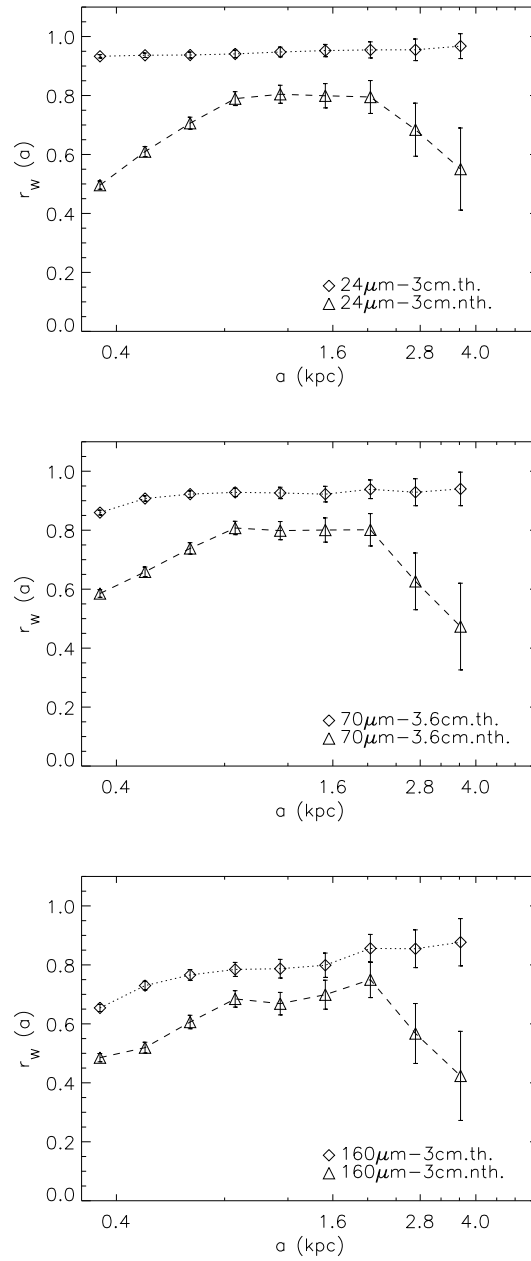


Figure 4.15: The cross-correlation between the thermal/nonthermal components of the 3.6 cm and $24\mu\text{m}$ (top), $70\mu\text{m}$ (middle), and $160\mu\text{m}$ (bottom) images at $90''$ resolution.

4.9.6 Spinning dust emission

It was supposed that the radio continuum emission consists of the thermal and nonthermal components. On the other hand, it is claimed that spinning dust also emits radio continuum radiation with a peak at around 20 GHz (e.g. Watson et al. 2005) and with a possible contamination at 3.6 cm (8.35 GHz). Then a question is how much of the total emission from M33 at 3.6 cm is provided by spinning dust. We investigated the contribution of the spinning dust emission from M33 by using the nonthermal spectral index obtained from the integrated nonthermal flux densities at 20 and 6.2 cm, $\alpha_n (\simeq 0.8)$. Assuming that this nonthermal spectral index is constant between 20 and 3.6 cm, the integrated nonthermal flux density at 3.6 cm, $S_n(8.35)$, is obtained by:

$$S_n(8.35) = S_n(1.42) (8.35/1.42)^{-\alpha_n}. \quad (4.15)$$

The total flux density of the spinning dust emission, S_{dust} can be obtained by subtracting $S_n(8.35)$ from the integrated nonthermal flux density obtained from the new method, $S'_n(8.35)$:

$$S_{\text{dust}} = S'_n(8.35) - S_n(8.35) \quad (4.16)$$

Substituting the corresponding values in (6.1) and (6.2) and taking the errors into account, we derive $S_{\text{dust}} = (370 \pm 60) - (463 \pm 73)$ mJy, indicating an unimportant (if any) contribution of the spinning dust in the total radio continuum emission from M33 at 3.6 cm. In case of a steeper nonthermal spectrum between 6.2 and 3.6 cm, e.g. taking $\alpha_n = 1$, we receive $S_{\text{dust}} = (370 \pm 60) - (296 \pm 73)$ mJy, which is also negligible within the errors.

4.9.7 Comparison with the 49 cm data

The HII complexes NGC604 and NGC595 are strong features appearing in our nonthermal maps. This seems to contradict to what is known from HII regions as ‘thermal nebulae’. Although the fact that these sources are not single HII regions but a collection of about 200 O/B stars in different evolutionary phases answers the question, it would be interesting to check these sources at longer wavelengths, where the thermal emission is much weaker than the nonthermal emission. A map of M33 at 612 MHz (49 cm) observed with the Westerbork Synthesis Radio Telescope (WSRT) interferometer shows that not only NGC604 and NGC595 are strongest sources but also other similarities with our nonthermal maps can be confirmed (Fig. 4.16). Note that we could not use this data in our separation because of its lack of diffuse emission (due to the missing spacings problem of interferometry).

4.10 Summary and conclusions

We have developed a new method to separate the thermal and nonthermal radio emission from a galaxy. We used the highly resolved and sensitive Spitzer 70 and 160 μm data of M33 to correct the $\text{H}\alpha$ map of Hoopes & Walterbos (2000) for extinction. From this map, we calculated the thermal (free-free) emission at 3.6 and 20 cm and obtained maps

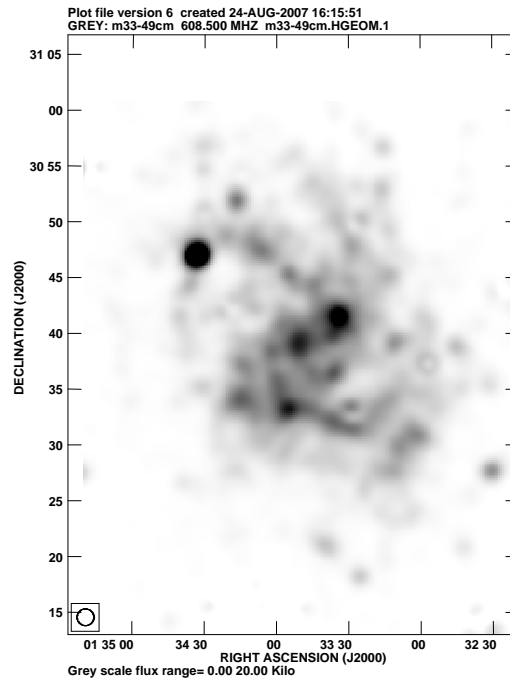


Figure 4.16: The WSRT 49 cm image of M33 at $90''$ resolution.

of the nonthermal emission as well as a map of the nonthermal spectral index in M33. The distribution of the nonthermal spectral index greatly helps to understand the origin and propagation of cosmic ray electrons in a galaxy. In brief, the results and conclusions are as follows:

- The distribution of the dust extinction is similar to that of the $160 \mu\text{m}$ emission. The mean extinction in rings in the galactic plane exhibits a shallow radial gradient.
- With a nonthermal fraction of about 30%–60% at 3.6 cm, the spiral arms and star-forming regions have a considerable contribution to the nonthermal emission. This contribution is negligible in the nonthermal maps obtained from the standard separation method. The radial profiles of the surface brightnesses and the wavelet spectra show that the distribution of the nonthermal emission from the standard method is smoother than that derived from the new method. This is caused by the assumption of a constant nonthermal spectral index in the standard method.
- The nonthermal emission from the new method is still more smoothly distributed than the thermal emission. The exponential scale lengths of the nonthermal emission are more than twice as large as those of the thermal emission.
- The standard method over-estimates the thermal fraction, especially at the position of giant HII regions. For galactocentric radius $R < 7.5$ kpc, the thermal fractions at 3.6 cm are $51 \pm 11\%$ and $63 \pm 13\%$ from the new and standard methods, respectively.

- For the first time, we derived a map of the nonthermal spectral index. In the star-forming regions, the nonthermal spectrum is relatively flat with an average value of α_n of 0.6 ± 0.1 , the typical spectral index of supernova remnants, but α_n increases to 1.2 ± 0.2 in the interarm regions and outer parts of the galaxy. This shows that the relativistic electrons lose energy when diffusing from their origin in star-forming regions towards interarm regions and the outer parts of the galaxy. The mean spectral index of the nonthermal emission becomes equal to that of the total emission at $R \simeq 4.5$ kpc. This indicates that the total radio emission is mostly nonthermal at $R > 4.5$ kpc in M33, where the spectral index is dominated by synchrotron and inverse Compton loss processes.
- The wavelet transform of the nonthermal maps revealed that the nonthermal emission is smoother at 20 cm than at 3.6 cm, indicating that high energy CR electrons experience more energy losses, and hence diffuse less than low energy CR electrons.
- Assuming equipartition between the magnetic field and CRs, the scale length of the CR electrons and of the magnetic field estimated are $l_{cr} \simeq 12$ kpc and $l_B \simeq 24$ kpc in this galaxy.
- Generally, the *integrated* results from the two methods match with each other within the errors, indicating that the assumption of a constant nonthermal spectral index is a proper approximation for ‘global’ studies.
- At scales smaller than 4 kpc, not only the warm dust but also the cold dust emission is better correlated with the thermal than with the nonthermal radio emission, indicating the important role of UV photons in heating the dust at these scales.

5 Magnetic fields in M33

5.1 Introduction

Magnetic fields in galaxies can be traced by radio polarization measurements. Synchrotron radio continuum emission in a uniform magnetic field is about 70% linearly polarized intrinsically. Turbulent magnetic fields, depolarization effects and telescope beam smearing reduce the observable degree of polarization. The linearly polarized intensity gives information about the magnetic field component in the plane of the sky, while Faraday rotation measurements enable us to determine the magnetic field component along the line of sight.

M33 with its large angular size and medium inclination of 56° allows determination of the magnetic field components both parallel and perpendicular to the line of sight equally well. Our high-resolution and -sensitivity polarization data at 3.6, 6.2, and 20 cm enable us to study rotation measure (RM), magnetic field structure and strength, and depolarization effects in detail.

Previous RM studies of M33 based on polarization observations at 11.1 and 21.1 cm (Beck 1979) suggested a bisymmetric large scale magnetic field structure in the disk of M33. Buczylowski & Beck (1991) confirmed the presence of this bisymmetric field using two further polarization maps at 6.3 and 17.4 cm. However, this result might be affected by a lack of polarization and RM in the southern half of M33, due to the low-sensitivity observations.

Tabatabaei et al. (2007c) found a north-south asymmetry in the polarization distribution that is wavelength-dependent, indicating a possible north-south asymmetry in the Faraday depolarization. Investigating this possibility, requires a knowledge about the distribution of RM and turbulent magnetic field in the galaxy.

We obtain the intrinsic RM map with a spatial resolution higher than before ($3'$ or 0.7 kpc) and probe its mean value in rings in the galactic plane in Sect. 5.2. We also determine the nonthermal degree of polarization using the new nonthermal maps (Sect. 5.3). The magnetic field structure and strengths are discussed in Sect. 5.4. We derive a map for the observed depolarization and discuss possible depolarization sources in Sect. 5.5.

5.2 Rotation measures

As the linearly polarized radio waves propagate in a magneto-ionic medium, their polarization vector is systematically rotated. The amount of this rotation depends on the wavelength of the radio emission, the strength of the magnetic field along the line of sight

(B_{\parallel}), and the number of thermal electrons along the line of sight (n_e):

$$\frac{\Delta\phi}{\text{rad}} = 0.81 \left(\frac{\lambda}{\text{m}}\right)^2 \int_0^{L/\text{pc}} \left(\frac{B_{\parallel}}{\mu\text{G}}\right) \left(\frac{n_e}{\text{cm}^{-3}}\right) d\left(\frac{l'}{\text{pc}}\right), \quad (5.1)$$

with L the path length through the magneto-ionic medium. Hence, the measured polarization angle ($\phi = \frac{1}{2}\tan^{-1}\frac{U}{Q}$) differs from the intrinsic polarization angle (ϕ_i) as

$$\phi - \phi_i = \Delta\phi \equiv \lambda^2 \text{RM}. \quad (5.2)$$

Practically, RM can be obtained from measurements of the polarization angles at two wavelengths:

$$\frac{\text{RM}}{\text{rad m}^{-2}} = \frac{(\phi_1/\text{rad}) - (\phi_2/\text{rad})}{\left(\frac{\lambda_1}{\text{m}}\right)^2 - \left(\frac{\lambda_2}{\text{m}}\right)^2}. \quad (5.3)$$

In this definition, the unknown intrinsic polarization angle of the source (or sources along the line of sight) cancels. Positive RM indicates that B_{\parallel} points towards us.

Using the linearly polarization data of M33, we first obtained the distribution of RM between 3.6 and 20 cm (Fig. 5.1, left panel), showing smooth variations in the northern half of the galaxy. However, lots of RM variations and flips in the direction of B_{\parallel} exist in the southern half of the galaxy, which resist by adding $\pm n \cdot 73 \text{ rad m}^{-2}$ ambiguity. As presented in Chapter 2, weak polarized emission in the southern half at 20 cm could be linked to these RM variations. Between 3.6 and 6.2 cm, RM varies smoother than that between 3.6 and 20 cm in the south of the galaxy (Fig. 5.1, right panel). Usually, only part of RM is caused in interstellar medium of external galaxies (RM_i), the rest is due to the Galactic foreground medium (RM_{fg}) and $\text{RM} = \text{RM}_i + \text{RM}_{\text{fg}}$. The foreground rotation measure of M33 is mainly caused by the extended Galactic magnetic bubble region *A* (Simard-Normandin & Kronberg 1980). Assuming that the intrinsic contributions of the extragalactic sources 3C41, 3C42, and 3C48 themselves cancel out and the intergalactic contribution is negligible, Broten et al. (1988) and Tabara & Inoue (1980) found a rotation measure of $-57 \pm 10 \text{ rad m}^{-2}$. For the polarized sources in the $2^\circ \times 2^\circ$ M33 field, Buczilowski & Beck (1991) found a foreground RM of $-55 \pm 10 \text{ rad m}^{-2}$ (about the same value was obtained by Johnston-Hollitt et al. 2004). In the following we use this value as it is consistent with our measurements as well. Figure. 5.2 shows RM_i between 3.6 and 6.2 cm which varies in a range including both positive and negative values. Comparing the RM_i map with the overlaid contours of PI^1 , an agreement between the ordered magnetic field in the plane of the sky and the regular magnetic field in the line of sight is indicated in the north and along the minor axis. This is better visible in the magnetic filament in the north-west of M33 (see Chapter. 2), where RM_i shows small variation within the PI contours. This indicates that the strong ordered magnetic field in this region is mainly regular. The RM_i map also indicates that the magnetic field is directed towards us on the western minor axis, but has an opposite direction on the eastern part. Furthermore, large RM values on the minor axis indicate that B_{\parallel} is strong in these regions. Sign variations of the RM_i are more frequent in the southern than the northern

¹Note that PI is related to B_{\perp} which is a combination of both anisotropic (compressed or sheared random field) and regular fields in the sky plane. RM_i is related to B_{\parallel} that is regular field along the line of sight.

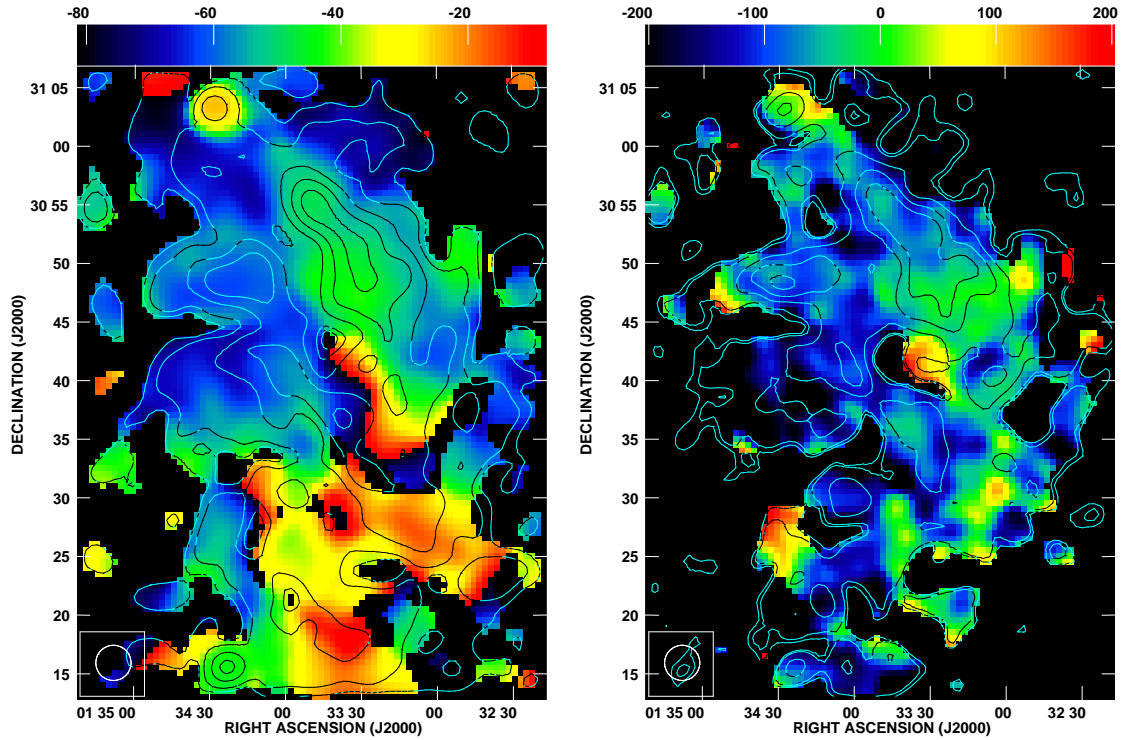


Figure 5.1: *Left*: observed rotation measure map of M33 between 3.6 and 20 cm with contours of 3.6 cm polarized intensity. Contour levels are 0.1, 0.2, 0.4, 0.6, 0.8 mJy/beam. *Right*: observed rotation measure map of M33 between 3.6 and 6.2 cm with contours of 6.2 cm polarized intensity. Contour levels are 0.3, 0.4, 0.8, 1.2, 1.6 mJy/beam.

half of the galaxy, where there is no correlation with PI. This indicates that the regular magnetic field is less confined to the disk in the south than in the north of M33.

Among the three brightest HII complexes at 3.6 cm (NGC604, NGC595, and IC133, see Chapter 2), the rotation measure is highest at the position of NGC595, $RA = 1^h 33^m 32.4^s$ & $DEC = 30^\circ 41' 50.0''$. This means that the electron density n_e , and/or the magnetic field component in the line of sight B_{\parallel} is larger at the position of NGC595 than in the two other HII complexes.

Figure. 5.3 shows the azimuthal variations of RM_i in rings. Starting from a distance of 1 kpc from the center, the rotation measure was averaged in the galactic plane in 6 rings of 1 kpc radial width over sectors of 10° width. The azimuthal angles shown in this figure were corrected for inclination of the galaxy, $\theta_0 = \arctan(\tan\theta/\cos i)$, with θ the azimuthal angle on the sky and i the inclination of the galactic plane against a face-on view. $\theta_0 = 0^\circ$ and 180° correspond to the northern and southern major axis, 90° and 270° to the eastern and western minor axis. As shown, the RM_i variations in this galaxy is very disordered and do not follow a periodic pattern (Sect. 5.4) in general. The only periodicity is found in the ring 2-3 kpc in which RM_i is asymmetric with its minimum and maximum on the eastern and western minor axis.

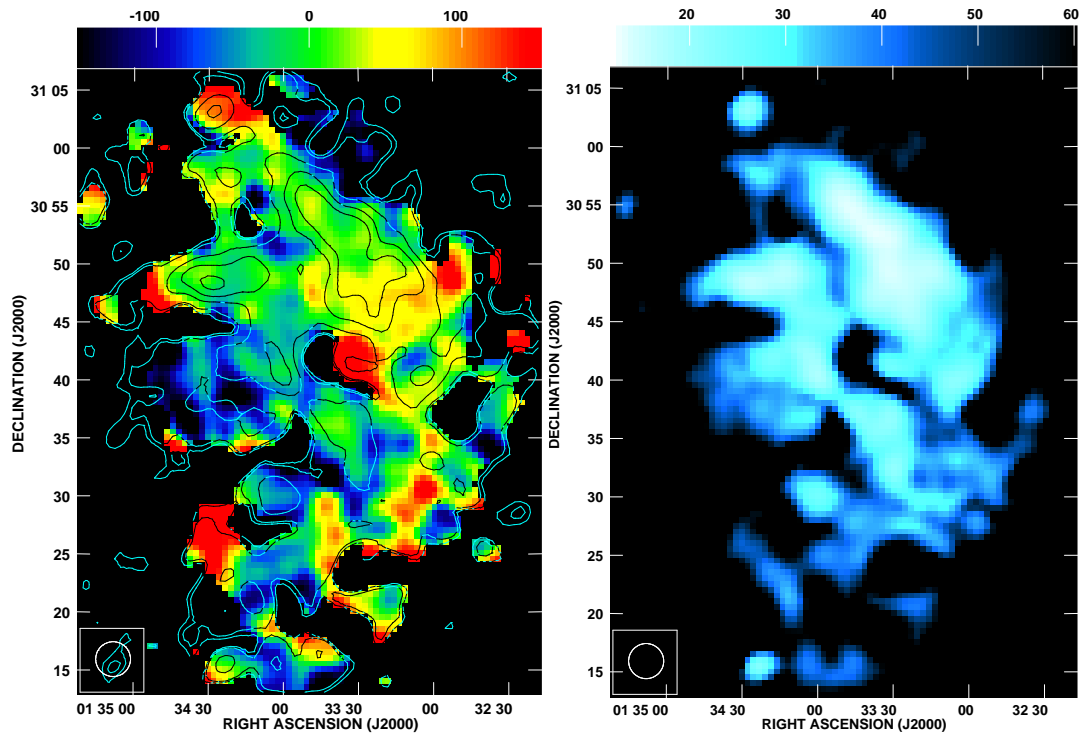


Figure 5.2: Rotation measure map of M33 between 3.6 and 6.2 cm after correction for the foreground RM. Overlaid are contours of 6.2 cm polarized intensity. Contour levels are 0.3, 0.4, 0.8, 1.2, 1.6, 3.2, 6.4 mJy/beam. The distribution of the estimated error in RM is shown in the right panel.

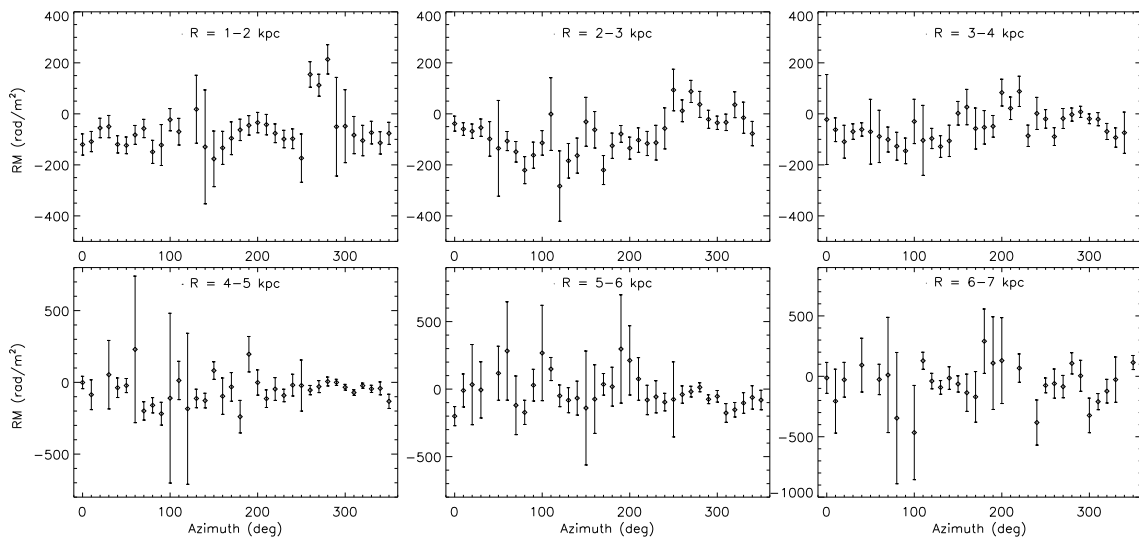


Figure 5.3: Azimuthal behavior of RM in M33 in different rings of 1 kpc width around the center of the galaxy.

Table 5.1: Integrated nonthermal flux densities and average nonthermal degree of polarization at $180''$.

λ (cm)	S_{nth} (mJy)	S_{PI} (mJy)	\bar{P}_{nth} %
3.6	370 ± 60	38 ± 4	10.3 ± 2.0
6.2	696 ± 110	79 ± 5	11.3 ± 1.9
20	1740 ± 65	115 ± 10	6.6 ± 0.6

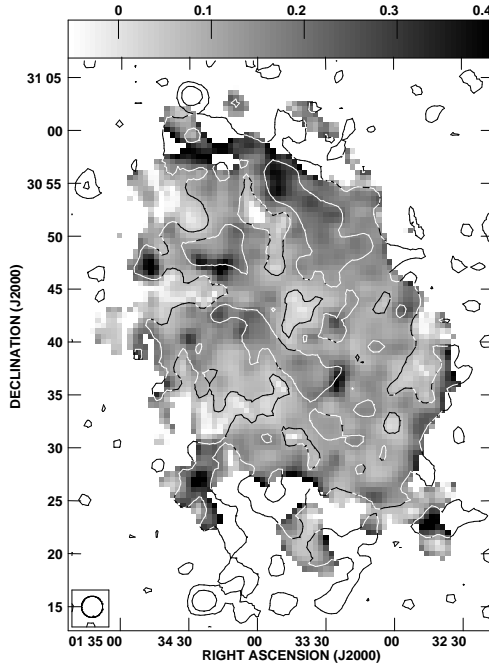


Figure 5.4: Nonthermal degree of polarization at 3.6 cm. Overlaid are contours of the linearly polarized intensity at 3.6 cm with levels of 0.1 and 0.3 mJy/beam.

5.3 Nonthermal degree of polarization

To verify the polarization due to synchrotron emission, the so-called nonthermal degree of polarization $P_{\text{nth}} = \text{PI}/I_{\text{nth}}$ is usually studied, where PI is the linearly polarized emission and I_{nth} is the flux density of the nonthermal emission. Using PI maps (Chapter 2) and the nonthermal maps (Chapter 4), we derived the maps of P_{nth} at different wavelengths. Fig. 5.4 shows P_{nth} at 3.6 cm. High nonthermal degrees of polarization ($P_{\text{nth}} > 30\%$) are found in the northern part of the magnetic filament (see chapter 2, corresponding to the second contour at $\text{DEC} > 30^\circ 54'$ in Fig. 5.4).

Integrating the polarized and nonthermal intensity maps in the galactic plane and for a galactocentric radius of $R \leq 7.5$ kpc, the average nonthermal degree of polarization $\bar{P}_{\text{nth}} = S_{\text{PI}}/S_{\text{nth}}$ is calculated. Table 5.1 gives \bar{P}_{nth} together with the integrated values of the nonthermal flux density and polarized intensity at different wavelengths. At the same angular resolution of $180''$, \bar{P}_{nth} is the same at 3.6 and 6.2 cm, confirming that Faraday depolarization effects are not significant at these wavelengths, generally. However, these effects are important at 20 cm providing a low \bar{P}_{nth} .

5.4 Magnetic field

Correcting the polarization angles for the rotation measure ($\phi_i = \phi - \lambda^2 \text{RM}_i$), the intrinsic direction of the magnetic field component in the plane of the sky (B_\perp) was obtained. Fig. 5.5 shows the corrected B_\perp -vectors superimposed on an optical image of M33. The orientation of B_\perp shows a spiral magnetic field pattern with open arms with approximately the same pitch angle of the optical arms in the north and south, but even larger in the east and west of the galaxy.

The regular magnetic field B_u in the disk of spiral galaxies is generally assumed to be dynamo-generated. The dynamo single modes of axisymmetric-spiral structure (ASS) and bisymmetric-spiral structure (BSS) can be distinguished from the azimuthal RM variation (as shown for M51, M81, and IC342 Tosa & Fujimoto 1978; Krause et al. 1989b,a). This analysis assumes that the magnetic field resides in the disk (or in a plane parallel to the disk), n_e is constant, and the field vectors follow spirals with constant pitch angles. In the ASS model, the RM variation can be fitted by the periodic function:

$$\text{RM}(\theta_0) = A \cos(\theta_0 - \psi) + \text{RM}_{\text{fg}}, \quad (5.4)$$

with ψ the pitch angle of the magnetic field vectors. Thus in the ASS model, the minimum and maximum of RM should be found near the northern and southern major axis.

In the BSS model,

$$\text{RM}(\theta_0) = A \cos(2\theta_0 - \psi - \mu) + A \cos(\mu - \psi) + \text{RM}_{\text{fg}}, \quad (5.5)$$

with μ the position angle of the magnetic spiral at a certain radius in the plane of the galaxy.

For M33, Beck (1979) and Buczilowski & Beck (1991) found that the BSS model can be best-fitted to the azimuthal RM variations. However, their RM information was only restricted to the northern half of this galaxy as they used low sensitivity polarization data. Such field structures can not be fitted to the RM variations obtained from our more complete and sensitive data (see Fig. 5.3). The least-squared fits failed to decrease the original standard deviation substantially. Besides to the RM variations in the south of M33 (Sect. 5.2), this may be other indication to a regular magnetic field that is not confined to the disk or a plane parallel to the disk (particularly in the southern half) and hence cannot be explained by only single modes of the dynamo action.

The strengths of the total magnetic field B_t and its regular component B_u can be found from the total synchrotron intensity and its degree of linear polarization P_{nth} . Assuming equipartition between the energy densities of the magnetic field and cosmic rays ($\varepsilon_{CR} = \varepsilon_{B_t} = B_t^2/8\pi$, Beck & Krause 2005),

$$B_t = \left\{ 4\pi(2\alpha_n + 1)(\mathbf{K} + 1) I_n E_p^{1-2\alpha_n} (\nu/2c_1)^{\alpha_n} \right. \\ \left. / [(2\alpha_n - 1) c_2(\alpha_n) l c_3] \right\}^{1/(\alpha_n+3)} \quad (5.6)$$

where I_n is the nonthermal intensity, \mathbf{K} the ratio between the number densities of cosmic ray protons and electrons, l the pathlength through the synchrotron emitting medium, and α_n the mean synchrotron spectral index. $E_p = 938.28 \text{ MeV} = 1.50 \times 10^{-3} \text{ erg}$ is the

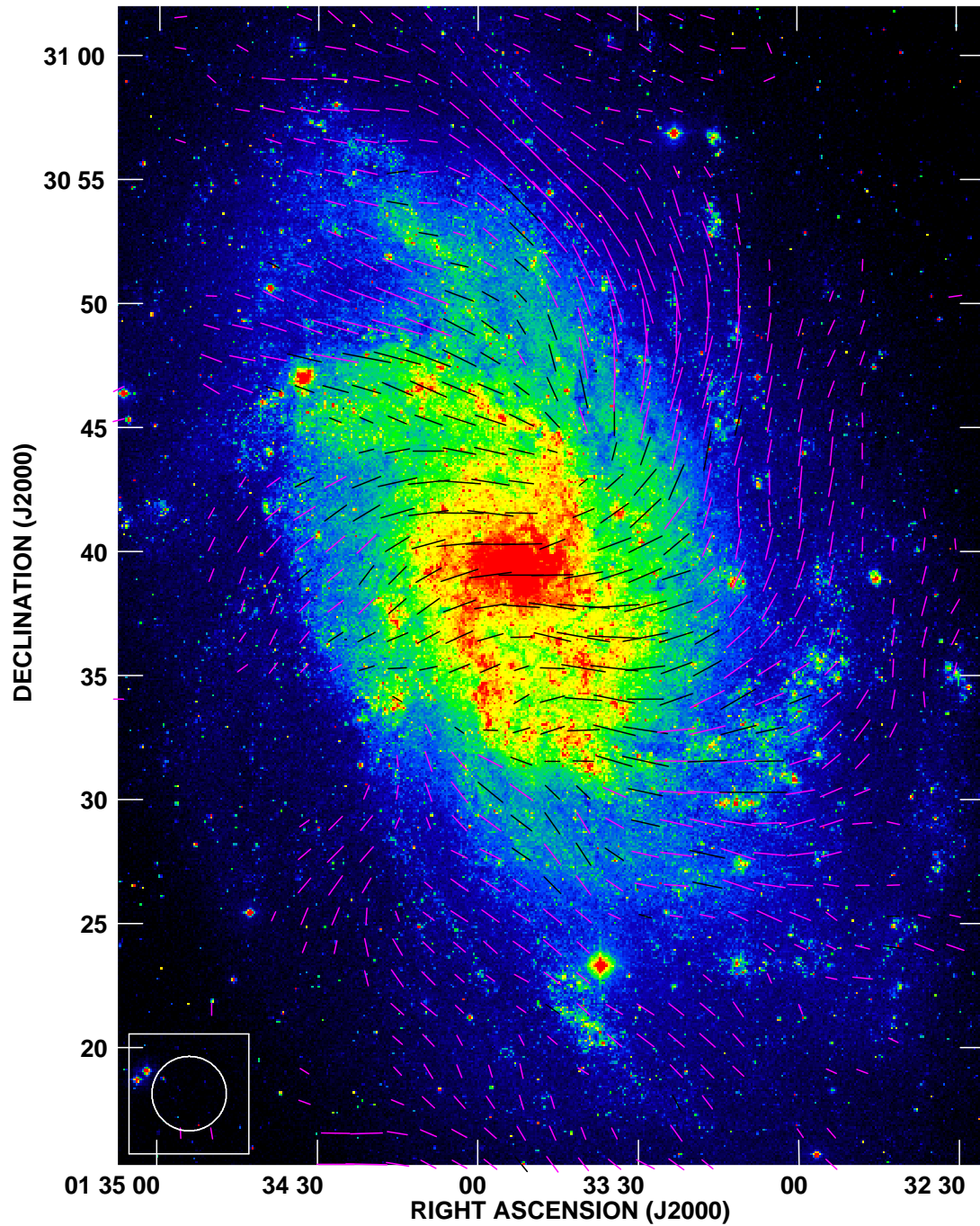


Figure 5.5: Optical image of M33 with overlaid vectors of the linearly polarized emission at 3.6 cm corrected for the Faraday rotation. A vector length of $1'$ represents a polarized intensity of 0.37 mJy/beam.

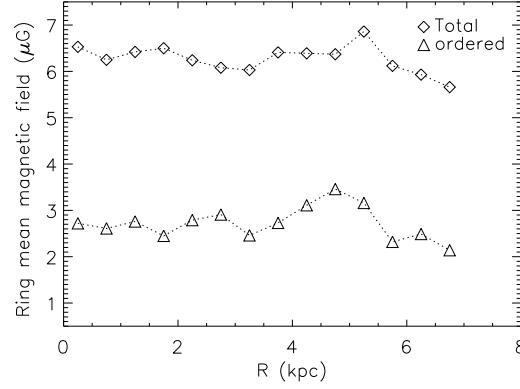


Figure 5.6: Variation of the mean total and ordered magnetic field strengths in rings of 500 pc with galactocentric radius.

proton rest energy and

$$\begin{aligned}
 c_1 &= 3e/(4\pi m_e^3 c^5) = 6.26428 \cdot 10^{18} \text{ erg}^{-2} \text{ s}^{-1} \text{ G}^{-1}, \\
 c_2(\alpha_n) &= \frac{1}{4} c_3 (\alpha_n + 5/3) / (\alpha_n + 1) \Gamma[(3\alpha_n + 1)/6] \\
 &\quad \times \Gamma[(3\alpha_n + 5)/6]
 \end{aligned} \tag{5.7}$$

For a region where the field is completely regular and has a constant inclination i with respect to the sky plane ($i = 0^\circ$ is the face-on view), $c_3 = [\cos(i)]^{(\alpha_n+1)}$. If the field is completely turbulent and has an isotropic angle distribution in three dimensions, $c_3 = (2/3)^{(\alpha_n+1)/2}$. If the synchrotron intensity is averaged over a large volume, $[\cos(i)]^{(\alpha_n+1)}$ has to be replaced by its average over all occurring values of i .

The strength of the regular magnetic field in the plane of the sky can be estimated from the observed nonthermal degree of polarization (Segalovitz et al. 1976):

$$\begin{aligned}
 P_{nth} &= \left(\frac{3\gamma + 3}{3\gamma + 7} \right) \left[1 + \frac{(1-q) \pi^{1/2} \Gamma[(\gamma+5)/4]}{2q\Gamma[(\gamma+7)/4]F(i)} \right]^{-1}, \\
 F(i) &= \frac{1}{2\pi} \int_0^{2\pi} (1 - \sin^2 i \sin^2 \theta)^{(\gamma+1)/4} d\theta,
 \end{aligned} \tag{5.8}$$

with $B_u/B_r = q^{2/(1+\gamma)}$, $\gamma = 2\alpha_n + 1$, and θ the azimuthal angle (B_r is the turbulent magnetic field). This formula assumes that the ordered magnetic field has a single orientation, is parallel to the disk and, taken over the galaxy as a whole, has no further preferential orientation with respect to any fixed direction in space.

The determined average values of I_n , α_n , and P_{nth} with the assumed values of \mathbf{K} ($\simeq 100$) and l ($\simeq 1$ kpc) lead to $B_t \simeq 6.4 \mu\text{G}$ and $B_u \simeq 2.5 \mu\text{G}$ for whole M33 ($R < 7.5$ kpc). The strongest ordered magnetic field is found in between the arms IV N and V N (in the magnetic filament, see Chapter 2) with $B_u \simeq 6.6 \mu\text{G}$ where $B_t \simeq 8.3 \mu\text{G}$.

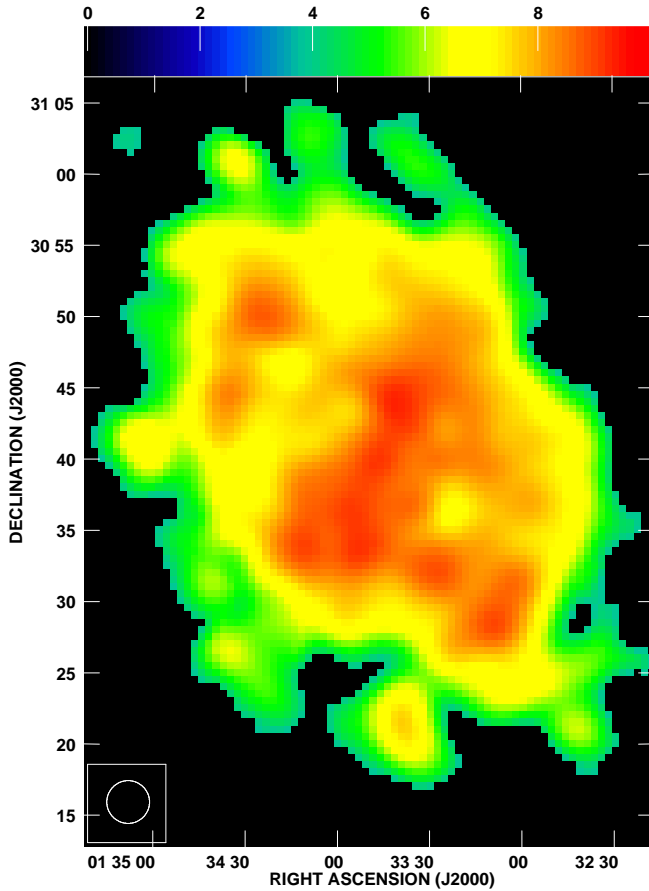


Figure 5.7: Distribution of the turbulent magnetic field strength, B_r (μG), in M33.

Using the mean synchrotron flux density, spectral index, and degree of polarization in rings, we also derive the average field strengths in rings. Fig. 5.6 shows some fluctuations but no systematic increase or decrease of these strengths with galactocentric radius (although B_t falls considerably in the last ring). The small bump at $4.5 < R < 5.5$ kpc is due to the M33's magnetic filament.

As the polarized intensity (PI) is related to the regular magnetic field, and the non-thermal intensity (I_n) to the total magnetic field in the plane of the sky, $I_n - \text{PI}$ gives the nonthermal emission due to the turbulent magnetic field B_r . This intensity with Eqs. (5.6) and (5.7) and assuming a completely turbulent field led to derive the distribution of B_r across the galaxy. Figure 5.7 shows strong B_r ($> 7 \mu\text{G}$) in the central region of the galaxy, the arm IS, and parts of the arm IN.

5.5 Depolarization

The observed depolarization at a certain wavelength is defined as the ratio of the non-thermal degree of linear polarization P_{nth} and the theoretical value p_0 . Generally, it may be caused by instrumental effects as the bandwidth and beamwidth of the observations or by the wavelength-dependent Faraday depolarization. Bandwidth depolarization oc-

curs when the polarization angles vary across the frequency band, reducing the observed amount of polarized emission. It is given by $\text{sinc}(2\text{RM} \lambda^2 \delta\nu/\nu)$, where $\delta\nu$ is the bandwidth of the observations (e.g. Reich 2006). In our study, the wavelengths, bandwidths and RM values lead to a negligible bandwidth depolarization.

Beam depolarization occurs when polarization vectors of different orientation are unresolved by the telescope beam. In order to compensate this effect, the ratio of the non-thermal degree of polarization at two wavelengths and at a same angular resolution is used,

$$\text{DP}_{\lambda_2/\lambda_1} = \frac{P_{\text{nth}}^{\lambda_2}}{P_{\text{nth}}^{\lambda_1}}, \quad (5.9)$$

where, $\lambda_2 > \lambda_1$. Then, the observed depolarization $\text{DP}_{\lambda_2/\lambda_1}$, that is wavelength-dependent, and called Faraday depolarization.

We derived the depolarization $\text{DP}_{20/3.6}$ using the maps of the nonthermal intensity and polarization at 20 and 3.6 cm at the same angular resolution of $180''$ (Fig. 5.9, top panel). Generally, the southern half of the galaxy is highly depolarized. While $\text{DP}_{20/3.6}$ changes between [0-0.5] in the south, it varies between [0.3-1] in the north. Considerable depolarization are found at the positions of NGC604, NGC595 and IC133. However, the strongest depolarization in the inner galaxy is found in the main southern arm IS. No depolarization ($\text{DP} \simeq 1$) is seen in the eastern edge of the minor axis and some northern regions.

According to Burn (1966) Faraday depolarization could be caused by the regular magnetic field and thermal electrons along the line of sight (depolarization due to differential Faraday rotation): when synchrotron emission originates in a magneto-ionic medium containing a regular magnetic field, the polarization plane of the radiation produced at different depths within the source is rotated over different angles by the Faraday effect. This results in a decrease in the degree of polarization of the integral emission observed. Faraday depolarization could also be caused by the turbulent magnetic field and thermal electrons along the line of sight (the so-called ‘Faraday dispersion’: depolarization due to dispersion in Faraday RM). When this dispersion is intrinsic to the source, it is called internal Faraday dispersion. In case of a dispersion in an external screen it is called external Faraday dispersion².

Generally, dealing with Faraday depolarization effects is very complicated and needs several free parameters which practically cannot be constrained. Here I only discuss simple models and try to find a qualitative agreement between the observed distribution of depolarization and results of these models.

Considering the dispersion in RM, $\sigma_{\text{RM}} = 0.81 \langle n_e \rangle B_r \sqrt{L \cdot d / f}$, the internal Faraday dispersion is given by

$$\text{DP}_r = \frac{1 - e^{-2\sigma_{\text{RM}}^2 \lambda^4}}{2\sigma_{\text{RM}}^2 \lambda^4} \quad (5.10)$$

(Sokoloff et al. 1998), with L the pathlength through the ionized medium, f the filling factor of the Faraday-rotating gas along the line of sight ($\simeq 0.5$, Beck 2007), and d the turbulent scale ($\simeq 50$ pc, Ohno & Shibata 1993). Using the $\text{H}\alpha$ emission measure ($EM =$

²This depolarization effect cannot be responsible for the north-south asymmetry in polarized emission from M33, as no asymmetry in the foreground distributions of RM (from galactic RM data by Johnston-Hollitt et al. 2004) and $\text{H}\alpha$ emission (from Wisconsin $\text{H}\alpha$ mapper) was found.

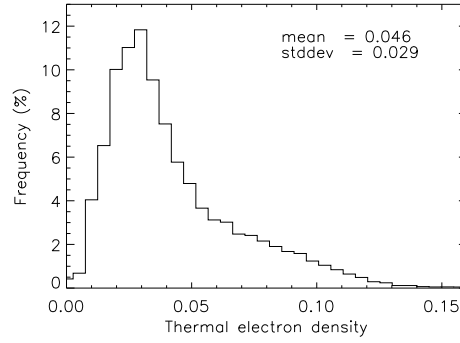


Figure 5.8: Histogram of the thermal electron density $\langle n_e \rangle$ (cm^{-3}) distribution across M33. A binning number of 70 was used for this plot.

$\int n_e^2 \cdot dl$) and a clumping factor $f_c = \langle n_e \rangle^2 / \langle n_e^2 \rangle$ describing the variations of the electron density, $\langle n_e \rangle$ can be determined by $\langle n_e \rangle = \sqrt{f_c EM/L}$. For the local interstellar medium, Manchester & Mebold (1977) found $f_c \simeq 0.05$. Assuming a thickness of $\simeq 1$ kpc for the thermal electrons in the disk of the galaxy (the Galactic value, Cordes & Lazio 2002) and correcting for the inclination of M33, we approximate $L \simeq 1800$ pc. Then the $H\alpha$ (EM) map of M33 leads to a distribution of $\langle n_e \rangle$ across the galaxy with a mean value of $\simeq 0.05 \text{ cm}^{-3}$ and a most probable value of $\simeq 0.03 \text{ cm}^{-3}$ (Fig. 5.8), that is in agreement with the estimated values in our galaxy (Lyne et al. 1985) and nearby galaxies IC382 (Krause et al. 1989b) and NGC5907 (Dumke et al. 2000). Note that a more realistic approach would consider different filling factors and electron densities for the thin and thick disk of the galaxy. However, because the only information we have is a superposition of these components along the line of sight, we are not able to distinguish the role of each component in this study. The resulting $\langle n_e \rangle$ with B_r obtained (Fig. 5.7) enable us to estimate DP_r at 3.6 and 20 cm. The left-bottom panel in Fig. 5.9 shows DP_r between 20 and 3.6 cm.

The next Faraday depolarization effect, differential Faraday rotation, for a symmetric layer is given by Sokoloff et al. (1998),

$$DP_u = \text{sinc} (2 \text{RM}_i \lambda^2). \quad (5.11)$$

Using the RM_i map (Fig. 5.2), DP_u between 20 and 3.6 cm was computed and shown in the right-bottom panel in Fig. 5.9.

In a qualitative comparison, both kinds of Faraday depolarization seem to be responsible for the observed depolarization in the galaxy. The global phenomenon, the north-south asymmetry in depolarization, is visible in DP_u . However, locally i.e. at the positions of HII complexes and the arm IS, the observed depolarization can be explained by DP_r . The contribution of each DP_u and DP_r varies region by region. A knowledge of how to combine DP_u and DP_r across the galaxy is required for a more quantitative comparison and needs detailed modeling. Furthermore, it is necessary to know the distribution of filling factors f and f_c , pathlength L , and the turbulent scale d across the galaxy.

Hence, we conclude that the highly turbulent southern arm IS with its chain of star-forming regions together with a magneto-ionic medium, which is probably not confined to

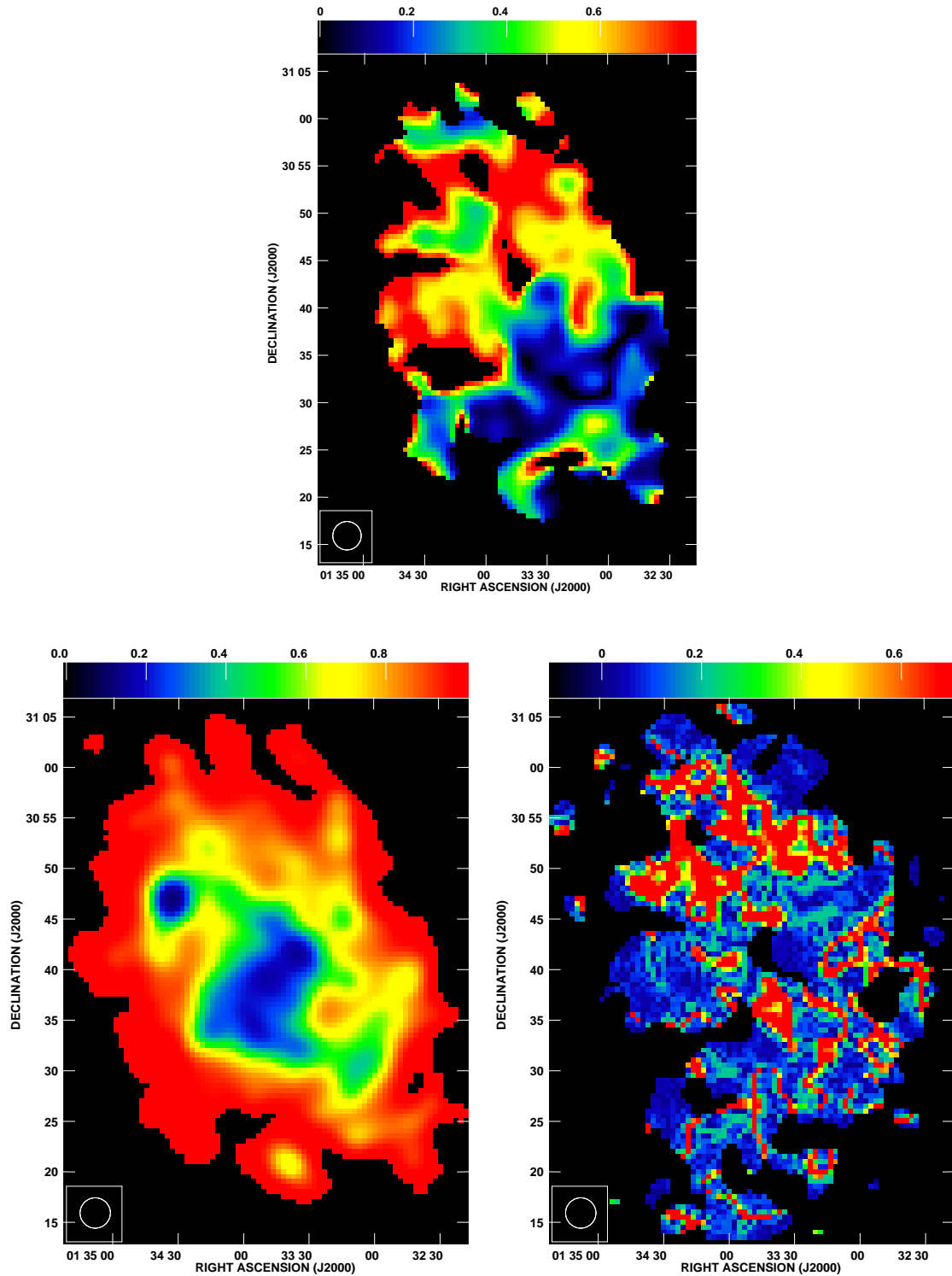


Figure 5.9: *Top*: observed depolarization between 3.6 and 20 cm. *Left-bottom*: depolarization due to dispersion in Faraday rotation, and *right-bottom*: depolarization due to differential Faraday rotation as measured between 3.6 and 20 cm.

the plane of the galaxy, containing a regular magnetic field, reduce the degree of polarization of the integral emission from the southern half and cause the wavelength-dependent north-south asymmetry in this galaxy.

The change of the optical spiral structure in M33 begins at a radius of about 4 kpc, where the HI warp begins. The inclination of the disk then tilts by about 40° . This is attributed to an external gas accretion, as recent optical and HI observations have detected extensions like a bridge between M33 and M31 (Ibata et al. 2007; Braun & Thilker 2004). Hence, M33's warp and/or a tidal force from its massive neighbor M31 may perturb the distribution of the ionized gas + regular magnetic field in the disk of the galaxy.

5.6 Conclusions

The linearly polarized intensity and polarization angle distributions at 3.6, 6.2, and 20 cm along with the nonthermal intensity and spectral index maps allowed to determine high-resolution distributions of RM, nonthermal degrees of polarization, and Faraday depolarization in M33. We found a nonthermal degree of polarization of $\simeq 10\%$ (at 3.6 cm) for the whole galaxy which is $> 30\%$ in the northern parts of the magnetic filament. Faraday depolarization is strong at 20 cm with reducing P_{nth} to $\simeq 6\%$.

We found an average total magnetic field strength of $B_t \simeq 6 \mu\text{G}$, stronger than that obtained by Buczylowski & Beck (1991) ($\simeq 4 \mu\text{G}$). This is probably due to an underestimate of the nonthermal intensity in the separation method used by Buczylowski & Beck (1991). The ordered magnetic field strength is higher within the ring at $4.5 < R < 5.5$ kpc, where the magnetic filament exists with a maximum regular field of $\simeq 6.6 \mu\text{G}$. Strong turbulent magnetic fields ($> 7 \mu\text{G}$) were found in the extended central region and the arms IS.

Comparing the south and north of M33, we found an excess of depolarization due to differential Faraday rotation in the south of M33. Furthermore, the main southern arm IS is highly depolarized due to dispersion in Faraday rotation. These may lead to the wavelength-dependent north-south asymmetry in polarization (or depolarization).

Strong variations in RM_i in the south of M33, where there is no correlation with PI and also with n_e , may indicate that the regular magnetic field in M33 is not confined to the disk. This may be linked to the warp in this galaxy. Furthermore, there are indications of strong magnetic fields B_{\parallel} in the eastern and western edges of the minor axis with opposite directions.

For a better understanding of the magnetic field configuration in M33, it is required to synthesis RM at as many wavelengths as possible (Brentjens & de Bruyn 2005) using multi-channel polarimeters at future high-sensitivity radio telescopes, e.g. the low frequency array (LOFAR).

6 Conclusions

M33's proximity and favorable inclination make it excellently suited for detailed studies of various astrophysical aspects. Although several studies have been carried out mainly in the optical regime, great efforts are required to explore the structure of the interstellar medium and different components that shape it, and to understand the energy balance of the interstellar medium as a function of galactic environment. This motivates high-resolution observations using different windows of the electromagnetic radiation.

A multi-wavelength study of the IR and radio emission from M33 using highly improved data is presented in this thesis. As the main topics, we investigate the energy sources of the IR emission and correlation with the radio emission, the variation in the spectral index of the synchrotron emission across the galaxy, the linearly polarized emission and magnetism. Previously, our knowledge was restricted to the poor resolution and low sensitivity data in both radio and IR regimes. New receivers of the 100-m Effelsberg telescope enabled us to achieve high-sensitivity and high-resolution radio maps in total power and linearly polarized intensity at 3.6 and 6.2 cm. These maps with those at 20 cm observed with the VLA provided our radio continuum window to M33. High resolution and sensitivity IR maps (at 24, 70, and 160 μm) were also achieved using the *Multiband Imaging Photometer* on board Spitzer satellite observatory. In this chapter, I present a brief summary of the work and highlight the main results and conclusions.

Radio continuum emission from M33

M33 was observed using the 3.6 cm dual channel and the 6.2 cm four-channel receivers of the 100-m Effelsberg telescope along with the L-band VLA D-array at 20 cm. These observations allowed to study the exponential scale length of the total radio emission, the spectral index distribution, and the linear radio polarization.

We detected considerable extended radio continuum emission, not only from the main spiral arms IS and IN, but also from the weaker arms. M33 belongs to those galaxies showing a sudden drop in their radial surface brightness profile in the optical regime. This break also exists in our radio profiles at $R \simeq 4$ kpc, where the warp starts, resulting in a larger exponential scale length inside than outside $R=4$ kpc. In contrast, the ring mean spectral index versus radius increases faster beyond $R=4$ kpc. We found a mean total spectral index of $\simeq 0.7$ for the whole M33. The most important conclusions are as follows.

- At $R < 4$ kpc, a spatial correlation between cosmic rays, magnetic fields, and star-forming regions exists.

- There is a north-south asymmetry in polarization that is frequency-dependent, indicating an asymmetry in Faraday depolarization.
- The total spectral index becomes slightly flatter at longer wavelengths that indicates a free-free absorption of the nonthermal emission in this galaxy.

More details are presented in Chapter 2, see also Tabatabaei et al. (2007c).

Thermal and nonthermal emission from M33

We developed a new method to separate thermal and nonthermal components of the radio continuum emission from M33 without the assumption of a constant nonthermal spectral index. Using the Spitzer FIR data at 70 and 160 μm and a standard dust model, we dereddened the $\text{H}\alpha$ emission. The extinction corrected $\text{H}\alpha$ emission served as a template for the thermal free-free radio emission. Subtracting from the observed 3.6 cm and 20 cm emission this free-free emission, we obtained the nonthermal maps. A constant electron temperature used to obtain the thermal radio intensity seems appropriate for M33 which, unlike the Milky Way, has a shallow metallicity gradient. On the other hand, the standard assumption of a constant nonthermal spectral index assumption imposes more uncertainty in the thermal/nonthermal distribution than a constant electron temperature. It is interesting that the obtained thermal fractions for the whole M33 at different wavelengths agree with those obtained from the standard method within the errors. This indicates that the assumption of a constant nonthermal spectral index (if known) is proper for global studies.

As expected, the nonthermal emission is distributed more smoothly than the thermal emission across M33, showing that the cosmic ray electrons diffuse to large scales, spiral around magnetic fields, and emit synchrotron emission. On the other hand, strong nonthermal emission is detected from giant star-forming regions and spiral arms, providing a spatial correlation between the thermal and nonthermal emissions, confirming our prediction in (Tabatabaei et al. 2007c). The most significant results are as follows.

- The mean extinction in rings in the galactic plane exhibits a shallow radial gradient.
- The wavelet transform of the nonthermal maps revealed that the nonthermal emission is smoother at 20 cm than at 3.6 cm, indicating that high-energy cosmic ray electrons experience more energy losses, and hence diffuse less than low-energy CR electrons.
- Assuming equipartition between the magnetic field and CRs, the scale length of the CR electrons and of the magnetic field estimated are $l_{cr} \simeq 12$ kpc and $l_B \simeq 24$ kpc in this galaxy.

In Chapter 4, we explain this method and compare it with the standard method in different aspects, see also Tabatabaei et al. (2007b).

Variations in the synchrotron spectral index across M33

Constraints on the origin and propagation of cosmic rays can be achieved by studying the variation in the spectral index of the synchrotron emission across external galaxies. For the first time, we determined variations in the nonthermal spectral index across a galaxy, M33. In the spiral arms, $\alpha_n = 0.6 \pm 0.1$, the typical spectral index of supernova remnants. The nonthermal spectrum in the interarm regions and the outer parts of the galaxy is steeper than that within the arms. This indicates energy-loss of the relativistic electrons when they diffuse from their origin in star-forming regions towards interarm regions and the outer parts of the galaxy. The main conclusions drawn by the nonthermal spectral index map are as follows.

- At $R < 4$ kpc, the ring-mean nonthermal spectral index varies between 0.65 and 0.9, indicating that cosmic ray electrons are injected by sources related to massive stars and diffused suffering a mixture of both leakage and synchrotron (and inverse-Compton) losses. At $R > 4.5$ kpc, synchrotron (and inverse-Compton) is the dominant energy loss mechanism as $\alpha_n \simeq 1$ on average.
- The nonthermal spectral index smaller than 0.5, found in some HII complexes like NGC604 and NGC592, indicates that ionization and free-free losses are dominant in these regions.
- Globally, the nonthermal emission from the southern half of the galaxy seems to have a steeper spectrum than that from the northern half, indicating a more important role of synchrotron and leakage losses in the southern half (that is possibly related to the vertical fields in the halo, see below).

Further details are presented in Chapter 4 (see also Tabatabaei et al. 2007b).

IR emission: energy sources and correlation with radio emission

In this study, we used the wavelet transform of the IR and radio maps to a) separate the diffuse emission components from compact sources, b) compare the emission at different wavelengths, and c) study the radio–IR correlation at various spatial scales. We also used the $H\alpha$ map as a tracer of the star forming regions. We found that the bright HII regions affect the wavelet spectra causing dominant small scales or decreasing trends towards the larger scales. The dominant scale of the $70 \mu\text{m}$ emission is larger than that of the $24 \mu\text{m}$ emission, while the $160 \mu\text{m}$ emission shows a smooth wavelet spectrum. The radio and $H\alpha$ maps are well correlated with all 3 MIPS maps, although their correlations with the $160 \mu\text{m}$ map are weaker. After subtracting the bright HII regions, the 24 and $70 \mu\text{m}$ maps show weaker correlations with the 20 cm map than with the 3.6 cm map at most scales. We also found a strong correlation between the 3.6 cm and $H\alpha$ emission at all scales. The most important conclusions concerning the scales smaller than 4 kpc are listed in the followings.

- The role of young, massive stars is more significant in heating the dust than that of a diffuse radiation field. The IR emission is influenced by O/B stars increasingly with decreasing wavelength from 160 to 24 μm .
- The radio–IR correlations indicate that the warm dust–thermal radio correlation is stronger than the cold dust–nonthermal radio correlation.
- A perfect 3.6 cm– $\text{H}\alpha$ correlation indicates small extinction of the $\text{H}\alpha$ emission by dust in M33 (this was also shown in Chapter 4, as $\tau_{\text{H}\alpha} < 1$ everywhere).

The radio–IR correlation described in Chapter 3 and published in Tabatabaei et al. (2007a), was re-investigated after the thermal/nonthermal separation (in Chapter 4), confirming a stronger warm dust–thermal than the cold dust–nonthermal radio correlation, and giving more results as follows.

- There is a characteristic scale range of 0.8 kpc–2 kpc where the IR–nonthermal radio correlation is maximum. This scale range includes the sizes of the giant molecular clouds, giant star forming regions, spiral arms, and the central extended region of M33.
- The better correlation of the cold dust with the thermal than with the nonthermal emission indicates that the role of UV photons from O/B stars is larger than that of the cosmic ray electrons in heating the cold dust at scales smaller than 4 kpc.
- The nonthermal 3.6 cm emission is better correlated with the warm dust than with the cold dust emission. This can be explained by the correlation of the nonthermal emission with the thermal emission e.g. because of strong magnetic fields and/or high densities of cosmic ray electrons in or nearby star-forming regions.

Magnetic fields in M33

We determined the distribution of the Faraday rotation measures across M33 at an angular resolution of 3' (0.7 kpc), indicating more variations in the south than in the north of the galaxy. In the south and also eastern and western minor axis, high values of the intrinsic rotation measure were found, where no dense medium of thermal electrons exists. Hence, in these regions, the regular magnetic field has strong components along the line of sight. These could be related to the M33's warp making the disk not a simple plane. This explains why single dynamo modes of ASS and BSS do not fit to the azimuthal behavior of the rotation measure. It is interesting that, in southern M33, there is a coincidence between the steeper nonthermal emission and stronger magnetic field along the line of sight which increases the effect of synchrotron losses. For the whole galaxy, we estimated the strengths of the total and regular magnetic fields as $\simeq 6.4 \mu\text{G}$ and $\simeq 2.5 \mu\text{G}$. Other highlights are as follows.

- The large-scale magnetic field exhibits a well ordered spiral structure with almost the same orientation as that of the optical spiral arms. However, there is no general structural correlation or anti-correlation between the magnetic and optical arms.

- The regular magnetic field in the south is not as confined to the disk as that in the north of the galaxy.
- High degree of polarization of the synchrotron emission ($> 20\%$) and strong regular magnetic field in the sky plane ($\simeq 6.6 \mu\text{G}$) are found in the northern magnetic filament.
- An excess of differential Faraday rotation in the southern half together with strong Faraday dispersion in the main southern arm IS seem to be responsible for the north-south asymmetry in the observed depolarization (which is wavelength dependent).

Details are presented in Chapter 5. More studies about the magnetic field structure and depolarization are in process. This work is going to be submitted to *Astronomy & Astrophysics* journal.

M33 versus other nearby galaxies

Most of the nearby spiral galaxies host a super massive black hole in their center that was made by merging with other galaxies, according to the galaxy formation scenarios. However, M33, with its small bulge and no satellite, is a rare example of a spiral galaxy that has not probably experienced merging in its formation history. On the other hand, it has a ten times more massive neighbor, M31, only 200 kpc away. Despite its much smaller mass, M33 has a star-formation rate comparable to that of M31. This provides a more efficient role of UV photons in heating the dust in M33 than in M31. While the total magnetic field strength are about the same in M33 and M31 ($\simeq 7 \mu\text{G}$), the ordered magnetic field strength in M33 is about half of that in M31 ($\simeq 4 \mu\text{G}$). M33's stronger depolarization and higher turbulence due to star-formation activities can explain this difference. In M31, the large-scale magnetic field is confined to the disk (toroidal) and follows the ASS dynamo model (Fletcher et al. 2004), in contrast to M33.

Like M33, spiral structure of the large-scale magnetic field has been found in M51, M81, IC342 as well, with different degrees of regularity. The spiral pattern of the magnetic field is generally linked to the $\alpha\Omega$ -dynamo action. In these galaxies, but M51, the regular magnetic field can be explained by a dominant single dynamo mode. The magnetic field in M51 is not confined to the disk and is extended to the halo (a magneto-ionic halo) with a structure different from that in the disk (Berkhuijsen et al. 1997). A similarity between M33 and M51 is that their magnetic fields are neither axisymmetric nor bisymmetric. This situation in M51 is perhaps due to the interaction with its companion, NGC5195, and in M33 possibly due to the warp in this galaxy (although the warp may also be linked or affected by a tidal interaction with M31).

A Ionization and recombination Processes

Some of absorption, emission, ionization, recombination, excitation, and de-excitation processes are described below. All these processes can occur when an incoming photon or electron interacts with an atom or ion.

1. **Induced absorption :** An incoming photon can excite an electron in an atom to a higher energy state $\epsilon_n = \epsilon_m + h\nu$. This process occurs with a probability that is proportional to the occupation number N_m in state m and the energy density U_ν of the radiation field, where the transition probabilities are specified by the Einstein coefficients B_{mn} , giving a transition rate $R = U_\nu B_{mn} N_m$.
2. **Stimulated emission :** An electron in an excited atom at energy state ϵ_n is stimulated by a passing photon ν from the ambient radiation field and falls back into a lower state ϵ_m , emitting during this process a second photon with energy $h\nu = \epsilon_n - \epsilon_m$. The probability of this process is also proportional to the energy density U_ν of the radiation field, as for induced absorption (i.e., with a rate of $R = U_\nu B_{nm} N_n$). This process is relevant to laser emission.
3. **Spontaneous emission:** In contrast to stimulated emission, no incoming photon is needed. An electron spontaneously falls from a higher energy state ϵ_n to a lower state ϵ_m by emission of a photon with $h\nu = \epsilon_n - \epsilon_m$. The probability is given by the Einstein coefficients A_{nm} , so the rate is $R = N_{nm} A_{nm}$.
4. **Photo-ionization:** This is a *bound-free transition*, where the incoming photon has a higher energy than the ionization energy (i.e., > 13.6 eV for hydrogen), so that the bound electron escapes from the atom. The wavelength of the incoming photon is $\lambda = hc/\Delta\epsilon$, with $\Delta\epsilon = \epsilon_i + \frac{1}{2}m_e v_e^2$, where ϵ_i is the ionization energy of the atom from the bound state ϵ_i of the electron, and $\frac{1}{2}m_e v_e^2$ is the kinetic energy of the free electron after escape.
5. **Radiative (or 2-body) recombination:** Recombination (also called *free-bound transition*) can occur by several processes, such as *radiative recombination*, *collisional recombination*, or *dielectronic recombination*. In *radiative recombination* a free electron is captured by an ion into one of the available energy states ϵ_i , while the excess energy is removed by emission of a photon with energy $h\nu = \frac{1}{2}m_e v_e^2 - \epsilon_i$, just as the time-reverse process of photo-ionization. This type of *bound-free transition* produces series limit continua such as the Balmer (3646 Å) and Lyman continua (912 Å) of hydrogen. These wavelengths correspond to the ionization energies

of $\epsilon_1 = 13.6$ eV from the ground state level $n = 1$ and $\epsilon_2 = 3.6$ eV from the first excited state $n = 2$.

6. **Dielectronic recombination:** The term *dielectronic recombination* indicates that two electrons are involved in this process. A free electron e_1^- is captured by an ion, resulting in a double excitation of the ion: (1) the original free electron lands in an excited state, and (2) a bound electron of the ion also becomes excited. Dielectronic recombination is accomplished when the highly unstable doubly excited configuration subsequently stabilizes, with one or both excited electrons falling back into vacancies of the lowest available states.
7. **Auto-ionization:** An ion is initially in a doubly excited state Z'' and auto-ionizes (i.e., it spontaneously ionizes without induced particle or photon) to $Z^+ + e^-$, thus leaving an ion and a free electron. If an electron from a lower energy state is knocked off, an electron from a higher energy level has to fall back to the emptied lower state to stabilize the ion. This process is also called *auto-ionization*.
8. **Thomson scattering:** It is the scattering of photons by free electrons which is independent of photon energy. The scattering rate is proportional to the electron density.
9. **Free-free emission:** This process is also called *bremsstrahlung*. Electrons are non-elastically scattered off ions and emit photons that have energies corresponding to the energy difference of the incoming and outgoing electron (i.e., $h\nu = \epsilon' - \epsilon$).
10. **Collisional ionization:** This occurs by collisions of ions with free electrons, when an orbiting electron of the ion (generally the outermost) is removed, and the ion is left in the next higher ionization state. This process is much more important than photo-ionization (when a photon incident on an ion results in removal of an orbiting electron).

B Wavelets as a tool for scaling analysis

The term wavelet means literally ‘little wave’, originated in the early 1980’s in its French version ‘ondelette’ in the work of Morlet and some seismologists. As an prototypical example, we consider Haar wavelet

$$h(x) = \begin{cases} 1, & 0 \leq x < \frac{1}{2} \\ -1, & \frac{1}{2} \leq x < 1 \\ 0, & \text{elsewhere.} \end{cases} \quad (\text{B.1})$$

Here, the ‘wavelet’ property is simply shown by the fact that h has average zero i.e.,

$$\int_{-\infty}^{\infty} h(x) dx = \int_0^1 h(x) dx = 0.$$

So, Haar wavelet has some oscillation but unlike such periodic functions as sine and cosine it has *compact support*: it lives on the interval $[0, 1)$ and does not oscillate everywhere on $(-\infty, \infty)$.

Wavelet analysis is based on a space-scale decomposition using the convolution of the data with a family of self-similar basic functions that depend on two parameters, scale and

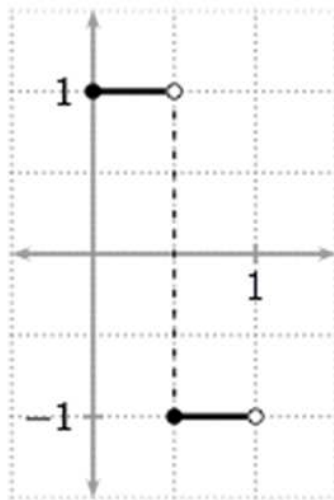


Figure B.1: Haar wavelet.

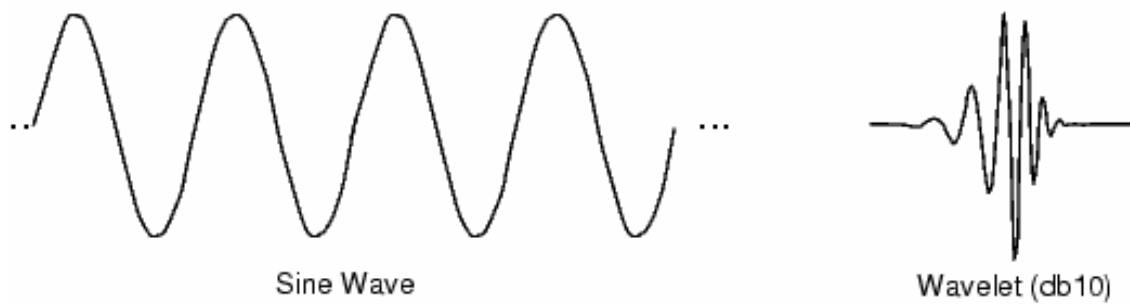


Figure B.2: The sinusoids have infinity support but the wavelets (here db10) have compact (or interval) support.

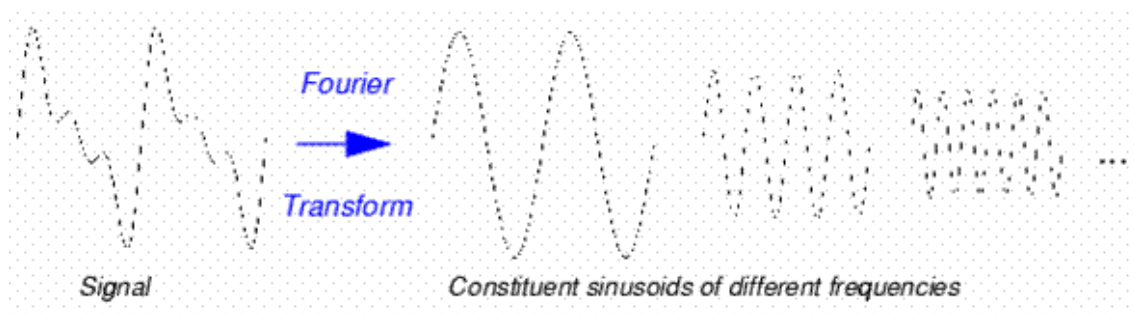


Figure B.3: An input signal decomposed by the fourier transform.

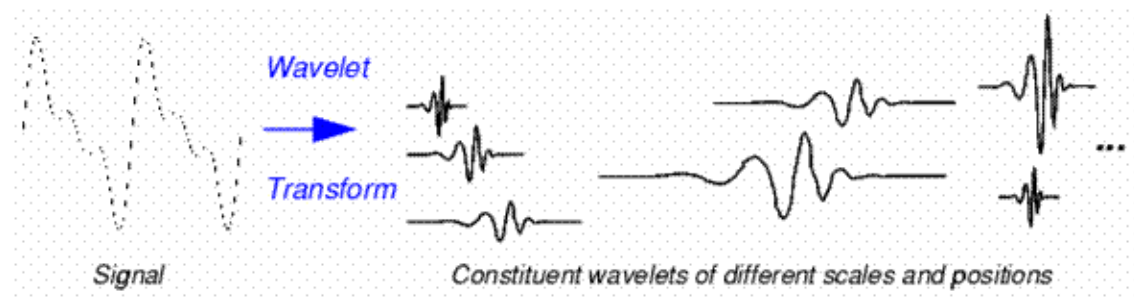


Figure B.4: An input signal decomposed by a wavelet transform.

location. It can be considered as a generalization of the Fourier transformation, which uses harmonic functions as a one-parametric functional basis, characterized by frequency, or in the case of a space function, by the wavevector \mathbf{k} . The wavelet transformation also uses oscillatory functions, but in contrast to the Fourier transform these functions rapidly decay towards infinity. The family of functions is generated by dilations and translations of the mother function, called the analysing wavelet. This procedure provides self-similarity, which distinguishes the wavelet technique from the windowed Fourier transformation, where the frequency, the width of the window and its position are independent parameters.

We consider the continuous wavelet transform, which in the two-dimensional case can be written in the form

$$W(a, \mathbf{x}) = \frac{1}{a^\kappa} \int_{-\infty}^{+\infty} \int_{-\infty}^{+\infty} f(\mathbf{x}') \psi^* \left(\frac{\mathbf{x}' - \mathbf{x}}{a} \right) d\mathbf{x}'. \quad (\text{B.2})$$

Here $\mathbf{x} = (x, y)$, $f(\mathbf{x})$ is a two-dimensional function, for which the Fourier transform exists (i.e. square integrated), $\psi(\mathbf{x})$ is the analysing wavelet (real or complex, * indicates the complex conjugation), a is the scale parameter, and κ is a normalization parameter which will be discussed below.

For later considerations the relation between the wavelet and the Fourier decomposition will be useful. The 2-D Fourier transform $\hat{f}(\mathbf{k})$ of the function $f(\mathbf{x})$ is defined as

$$\hat{f}(\mathbf{k}) = \int_{-\infty}^{+\infty} \int_{-\infty}^{+\infty} f(\mathbf{x}) e^{-i\mathbf{k}\mathbf{x}} d\mathbf{x}, \quad (\text{B.3})$$

where $\mathbf{k} = (k_x, k_y)$ is the wavevector. Then the inverse Fourier transform is

$$f(\mathbf{x}) = \frac{1}{4\pi^2} \int_{-\infty}^{+\infty} \int_{-\infty}^{+\infty} \hat{f}(\mathbf{k}) e^{i\mathbf{k}\mathbf{x}} d\mathbf{k} \quad (\text{B.4})$$

and the wavelet coefficients (B.2) can be expressed as

$$W(a, \mathbf{x}) = \frac{a^{2-\kappa}}{4\pi^2} \int_{-\infty}^{+\infty} \int_{-\infty}^{+\infty} \hat{f}(\mathbf{k}) \hat{\psi}^*(a\mathbf{k}) e^{i\mathbf{k}\mathbf{x}} d\mathbf{k}. \quad (\text{B.5})$$

The choice of the wavelet function depends on the data and on the goals of the analysis. For spectral analysis wavelets with good spectral resolution (i.e. well localized in Fourier space, or having many oscillations) are preferable, for local structure recognition a function, well localized in the physical space, is preferable. (Note that the spectral resolution Δk and the space resolution Δx are strongly related and are restricted by the uncertainty relation $\Delta x \Delta k \geq 2\pi$.) An obligatory property of the wavelet is the zero mean value $\int \int \psi(x, y) dx dy = 0$. An *isotropic* wavelet is an axisymmetric function $\psi = \psi(\rho)$, $\rho = \sqrt{x^2 + y^2}$.

A simple real isotropic wavelet with a minimal number of oscillations is known as the *Mexican Hat* (MH),

$$\psi(\rho) = (2 - \rho^2) e^{-\rho^2/2}. \quad (\text{B.6})$$

For a better separation of scales (to analyse spectra and to find the scale of dominant structures) another isotropic wavelet is used which is defined in Fourier space by the formula

$$\hat{\psi}(\mathbf{k}) = \begin{cases} \cos^2\left(\frac{\pi}{2} \log_2 \frac{k}{2\pi}\right) & : \quad \pi < |\mathbf{k}| < 4\pi \\ 0 & : \quad |\mathbf{k}| < \pi, |\mathbf{k}| > 4\pi \end{cases} \quad (\text{B.7})$$

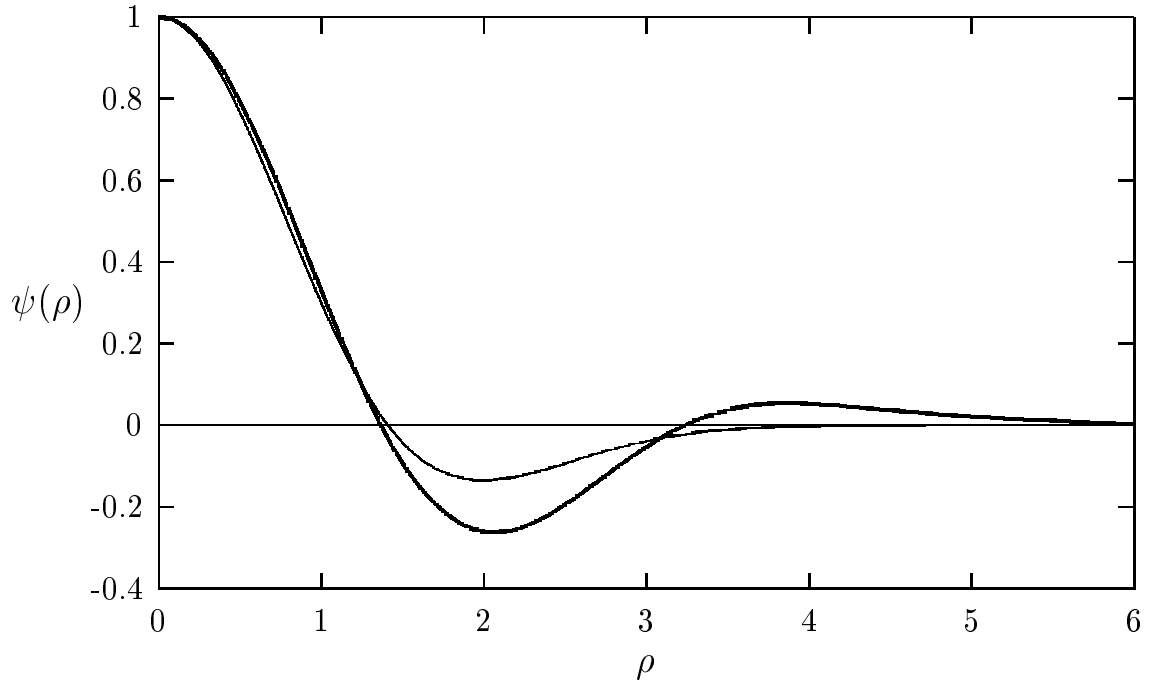


Figure B.5: Two isotropic wavelet functions: the MH wavelet (thin line) and the PH wavelet (thick line).

The function is localized in Fourier space in a ring with a median radius 2π and vanishes for $|\mathbf{k}| < \pi$ and $|\mathbf{k}| > 4\pi$. This wavelet definition provides a relatively good spectral resolution, it is referred to *Pet Hat* (PH) (Frick et al. 2001). In physical space the PH wavelet is obtained by numerical integration of (B.7). Both wavelets MH and PH are shown in Fig. B.5

The wavelet transform (B.2) is unique and reversible which means that the analyzed function $f(x, y)$ can be reconstructed from its wavelet decomposition. An extended description of continuum wavelet transform can be found in e.g. Holschneider (1995) and Torresani (1995).

Wavelet energy spectrum In the studies of scaling properties of turbulence a commonly used characteristic of a turbulent field is the *spectral energy density* $E(k)$ which includes the energy $F(\mathbf{k}) = |\hat{f}(\mathbf{k})|^2$ of all Fourier harmonics with wavenumbers \mathbf{k} , for which $|\mathbf{k}| = k$

$$E(k) = \int_{|\mathbf{k}|=k} F(\mathbf{k}) d\mathbf{k} . \quad (\text{B.8})$$

The spectral energy is related to the *autocorrelation* function

$$C(\mathbf{l}) = \int_{-\infty}^{+\infty} \int_{-\infty}^{+\infty} f(\mathbf{x}) f(\mathbf{l} - \mathbf{x}) d\mathbf{x} \quad (\text{B.9})$$

by its Fourier transform

$$F(\mathbf{k}) = \hat{C}(\mathbf{k}) = \int_{-\infty}^{+\infty} \int_{-\infty}^{+\infty} C(\mathbf{l}) e^{-i\mathbf{k}\mathbf{l}} d\mathbf{l} . \quad (\text{B.10})$$

The vector \mathbf{l} defines the shift of the image in the convolution (B.9) and is the scale parameter. In the important case of isotropic turbulence the autocorrelation function depends only on the distance between two points $C(\mathbf{l}) = C(l)$, and the spectral energy depends only on the modulus of the wavevector $F(\mathbf{k}) = F(k)$. Then these two functions are related by the Hankel transform

$$F(k) = 2\pi \int_0^{\infty} C(l) J_0(kl) l dl, \quad (\text{B.11})$$

where J_0 is the Bessel function and $E(k) = 2\pi k F(k)$.

Another often used characteristic for scaling studies is the *structure function* defined for arbitrary order q as

$$S_q(l) = \langle (f(\mathbf{x}) - f(\mathbf{x} - \mathbf{l}))^q \rangle_{|\mathbf{l}|=l}, \quad (\text{B.12})$$

where the brackets $\langle \dots \rangle$ mean the average value. Calculation of high-order structure functions requires a high accuracy of the initial data. In the case of maps of external galaxies, where a relatively small number of grid points is available and the noise is significant, only the second-order function S_2 , corresponding to the energy spectrum (B.8), can be discussed.

In the wavelet representation the scale distribution of the energy can be characterized by the *wavelet spectrum*, defined as the energy of the wavelet coefficients of scale a of the whole physical plane

$$M(a) = \int_{-\infty}^{+\infty} \int_{-\infty}^{+\infty} |W(a, \mathbf{x})|^2 d\mathbf{x}. \quad (\text{B.13})$$

The wavelet spectrum can be related to the Fourier spectrum. Using (B.5) one can easily rewrite (B.13) in the form

$$M(a) = \frac{a^{4-2\kappa}}{16\pi^4} \int_{-\infty}^{+\infty} \int_{-\infty}^{+\infty} |\hat{f}(\mathbf{k})|^2 |\hat{\psi}(a\mathbf{k})|^2 d\mathbf{k}. \quad (\text{B.14})$$

This relation shows that the wavelet spectrum is a smoothed version of the Fourier spectrum. In the isotropic case (B.14) has a more simple form

$$M(a) = \frac{a^{4-2\kappa}}{8\pi^3} \int_0^{\infty} E(k) |\hat{\psi}(ak)|^2 dk. \quad (\text{B.15})$$

C Effective optical depth

The general radiative transfer equation for a medium in case of both absorption and emission can be written as

$$\frac{dI}{d\tau} = S - I, \quad (\text{C.1})$$

from which the integral form of the transfer equation follows formally,

$$I = I_0 e^{-\tau} + \int_0^{\tau} S(\tau') e^{-(\tau-\tau')} d\tau', \quad (\text{C.2})$$

with τ the optical depth of the medium, I_0 the intensity of an incoming emission from background, and S the so called source function (the ratio of the emissivity to the absorption factor).

Considering a homogeneous mixing of emitting (sources) and absorbing media, (C. 2) is converted to

$$I = S_0 (1 - e^{-\tau}), \quad (\text{C.3})$$

(Rybicki & Lightman 1979) with S_0 the total intrinsic intensity and neglecting the background emission.

Now, a question is assuming this medium is occupied only by a homogeneous distribution of the emitters, what would be the effective thickness of an only absorbing medium in front of this emission to give the same amount of intensity in (C. 3).

For only emitting medium, the radiative transfer gives

$$I_e = S_0 \tau, \quad (\text{C.4})$$

and for only absorbing medium,

$$I_a = I_e e^{-\tau_{\text{eff}}}, \quad (\text{C.5})$$

or using (C. 4)

$$I_a = S_0 \tau e^{-\tau_{\text{eff}}}. \quad (\text{C.6})$$

I_a should be equivalent to I in (C. 3), thus

$$(1 - e^{-\tau})/\tau = e^{-\tau_{\text{eff}}}. \quad (\text{C.7})$$

Expanding both sides as series,

$$1 - \frac{\tau}{2} + \frac{\tau^2}{6} - \dots = 1 - \tau_{\text{eff}} + \frac{(\tau_{\text{eff}})^2}{2} - \dots \quad (\text{C.8})$$

Neglecting $O(2)$ in the optically thin condition gives $\tau_{\text{eff}} = \frac{1}{2} \tau$. However, values of $\tau \approx 1$ does not harm the optically thin assumption as $\tau_{\text{eff}} \approx 0.46$.

Bibliography

- Altenhoff, W., Mezger, P. G., Wendker, H., & Westerhout, G. 1960, *Veroff Sternwarte Bonn*, 59, 48
- Andriesse, C. D. 1974, *A&A*, 37, 257
- Baars, J. W. M., Genzel, R., Pauliny-Toth, I. I. K., & Witzel, A. 1977, *A&A*, 61, 99
- Beck, R. 1979, Ph.D. Thesis, Rheinische Friedrich-Wilhelms-Universitaet, Bonn.
- Beck, R. 2007, *A&A*, 470, 539
- Beck, R., Brandenburg, A., Moss, D., Shukurov, A., & Sokoloff, D. 1996, *ARA&A*, 34, 155
- Beck, R. & Golla, G. 1988, *A&A*, 191, L9
- Beck, R. & Gräve, R. 1982, *A&A*, 105, 192
- Beck, R. & Krause, M. 2005, *Astronomische Nachrichten*, 326, 414
- Berkhuijsen, E. M. 1982, *A&A*, 112, 369
- Berkhuijsen, E. M. 1983, *A&A*, 127, 395
- Berkhuijsen, E. M., Beck, R., & Hoernes, P. 2003, *A&A*, 398, 937
- Berkhuijsen, E. M., Horellou, C., Krause, M., et al. 1997, *A&A*, 318, 700
- Berkhuijsen, E. M. & Klein, U. 1985, in *IAU Symposium, Vol. 106, The Milky Way Galaxy*, ed. H. van Woerden, R. J. Allen, & W. B. Burton, 431–434
- Bianchi, S., Davies, J. I., & Alton, P. B. 2000, *A&A*, 359, 65
- Bicay, M. D. & Helou, G. 1990, *ApJ*, 362, 59
- Biermann, P. & Harwit, M. 1980, *ApJ*, 241, L105
- Biermann, P. L. 1995, *astro-ph/9501030*
- Bothun, G. D. & Rogers, C. 1992, *AJ*, 103, 1484
- Boulesteix, J., Courtes, G., Laval, A., Monnet, G., & Petit, H. 1974, *A&A*, 37, 33

- Braun, R. & Thilker, D. 2004, in *Astronomical Society of the Pacific Conference Series*, Vol. 327, *Satellites and Tidal Streams*, ed. F. Prada, D. Martinez Delgado, & T. J. Mahoney, 139
- Breitschwerdt, D., Dogiel, V. A., & Völk, H. J. 2002, *A&A*, 385, 216
- Brentjens, M. A. & de Bruyn, A. G. 2005, *A&A*, 441, 1217
- Broadbent, A., Osborne, J. L., & Haslam, C. G. T. 1989, *MNRAS*, 237, 381
- Brotten, N. W., MacLeod, J. M., & Vallee, J. P. 1988, *Ap&SS*, 141, 303
- Buczilowski, U. R. & Beck, R. 1991, *A&A*, 241, 47
- Buczilowski, U. R. 1988, *A&A*, 205, 29
- Buczilowski, U. R. & Beck, R. 1987, *A&AS*, 68, 171
- Burn, B. J. 1966, *MNRAS*, 133, 67
- Chyży, K. T., Bomans, D. J., Krause, M., et al. 2007, *A&A*, 462, 933
- Corbelli, E. & Salpeter, E. E. 1993, *ApJ*, 419, 104
- Corbelli, E. & Salucci, P. 2000, *MNRAS*, 311, 441
- Corbelli, E. & Schneider, S. E. 1997, *ApJ*, 479, 244
- Cordes, J. M. & Lazio, T. J. W. 2002, *ArXiv Astrophysics e-prints*
- Crockett, N. R., Garnett, D. R., Massey, P., & Jacoby, G. 2006, *ApJ*, 637, 741
- de Jong, T., Klein, U., Wielebinski, R., & Wunderlich, E. 1985, *A&A*, 147, L6
- de Vaucouleurs, G., de Vaucouleurs, A., Corwin, Jr., H. G., et al. 1991, *Third Reference Catalogue of Bright Galaxies (Volume 1-3, XII, 2069 pp. 7 figs.. Springer-Verlag Berlin Heidelberg New York)*
- de Vaucouleurs, G. & Leach, R. W. 1981, *PASP*, 93, 190
- Deul, E. R. 1989, *A&A*, 218, 78
- Deul, E. R. & van der Hulst, J. M. 1987, *A&AS*, 67, 509
- Devereux, N., Duric, N., & Scowen, P. A. 1997, *AJ*, 113, 236
- Devereux, N. A., Jacoby, G., & Ciadullo, R. 1996, *AJ*, 111, 2115
- Devereux, N. A., Price, R., Wells, L. A., & Duric, N. 1994, *AJ*, 108, 1667
- Dickinson, C., Davies, R. D., & Davis, R. J. 2003, *MNRAS*, 341, 369
- Dodorico, S. 1978, *Mem. Soc. Astr. Ital.*, 49, 485

- Draine, B. T. & Lee, H. M. 1984, *ApJ*, 285, 89
- Dumke, M., Krause, M., & Wielebinski, R. 2000, *A&A*, 355, 512
- Duric, N., Gordon, S. M., Goss, W. M., Viallefond, F., & Lacey, C. 1995, *ApJ*, 445, 173
- Duric, N., Viallefond, F., Goss, W. M., & van der Hulst, J. M. 1993, *A&AS*, 99, 217
- Ehle, M. & Beck, R. 1993, *A&A*, 273, 45
- Emerson, D. T. & Graeve, R. 1988, *A&A*, 190, 353
- Emerson, D. T., Klein, U., & Haslam, C. G. T. 1979, *A&A*, 76, 92
- Fletcher, A., Berkhuijsen, E. M., Beck, R., & Shukurov, A. 2004, *A&A*, 414, 53
- Fletcher, A. 2001, Ph.D. Thesis, University of Newcastle, U.K.
- Fletcher, A., Berkhuijsen, E. M., Beck, R., & Shukurov, A. 2004, *A&A*, 414, 53
- Freedman, W. L., Wilson, C. D., & Madore, B. F. 1991, *ApJ*, 372, 455
- Frick, P., Beck, R., Berkhuijsen, E. M., & Patrickeyev, I. 2001, *MNRAS*, 327, 1145
- Fürst, E., Reich, W., & Sofue, Y. 1987, *A&AS*, 71, 63
- Gavazzi, G., Cocito, A., & Vettolani, G. 1986, *ApJ*, 305, L15
- Gioia, I. M., Gregorini, L., & Klein, U. 1982, *A&A*, 116, 164
- Gordon, K. D., Clayton, G. C., Witt, A. N., & Misselt, K. A. 2000, *ApJ*, 533, 236
- Gordon, K. D., Pérez-González, P. G., Misselt, K. A., et al. 2004a, *ApJS*, 154, 215
- Gordon, K. D., Pérez-González, P. G., Misselt, K. A., et al. 2004b, *ApJS*, 154, 215
- Gordon, K. D., Rieke, G. H., Engelbracht, C. W., et al. 2005, *PASP*, 117, 503
- Gordon, S. M., Duric, N., Kirshner, R. P., Goss, W. M., & Viallefond, F. 1999, *ApJS*, 120, 247
- Gordon, S. M., Kirshner, R. P., Duric, N., & Long, K. S. 1993, *ApJ*, 418, 743
- Gordon, S. M., Kirshner, R. P., Long, K. S., et al. 1998, *ApJS*, 117, 89
- Haslam, C. G. T. 1974, *A&AS*, 15, 333
- Helou, G. & Bica, M. D. 1993, *ApJ*, 415, 93
- Helou, G., Soifer, B. T., & Rowan-Robinson, M. 1985, *ApJ*, 298, L7
- Hinz, J. L., Rieke, G. H., Gordon, K. D., et al. 2004, *ApJS*, 154, 259
- Hippelein, H., Haas, M., Tuffs, R. J., et al. 2003, *A&A*, 407, 137

- Hirashita, H., Buat, V., & Inoue, A. K. 2003, *A&A*, 410, 83
- Hoernes, P., Berkhuijsen, E. M., & Xu, C. 1998, *A&A*, 334, 57
- Holschneider, M. 1995, *Wavelets: An Analysis Tool* (Oxford University Press, Oxford)
- Hoopes, C. G. & Walterbos, R. A. M. 2000, *ApJ*, 541, 597
- Hughes, A., Wong, T., Ekers, R., et al. 2006, *MNRAS*, 613
- Humphreys, R. M. & Sandage, A. 1980, *ApJS*, 44, 319
- Ibata, R., Martin, N. F., Irwin, M., et al. 2007, *ArXiv e-prints*, 704
- Israel, F. P. & Kennicutt, R. C. 1980, *ApL*, 21, 1
- Israel, F. P., Mahoney, M. J., & Howarth, N. 1992, *A&A*, 261, 47
- Israel, F. P. & van der Kruit, P. C. 1974, *A&A*, 32, 363
- Johnson, K. E., Kobulnicky, H. A., Massey, P., & Conti, P. S. 2001, *ApJ*, 559, 864
- Johnston-Hollitt, M., Hollitt, C. P., & Ekers, R. D. 2004, in *The Magnetized Interstellar Medium*, ed. B. Uyaniker, W. Reich, & R. Wielebinski, 13–18
- Jones, L. V., Elston, R. J., & Hunter, D. A. 2002, *AJ*, 124, 2548
- Kennicutt, Jr., R. C. 1998, *ARA&A*, 36, 189
- Killeen, N. E. B., Bicknell, G. V., & Ekers, R. D. 1986, *ApJ*, 302, 306
- Klein, U., Beck, R., Buczylowski, U. R., & Wielebinski, R. 1982, *A&A*, 108, 176
- Klein, U., Wielebinski, R., & Beck, R. 1984, *A&A*, 135, 213
- Kolmogorov, A. N. 1941, *Dokl. Akad. Nauk.*, 31, 99
- Kormendy, J. & McClure, R. D. 1993, *AJ*, 105, 1793
- Krause, M. 1993, in *IAU Symp. 157: The Cosmic Dynamo*, ed. F. Krause, K. H. Radler, & G. Rudiger, 305–+
- Krause, M., Beck, R., & Hummel, E. 1989a, *A&A*, 217, 17
- Krause, M., Hummel, E., & Beck, R. 1989b, *A&A*, 217, 4
- Krügel, E. 2003, *The physics of interstellar dust* (The physics of interstellar dust, by Endrik Krügel. IoP Series in astronomy and astrophysics, ISBN 0750308613. Bristol, UK: The Institute of Physics, 2003.)
- Kwitter, K. B. & Aller, L. H. 1981, *MNRAS*, 195, 939
- Lang, K. R. 1999, *Astrophysical formulae* (Vol. 1, 3rd ed., Springer, Berlin)

- Lauer, T. R., Faber, S. M., Ajhar, E. A., Grillmair, C. J., & Scowen, P. A. 1998, *AJ*, 116, 2263
- Li, J., Ma, J., Zhou, X., et al. 2004, *A&A*, 420, 89
- Lyne, A. G., Manchester, R. N., & Taylor, J. H. 1985, *MNRAS*, 213, 613
- Magrini, L., Corbelli, E., & Galli, D. 2007, *ArXiv e-prints*, 704
- Manchester, R. N. & Mebold, U. 1977, *A&A*, 59, 401
- Mathis, J. S., Rumpl, W., & Nordsieck, K. H. 1977, *ApJ*, 217, 425
- McConnachie, A. W., Chapman, S. C., Ibata, R. A., et al. 2006, *ApJ*, 647, L25
- McLean, I. S. & Liu, T. 1996, *ApJ*, 456, 499
- Melnick, J., Moles, M., Terlevich, R., & Garcia-Pelayo, J.-M. 1987, *MNRAS*, 226, 849
- Mezger, P. G. & Henderson, A. P. 1967, *ApJ*, 147, 471
- Minniti, D., Olszewski, E. W., & Rieke, M. 1993, *ApJ*, 410, L79
- Misiriotis, A., Popescu, C. C., Tuffs, R., & Kylafis, N. D. 2001, *A&A*, 372, 775
- Murphy, E. J., Braun, R., Helou, G., et al. 2006, *ApJ*, 638, 157
- Niklas, S. & Beck, R. 1997, *A&A*, 320, 54
- Niklas, S., Klein, U., & Wielebinski, R. 1997, *A&A*, 322, 19
- Ohno, H. & Shibata, S. 1993, *MNRAS*, 262, 953
- Pacholczyk, A. G. 1970, *Radio astrophysics (Series of Books in Astronomy and Astrophysics, San Francisco: Freeman and Co.)*
- Panagia, N. 1979, *Memorie della Societa Astronomica Italiana*, 50, 79
- Petersen, L. & Gammelgaard, P. 1997, *A&A*, 323, 697
- Popescu, C. C., Misiriotis, A., Kylafis, N. D., Tuffs, R. J., & Fischera, J. 2000, *A&A*, 362, 138
- Popescu, C. C., Tuffs, R. J., Völk, H. J., Pierini, D., & Madore, B. F. 2002, *ApJ*, 567, 221
- Regan, M. W. & Vogel, S. N. 1994, *ApJ*, 434, 536
- Regan, M. W. & Vogel, S. N. 1994, *ApJ*, 434, 536
- Reich, W. 2006, *ArXiv Astrophysics e-prints*
- Rieke, G. H., Young, E. T., Engelbracht, C. W., et al. 2004, *ApJS*, 154, 25

- Rybicki, G. B. & Lightman, A. P. 1979, Radiative processes in astrophysics (New York, Wiley-Interscience, 1979. 393 p. 14)
- Sandage, A. & Humphreys, R. M. 1980, ApJ, 236, L1
- Sandage, A. & Tammann, G. A. 1981, A revised Shapley-Ames Catalog of bright galaxies (Washington: Carnegie Institution, 1981, Preliminary version)
- Sauvage, M. & Thuan, T. X. 1992, ApJ, 396, L69
- Schulman, E. & Bregman, J. N. 1995, ApJ, 441, 568
- Segalovitz, A., Shane, W. W., & de Bruyn, A. G. 1976, Nature, 264, 222
- Shaver, P. A., McGee, R. X., Newton, L. M., Danks, A. C., & Pottasch, S. R. 1983, MNRAS, 204, 53
- Simard-Normandin, M. & Kronberg, P. P. 1980, ApJ, 242, 74
- Sofue, Y. & Reich, W. 1979, A&AS, 38, 251
- Sokoloff, D. D., Bykov, A. A., Shukurov, A., et al. 1998, MNRAS, 299, 189
- Spangler, S. R. 1991, ApJ, 376, 540
- Tabara, H. & Inoue, M. 1980, A&AS, 39, 379
- Tabatabaei, F., Krause, M., & Beck, R. 2005, AN, 326, 532
- Tabatabaei, F. S., Beck, R., Krause, M., et al. 2007a, A&A, 466, 509
- Tabatabaei, F. S., Beck, R., Krügel, E., et al. 2007b, A&A, 475, 133
- Tabatabaei, F. S., Krause, M., & Beck, R. 2007c, A&A, 472, 785
- Terzian, Y. & Pankonin, V. 1972, ApJ, 174, 293
- Tilanus, R. P. J., Allen, R. J., van der Hulst, J. M., Crane, P. C., & Kennicutt, R. C. 1988, ApJ, 330, 667
- Torresani, B. 1995, Continuous Wavelet Transform (Savoire, Paris)
- Tosa, M. & Fujimoto, M. 1978, PASJ, 30, 315
- Trewhella, M. 1998, MNRAS, 297, 807
- Urbanik, M., Elstner, D., & Beck, R. 1997, A&A, 326, 465
- Valls-Gabaud, D. 1998, Publ. Astr. Soc. Austr, 15, 111
- Viallefond, F., Goss, W. M., van der Hulst, J. M., & Crane, P. C. 1986a, A&AS, 64, 237
- Viallefond, F., Goss, W. M., van der Hulst, J. M., & Crane, P. C. 1986b, A&AS, 64, 237

- von Kap-Herr, A., Berkhuijsen, E. M., & Wielebinski, R. 1978, *A&A*, 62, 51
- Walsh, W., Beck, R., Thuma, G., et al. 2002, *A&A*, 388, 7
- Walterbos, R. A. M. & Greenawalt, B. 1996, *ApJ*, 460, 696
- Watson, R. A., Rebolo, R., Rubiño-Martín, J. A., et al. 2005, *ApJ*, 624, L89
- Westfold, K. C. 1959, *ApJ*, 130, 241
- Willner, S. P. & Nelson-Patel, K. 2002, *ApJ*, 568, 679
- Witt, A. N. & Gordon, K. D. 2000, *ApJ*, 528, 799
- Xu, C. 1990, *ApJ*, 365, L47
- Xu, C. & Helou, G. 1996, *ApJ*, 456, 163
- Yang, H., Chu, Y.-H., Skillman, E. D., & Terlevich, R. 1996, *AJ*, 112, 146
- Young, J. S. & Scoville, N. 1982, *ApJ*, 260, L11
- Zhou, Z. & Adeli, H. 2003, *International Journal of Imaging Systems and Technology*, 13, 133

Curriculum vitae

Address

Max-Planck-Institut für Radioastronomie
Auf dem Hügel 69
53121 Bonn, Germany
Tel: +49 228 525 324
Fax: +49 228 525 229
Email: tabataba@mpifr-bonn.mpg.de

Personal Details

Gender: Female
Date of birth: 31 August 1974
Place of birth: Tehran, Iran
Marital status: Married

Education

10/1993-07/1997 Undergraduate Student in Physics (Bachelor of science) at the University of Tehran (<http://www.ut.ac.ir>)

10/1997-01/2000 Graduate student in Physics (Master of Science) at the Institute for Advanced Studies in Basic Sciences (IASBS), Zanjan (<http://iasbs.ac.ir>)
Specialization: Astrophysics
Thesis title: A Phenomenological Study of Evolution of Galaxies and QSOs
Advisor: Dr. Sadollah Nasiri

01/2005- 01/2008 PhD student at the Max-Planck-Institut für Radioastronomie, Bonn (<http://www.mpifr-bonn.mpg.de>)
Thesis title: Thermal and Nonthermal Emission from the Nearby Galaxy M33
Supervisor: Prof. Dr. Uli Klein

Academic Experience

10/2000-07/2002 Physics teacher in Imam Reza College, Tehran.

10/2002-01/2003 Laboratory expert in Azad University, Tehran.

01/2003-07/2003 Teaching in Shahrood University, Shahrood.

10/2003-07/2004 Teaching in Damghan University, Damghan.

Publications

- Tabatabaei, F. S., Krause, M., and Beck, R.
High-resolution radio continuum survey of M 33. I. The radio maps, Astronomy & Astrophysics, 2007, V. 472, p. 785
- Tabatabaei, F. S. and Beck, R., Krügel, E., Krause, M., Berkhuijsen, E. M., Gordon, K. D., and Menten, K. M.
High resolution radio continuum survey of M33: II. Thermal and nonthermal emission, Astronomy & Astrophysics, 2007, V. 475, p. 133
- Tabatabaei, F. S., Beck, R., Krause, M., Berkhuijsen, E. M., Gehrz, R., Gordon, K. D., Hinz, J. L., Humphreys, R., McQuinn, K., Polomski, E., Rieke, G. H., and Woodward, C. E.
A multi-scale study of infrared and radio emission from Scd galaxy M 33, Astronomy & Astrophysics, 2007, V. 466, p. 509
- Tabatabaei, F. S., Beck, R., Krause, M., Krügel, E., and Berkhuijsen, E. M.
Variation of the radio synchrotron spectral index in the interstellar medium of M33, Astronomische Nachrichten, 2007, V. 328, p. 636
- Tabatabaei, F., Krause, M. and Beck, R.
Spitzer images of M 33: a probe to radio-FIR correlation, Astronomische Nachrichten, 2005, V. 326, p. 532
- Tabatabaei, F. S., Krause, M. Beck, and R. Berkhuijsen, E.
The radio-F(IR) correlation in M33 in Turbulence in the magnetized interstellar medium, German-Russian Open Workshop, Perm, Russia, September 2006.
- Tabatabaei, F. S., Beck, R., Krügel, E., Krause, M., Berkhuijsen, E. M., Gordon, K. D., Menten, K. M.
Variations of the Radio Synchrotron Spectral Index in M33, in Formation and Evolution of Galaxy Disks, Vatican, October 2007
- Tabatabaei, F. S., Beck, R., Krause, M., and Berkhuijsen, E. M.
A Multi-Scale Study of IR and Radio Emission from M33, in Formation and Evolution of Galaxy Disks, Vatican, October 2007
- Tabatabaei, F. & Nasiri, S.
A Phenomenological Model for Evolution of Proto-Galaxies, 2003, astro-ph/0310202
- Tabatabaei, F. & Nasiri, S.
Distribution of the Surface Brightness of QSOs, proceeding of the ‘Annual Iranian Physics Conference’, Babolsar, August 1999
- Tabatabaei, F. & Nasiri, S.
Investigation of Luminosity Function of QSOs, Proceeding of the ‘Annual Iranian Astrophysics Research Conference’, IASBS, February 1999

- Tabatabaei, F. & Nasiri, S.
Different Morphologies of Galaxies and the Proposed Starburst Model, proceeding of the ‘Annual Iranian Astrophysics Research Conference’, IASBS, February 2000
- Gholami, I., Tabatabaei, F., and Jahanmiri, M.
Correction of the Limb Profile of the Moon for Determining the Variation of the Solar Radius, proceeding of the ‘Annual Iranian Astrophysics Research Conference’, IASBS, February 2000

Research Interests

- Dust emission and absorption in the galaxies’ ISM: The interstellar medium plays a central role in the evolution of galaxies. In order to understand how the energy sources of dust emission (and also extinction) varies as a function of environment and star formation efficiency. Using the wavelet transformation of the MIPS M33 data, we (Tabatabaei et al. 2007a) showed that, depending on the wavelength of the dust emission, heating sources of dust (UV photons from O/B stars or ISRF) varies with scale of emitting structure. In M33, at scales smaller than 0.8 kpc, cold dust is heated mainly by UV photons from massive stars, while an average interstellar field also contribute at larger scales. I also found that stellar photons are more important than cosmic ray electrons in heating the dust up to scales of 2kpc in M33. I plan to investigate these properties in other nearby galaxies like M31, M51 to probe different environmental conditions and starformation efficiencies. I am also interested in very cold dust detection in galaxies as it is important for SED studies globally and high-mass starformation locally. This will be done for M33 using the Hershel space telescope (I am a project member of the Herschel M33 extended Survey), allowing us to accurately determine the amount of dust in M33 and how it is distributed with respect to the stars and the gas. Polarization by dust is another interest as it is important to know how magnetic fields control star formation in galaxies.
- Radio-IR correlation in galaxies: separating the radio continuum emission to its thermal and nonthermal components on one hand and the IR emission to its cold and warm components on the other hand helps to better understanding the origin of this well-known correlation. Furthermore, correlation analysis locally and as a function of spatial scale is possible using the wavelet tool, providing a knowledge about the typical scale where the radio-IR correlation is maximum or, in case of high resolution data, the smallest scale this correlation is still valid.
- Origin and propagation of cosmic rays in galaxies: The map of synchrotron spectral index in M33 by Tabatabaei et al. (2007c) provides, for the first time in an external galaxy, information on the origin and propagation of cosmic ray electrons. I plan to extract these information using this map and through modellings.
- Extragalactic magnetic field: what is the role of magnetic field in energy ballance of interstellar medium, star formation efficiency, and evolution of galaxies? I have studied the magnetic field distribution, depolarization and Faraday effects in M33

using the Effelsberg and VLA radio polarization data and our recent separated map of the synchrotron emission from this galaxy (Tabatabaei et al. in prep). I plan to observe radio continuum emission from this galaxy using the EVLA in order to reach resolutions comparable to that of the Hershel that is important for energy ballance studies in M33's ISM.

- Evolution of galaxies and AGNs: I investigated the specific angular momentum in terms of the specific luminosity of galaxies of various morphological types for my MSc, showing inverse relations between these two parameters. Furthermore, I studied the luminosity function of QSOs using the LBQS data.